

THE UNIVERSITY
of ADELAIDE

Understanding the Aerodynamic Environment in Track Cycling

Shaun Fitzgerald

School of Mechanical Engineering
The University of Adelaide
Australia

A thesis submitted in fulfilment of the requirements
for the degree of Doctor of Philosophy
May 2022

PhD Thesis

Submission date: 17 November 2021
Amendment date: 2 May 2022

School of Mechanical Engineering
The University of Adelaide
South Australia 5005
Australia

Copyright © 2022 Shaun Fitzgerald.

All right reserved. No part of this report may be used or reproduced in any form or by any means, or stored in a database or retrieval system without prior written permission of the copyright holders except in the case of brief quotations embodied in critical articles and reviews.

For Felix

Abstract

This research project aims to improve our understanding of the aerodynamic environment experienced by a track cyclist within an indoor velodrome. This has been completed through the use of an in-situ experimental setup and the development of theoretical calculations for salient measurements. By developing an understanding of the aerodynamic environment, we can improve the accuracy of theoretical modelling and help develop new methods of bicycle and/or rider drag reduction.

The primary method for conducting this research was the development of an instrumented bicycle that can measure the incident airflow, roll angle, steering angle, and power output as a cyclist rides around a velodrome. A quasi-steady theoretical analysis of the airflow encountered by a cyclist travelling around a bend was created that indicates a yaw and pitch angle relative to the cyclist. A new model of velodrome geometry that includes transition curves into and out of the bends was also developed to improve the accuracy of theoretical calculations. Measurements of the roll and steering angles were completed and compared to theoretical calculations, including the effects of the bend transitions. The instrumented bicycle was also used to measure data in a velodrome with and without other riders.

It is found that the relative airflow experienced by a cyclist in an indoor velodrome deviates from a direct headwind due to three primary factors. Firstly, there is the position of the rider in the lap, with curved airflow arising when cornering/leaning on the bends. Secondly, there are several effects due to the rider's pedalling which can have a combination of influences, namely, rocking the bicycle side to side, steering the front wheel left to right, and the motion of the legs producing an upstream aerodynamic effect. Thirdly, there is an influence from other riders on the track, ranging from a large decrease in the airspeed when drafting directly behind a rider to a smaller influence from other riders when in their far wake. Turbulence measurements using

the instrumented bicycle show that other riders on the track can alter the freestream turbulence experienced by a cyclist, even when other riders are half a lap ahead.

Measurements of the flow through the middle of the bicycle frame were undertaken in a velodrome with a live rider, in a wind tunnel with an anatomically-accurate pedalling mannequin, and with potential flow calculations. The three different methods of experimentation all demonstrated a large deviation of ±15° of yaw angle due to the position and movement of the pedalling legs. A minor reduced-frequency effect was observed, indicating that the magnitude of the cadence can influence the aerodynamic results and the pedalling motion cannot be assumed to be quasi-steady at high cadences.

The work undertaken in this project helps to provide a greater understanding of the flow experienced inside an indoor velodrome and provides validation of commonly used theoretical calculations. It can be used as a first step towards the understanding and reduction of the differences between wind tunnel and field testing.

Declaration

I certify that this work contains no material which has been accepted for the award of any other degree or diploma in my name, in any university or other tertiary institution and, to the best of my knowledge and belief, contains no material previously published or written by another person, except where due reference has been made in the text. In addition, I certify that no part of this work will, in the future, be used in a submission in my name, for any other degree or diploma in any university or other tertiary institution without the prior approval of the University of Adelaide and where applicable, any partner institution responsible for the joint-award of this degree.

I acknowledge that copyright of published works contained within this thesis resides with the copyright holder(s) of those works.

I also give permission for the digital version of my thesis to be made available on the web, via the University's digital research repository, the Library Search and also through web search engines, unless permission has been granted by the University to restrict access for a period of time.

I acknowledge the support I have received for my research through the provision of an Australian Government Research Training Program Scholarship, as well as from the Australian Institute of Sport (AIS) and the South Australian Sports Institute (SASI) through an AIS PhD Program Scholarship.

Shaun Fitzgerald
2 May 2022

Acknowledgements

First and foremost, I must thank Richard, without whom this would not have been possible. Thank you for believing in me more than I could ever believe in myself. Thank you to Paul, for being the one to ensure that I actually finished this thing; and to Andy, for always bringing it back to the question of: 'how can we use this to go faster?'.

Thanks to my friends from Uni for the lunch-time chats, the after-work drinks, and the beach trips. To my netball team, for being a welcome distraction and always reminding me that yes, I do have long arms. And to my family for your unwavering encouragement and support.

To my assortment of housemates over the years: Declan, Kiri, Margaret, Briony, Ryan, Hazel and Freya. Thank you for reminding me that there were more valuable things in life than bicycles, and for feeding me on many an occasion.

Author's note

This thesis contains several journal articles that have either been published or submitted for publication. All included publications are identical to the original article, either as published or submitted, with the following exceptions:

- The typesetting, referencing style, and table formatting have been altered so that there is a consistent format throughout the thesis.
- The positions of figures and tables may differ from the final published version.
- Each publication's figure, table and equation numbers have the chapter number included as a prefix.
- To avoid duplication and maintain coherence, a common reference list is included at the end of this thesis.

A reference to the as-published article is provided at the beginning of each chapter. Permissions have been obtained from the journals for inclusion in this thesis.

Contents

List of Figures **x**

List of Tables **xiii**

List of Publications **xiv**

1 Introduction **1**
1.1 A brief overview of track cycling 1
1.2 Research objectives 3
1.3 Thesis outline 3

2 Literature review **5**
2.1 Power requirements for track cycling 5
2.1.1 Cornering dynamics 7
2.1.2 Aerodynamic drag 10
2.1.3 Rolling resistance 11
2.1.4 Potential and kinetic energy 12
2.2 Aerodynamic drag production in track cycling 13
2.2.1 Freestream turbulence 14
2.2.2 Cornering flow 16
2.2.3 Cadence 18
2.2.4 Drafting 20
2.3 Methods for cycling aerodynamic analysis 22
2.3.1 Wind tunnel experiments 22
2.3.2 Numerical computation 24
2.3.3 Field measurements 25
2.4 Bicycle dynamics and steering 26
2.5 Velodrome design 28
2.6 Concluding remarks 30

3 The in-situ aerodynamics of a team pursuit 32
Statement of Authorship 33
Abstract 34
3.1 Introduction 34
3.1.1 Cornering theory 37
3.2 Methods 41
3.3 Results and discussion 44
3.3.1 Stationary wind tunnel testing 44
3.3.2 Velodrome testing 45
3.3.3 Effect of rider position 47
3.3.4 Effect of location on the track 48
3.3.5 Effect of pedal cycle 50
3.3.6 General discussion 52
3.4 Conclusion 53

4 The theoretical impact of a velodrome transition curve 55
Statement of Authorship 56
Abstract 57
4.1 Introduction 57
4.2 Methods 60
4.2.1 Transition curve properties 60
4.2.2 Connecting a straight line to a circular arc 61
4.2.3 Fitting to a velodrome track 62
4.2.4 Curvature profiles 62
4.2.5 Banking 63
4.2.6 Bicycle dynamics 64
4.3 Results 66
4.4 Discussion 70
4.5 Conclusion 73
4.6 Supplementary material 74

5 The dynamics and aerodynamics of a single rider 76
Statement of Authorship 77
Abstract 78
5.1 Introduction 78
5.2 Results 80
5.2.1 Theoretical calculations 81
5.2.2 Changes over a lap 82
5.2.3 Changes over a crank cycle 86
5.2.4 Turbulence and wakes 87

5.3 Discussion 89
5.4 Conclusion 91
5.5 Methods 91
5.5.1 Instrumented bicycles 91
5.5.2 Velodrome 93
5.5.3 Errors and limitations 94

6 The influence of wheels and cadence **95**
Statement of Authorship 96
Abstract 97
6.1 Introduction 97
6.2 Methods 99
6.2.1 Velodrome testing 99
6.2.2 Wind tunnel testing 101
6.2.3 Potential flow calculations 104
6.3 Results and discussion 111
6.3.1 Effect of yawing the bicycle (front probe) 111
6.3.2 Effect of yawing the bicycle (middle probe) 113
6.3.3 Effect of the reduced frequency 119
6.4 General discussion 120
6.5 Conclusion 122
6.6 Supplementary material 123

7 Conclusions **124**
7.1 Recommendations for future work 127

A An additional turn curvature equation **129**
A.1 Derivation 129
A.2 Results 130

References **135**

List of Figures

1.1 Track cycling races and their typical bicycle types. 2

2.1 Summary of the forces on a cyclist and bicycle in motion. 6
2.2 Free-body diagram of a cyclist on a level banked corner. 8
2.3 Effect of freestream turbulence intensity on the drag crisis of a 2D circular cylinder. 15
2.4 Yaw angle of the airflow anterior to a bicycle travelling around a 250 m indoor velodrome track. 17
2.5 Plan view diagram of yawed airflow compared to curved, leaning flow. 18
2.6 The variation in drag area and frontal area over the course of a single pedal cycle. 20
2.7 The primary areas of aerodynamic influence relative to the primary cyclist on another cyclist. 21
2.8 Measurements of drag area from a variety of studies with different measurement techniques. 23
2.9 Steering angle on a bicycle travelling around a 250 m indoor velodrome track. 28
2.10 Cross-section diagram of a typical velodrome track with the required line markings. 29

3.1 The three components of total air velocity and the yaw and pitch angle definitions. 35
3.2 The steady-state airflow distribution observed by a leaning bicycle and cyclist on a corner of constant radius. 38
3.3 The steady-state free-body diagram of a bicycle traversing a level banked corner. 40
3.4 The instrumented bicycle with the position of the probe tip. 42

3.5 The Fourier Transform of the three components of velocity for stationary testing. ... 45
3.6 The three components of air velocity as well as the wheel speed for the length of a simulated team pursuit race. ... 46
3.7 Velocity of the wheels, total velocity, yaw and pitch over the course of a single lap. ... 49
3.8 The cadence-filtered yaw and pitch angles for lap 10, when the cyclist is in position 1, from both tests, displayed in a velodrome plot. ... 50
3.9 Fourier transform of the yaw and pitch angles for laps 2 to 16. ... 51
3.10 Probability Density Function of the yaw and pitch angles. ... 53

4.1 Plan view of a velodrome with required definitions. ... 59
4.2 Transition curve definitions for connecting a straight line to a circular arc with defining parameters Y and R. ... 60
4.3 Parameter space of the model where the shaded area indicates the limits of normalised inputs Y and R. ... 64
4.4 Free-body diagram of a bicycle on a level banked corner. ... 65
4.5 Comparing the model with two measured velodromes. ... 68
4.6 The effect of four different curvature profiles along one quarter of the track. ... 69
4.7 The bank angle of the two measured velodromes and a symmetric model. ... 70
4.8 Three different transition curve options and the influence of a constant V_{CG} on the bicycle dynamics. ... 71
4.9 Measuring a circular radius from arc length and chord length. ... 74

5.1 Measured and calculated roll angle averaged over 17 laps. ... 82
5.2 Measured and calculated roll angle for a range of wheel speeds. ... 83
5.3 Measured wheel speed, calculated centre of gravity speed, measured air speed, and measured power averaged over seven laps. ... 84
5.4 Measured and calculated steering input angle averaged over seven laps. ... 85
5.5 Measured and calculated steering input angle for a range of wheel speeds. ... 86
5.6 Measured steering angle over each crank cycle for a range of wheel speeds. ... 87
5.7 Primary bicycle used for testing and the bicycle coordinate system. 92

6.1 On-track flow visualisation ... 100

6.2 Bicycle coordinate system. 101
6.3 Pedalling mannequin and instrumented bicycle on the measurement rig in the wind tunnel. 103
6.4 The mannequin leg and bicycle model. 105
6.5 The input and output dimensions required to create an ellipse from a cone. 108
6.6 The stream function, velocity potential, total velocity, and yaw angle at a crank angle of 135°. 110
6.7 The different front wheels tested in the wind tunnel. 111
6.8 The effect of yawing the bicycle on the front probe. 113
6.9 The effect of yawing the bicycle on the middle probe. 114
6.10 Normalised flow speed, pitch and yaw at the three measured positions for three different data sets and a bicycle yaw angle of 0°. 116
6.11 Potential flow results along a horizontal line parallel to the centreline of the bicycle at a height of 374 mm above the bottom bracket. 118
6.12 Potential flow results 50 mm anterior to the seat tube over a range of heights above the bottom bracket. 119
6.13 Measuring the effects of reduced frequency at probe position P_1 between the mannequin legs. 121

A.1 The effect of Equation (A.1) on the curvature and its first three derivatives along one quarter of the track. 132
A.2 Parameter space of Equation (A.1) where the shaded area indicates the limits of normalised inputs Y and R with increasing geometric continuity. 133
A.3 A summary of all used transition curve equations and their first two derivatives. 134

List of Tables

3.1 Summary of data from stationary testing of the instrumented bicycle. 44
3.2 Average aerodynamic factors at each position along the team pursuit line. 48

4.1 Cyclist model input variables. 66
4.2 Numerical results from fitting different models to the measured velodrome data. 67
4.3 Chapter 4 nomenclature. 75

5.1 Comparison of velocity and turbulence measurements for the empty track test (1 cyclist) and the warm-up test (16 total cyclists on the track). 88

6.1 Mannequin and bicycle dimensions. 106

A.1 The straight, bend, and transition lengths for Equation (A.1) with increasing levels of continuity. 133

List of Publications

Included in this thesis

Published

- Fitzgerald, S., Kelso, R., Grimshaw, P., and Warr, A. (2019) 'Measurement of the air velocity and turbulence in a simulated track cycling team pursuit race' *Journal of Wind Engineering and Industrial Aerodynamics*, 190, 322–330, DOI: 10.1016/j.jweia.2019.05.014.

- Fitzgerald, S., Kelso, R., Grimshaw, P., and Warr, A. (2020) 'Observations of the flow experienced by a track cyclist using velodrome, wind tunnel, and potential flow investigations with an instrumented bicycle' *Journal of Wind Engineering and Industrial Aerodynamics*, 206, 104374, DOI: 10.1016/j.jweia.2020.104374.

- Fitzgerald, S., Kelso, R., Grimshaw, P., and Warr, A. (2021) 'Impact of transition design on the accuracy of velodrome models' *Sports Engineering*, 24, 23, DOI: 10.1007/s12283-021-00360-3.

Submitted

- Fitzgerald, S., Kelso, R., Grimshaw, P., and Warr, A. (2021) 'Measurements from an instrumented bicycle in a velodrome' Submitted to *Scientific Reports* (Nature Research).

Related

- Fitzgerald, S., Atkins, H., Kelso, R., and Dimitriou, A. (2018) 'Bicycle Helmets—Are Low Drag and Efficient Cooling Mutually Exclusive?' *Proceedings of the 12th Conference of the International Sports Engineering Association*, 2(6), 212, DOI: 10.3390/proceedings2060212.

- Fitzgerald, S., Atkins, H., Leknys, R., and Kelso, R. (2018) 'A Thermal Test System for Helmet Cooling Studies' *Proceedings of the 12th Conference of the International Sports Engineering Association*, 2(6), 272, DOI: 10.3390/proceedings2060272.

- Fitzgerald, S., Kelso, R., Grimshaw, P., and Warr, A. (2019) 'The influence of cornering on track cycling aerodynamics' *British Association of Sport and Exercise Sciences*, 37, 15, DOI: 10.1080/02640414.2019.1671688.

— Chapter 1 —

Introduction

The importance of aerodynamics in cycling cannot be understated, with over 90 % of a cyclist's resistive force at race speeds coming from aerodynamic drag [1]. This is particularly important in track cycling where the races are shorter and can be determined by fractions of a second. Here, a small drag reduction can lead to a significant advantage over the course of a race. As such, there has been extensive academic and industry research into the reduction of a cyclist's drag.

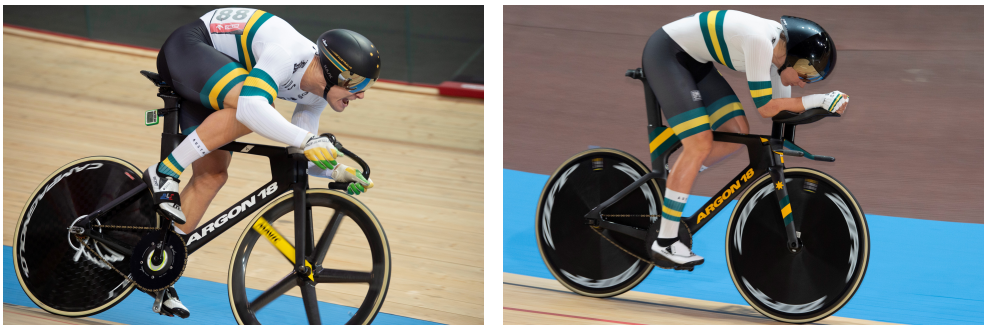
To date, most of the cycling aerodynamic research, leading to reduced drag and a performance advantage, has been conducted in a highly controlled environment. This allows for fine control over the experimental setup and provides accurate results. However, a clear understanding of the true environment that exists in a velodrome has not yet been achieved. Furthermore, the majority of cycling research is conducted for road cycling, rather than specifically for track cycling. This project aims to experimentally measure the aerodynamic environment experienced in indoor track cycling in order to improve experimental measurements, simulations and modelling.

1.1 A brief overview of track cycling

Track cycling is a particular subsection of competitive cycling consisting of various races that take place around a banked oval track known as a velodrome. The primary focus of this research is on track cycling, however some of the same principles can be applied to other areas of cycling such as road, triathlon, and para-cycling.

Track cycling has several different competitive race styles, which can be broadly split into two categories: sprint and endurance. The sprint events have higher bicycle speeds with shorter race times and are generally ridden with a bicycle with a spoked front wheel and without handlebar extensions, with an

example shown in Figure 1.1a. Endurance events are longer and can use either sprint bicycles or pursuit bicycles with handlebar extensions and a disc front wheel, as shown in Figure 1.1b. Speeds at sprint events can exceed 70 km/h whilst endurance events are typically closer to 60 km/h. Sprint cyclists will generally output very high power for a short period of time, whilst endurance cyclists will output a lower, but more continuous power.



(a) **(b)**

Figure 1.1 Track cycling races and their typical bicycle types: **(a)** sprint, and **(b)** endurance. Photo credit © Casey B. Gibson 2019 and 2020 [2], used with permission.

The rules of track cycling are governed by the Union Cycliste Internationale (UCI) who dictate all regulations in track cycling from race format to equipment design and velodrome shape. Bicycle manufacturers are required to conform to a variety of regulations regarding the design of bicycles [3]. Nearly all modern elite track cycling events take place inside an indoor velodrome, in order to be sheltered from the elements [4].

This research will primarily focus on the pursuit events in the endurance category, namely the individual pursuit and the team pursuit, using a bicycle following the style of Figure 1.1b. The individual pursuit is a single cyclist riding solo, whilst the team pursuit involves a team of four riders. In these races, two opposing teams/riders will start at the two pursuit lines in the middle of either straight and ride in the same direction around the track. The race is won by the team/rider with the shortest time after a fixed distance or by the overtaking team if they catch the other. The cyclists in these events, with only minor exceptions for changing position in a team pursuit, will generally attempt to follow the datum (black) line for all laps as that is the shortest path. While particular consideration is given to the pursuit events, the results presented in this research are applicable to other cycling disciplines.

1.2 Research objectives

This project aims to enhance the development of cycling aerodynamics, with a particular regard to track cycling, through the establishment of a thorough understanding of the fundamental aerodynamic conditions experienced by the bicycle and rider. This problem shall be addressed by undertaking an analysis of the airflow conditions and bicycle motion experienced by a rider on a typical lap in a velodrome. The understanding developed here can inform the design of new low-drag frames and components to ease the rider's workload. The knowledge gained can also be used to refine and validate cycling analytical models.

1.3 Thesis outline

Excepting Chapters 1, 2 and 7, this thesis is a collection of manuscripts that have either been published or are currently under review in international journals. Each research chapter contains a brief introduction discussing how it fits within the thesis as a whole, and a statement of authorship to specify the roles of all authors.

Presented in Chapter 2 is a literature review of the current state of the art in track cycling aerodynamics and the fundamental concepts that describe the movement of a cyclists in a velodrome. Chapter 2 provides the base knowledge required to understand this thesis and places the research within the context of the academic literature. A concise review of the literature specific to each research chapter is presented in Chapters 3 to 6.

The theoretical basis of curved airflow around a banked bend is defined and initial experimental results are presented in Chapter 3. Some effects of drafting in a team pursuit and turbulence measurements are also presented.

The effects of velodrome geometry on the dynamics of a cyclist is investigated in Chapter 4. A mathematical model of the velodrome datum line is produced so that any velodrome can be replicated with only two simple geometric measurements and the lap length. This facilitates calculations of roll angle and steering angle throughout a single lap.

A full set of bicycle dynamic and aerodynamic measurements around a velodrome are presented in Chapter 5. Experimental measurements are compared and contrasted to theoretical calculations.

Wind tunnel experiments are outlined in Chapter 6, undertaken with the aim of understanding the results of Chapter 3. The effects of the flow around the front wheel are investigated and help to explain the results from Chapter 3.

The flow between a rider's legs and the influence of cadence are also analysed. A potential flow model is created to expand the region of analysis.

Finally, in Chapter 7 the main conclusions from each research section are combined and discussed in context of the whole project. Recommendations for future work are also documented to highlight the potential applications of this research.

— Chapter 2 —

Literature review

This research focuses on understanding the in-situ aerodynamic environment experienced by a track cyclist in an indoor velodrome. This chapter outlines the overarching requirements to observe this environment and the prior research completed in cycling and other relevant research areas. As this is a thesis by publication, each subsequent research chapter also includes a short literature review detailing the salient research for that particular chapter.

2.1 Power requirements for track cycling

As an introduction, a mathematical model of the power requirements for cycling on a velodrome track will be outlined. Such a model is useful to provide a clear indication of the relative influence of the different power demand parameters when cycling. The fundamental power requirements for track cycling have been outlined by a number of different groups [5–12], most of which are based on the power model developed and validated by Martin et al. [13]. The most effective cycling models include expressions for both the power supply (from the athlete) and power demand (external resistance) components [14]. However, this research will only focus on the demand side of the power equation, with the supply side outside the scope. The power model outlined in this section is based on an individual pursuit event where a solo rider is assumed to follow the datum line and not deviate up the track banking for the duration of the event.

Figure 2.1 provides a summary of the forces in a plane perpendicular to the ground surface. Here F_P is the propulsive force, F_N and F_{RR} are the normal force and rolling resistance force respectively with subscripts 1 or 2 referring to the front or rear wheel. The aerodynamic forces F_L and F_D are the lift and drag respectively, acting at the combined bicycle and rider centre of pressure. Finally, F_W is the combined cyclist and bicycle weight, acting at

the combined bicycle and rider centre of gravity, and δ being the angle of inclination. The required power (P) that is input by the cyclist through the cranks can be split into four different components. The first, contributing over 90 % of the total mechanical resistance for speeds above 9 m/s on level terrain [15], is the power required to overcome the aerodynamic drag force (P_D). Secondly, there is the power to overcome the rolling resistance force (P_{RR}). Lastly there is the power required to overcome changes in potential (P_{PE}) and kinetic (P_{KE}) energy. The total power input is then multiplied by a power input efficiency coefficient (η) to account for drivetrain and frame hysteresis losses and is equal to the sum of these four components with

$$\eta P = P_D + P_{RR} + P_{PE} + P_{KE}. \tag{2.1}$$

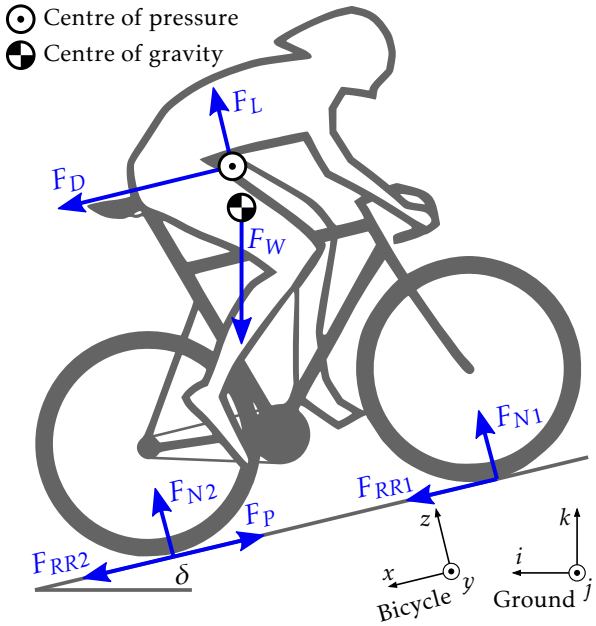


Figure 2.1 Summary of the forces on a cyclist and bicycle in motion on an inclined plane. The view is in the symmetry plane perpendicular to the ground surface.

Some power models also include the power required to overcome losses due to bearing resistance in the form

$$P_B = b_1 V + b_2 V^2, \tag{2.2}$$

where V is the bicycle speed and b_1 and b_2 are empirical coefficients. Most models [16–25] using this dissipation equation are based on the work of Danh et al. [26] as reported in Martin et al. [13]. The general form of Equation (2.2)

may be a valid method of determining bearing losses, but the typical values used for b_1 and b_2 are likely to be inaccurate for modern track cycling. The coefficients generally used, $b_1 = 0.091\,\text{N}$ and $b_2 = 0.0087\,\text{Ns/m}$, were developed by Martin et al. [13] from data in Danh et al. [26] of a greased cartridge bearing under 60 lb (27 kg) of load and for an unspecified wheel diameter (presumed to be a standard 700C road bicycle wheel). Over the last three decades there has been considerable research and development on bicycle bearings in the cycling industry and so these values are likely to be inaccurate for modern cycling. Additionally, they are for a specific model of bearing under a light load. As an example, using different data from Danh et al. [26] of an oiled cup and cone bearing with the method of Martin et al. [13], different coefficients $b_1 = -0.002\,\text{N}$ and $b_2 = 0.0004\,\text{Ns/m}$ are obtained. For a cyclist travelling at 15 m/s, using Equation (2.2) with the cartridge bearings provides a 3.3 W power requirement, whilst the cup and cone bearing has a 0.06 W power requirement, a 98 % reduction. Furthermore, the equation for the cup and cone bearing implies a negative drag (i.e. thrust) for speeds under 5 m/s which is not feasible. Modern development is likely to have further altered these coefficients. A detailed discussion on bearing resistance is given in Wilson [27] who concludes that bearing resistance is negligible compared with typical tyre rolling resistance and will only contribute a meaningful drag difference in long races. As such, bearing resistance will not be specifically considered for this track cycling power model and is assumed to be accounted for in the rolling resistance coefficient as done in other studies [10].

2.1.1 Cornering dynamics

When cornering on a velodrome, a cyclist experiences a centrifugal force which creates an overturning moment about the tyre/track contact point. To counter this moment with their weight, the cyclist will roll in towards the centre of the bend. If the bend is banked, such as in a velodrome, the bank angle helps to roll the bicycle, requiring less frictional force between the tyres and the track, allowing corners to be travelled at greater speeds.

To demonstrate this, a free-body diagram of the forces modelled as an inverted pendulum and during steady-state cornering around a level, banked turn, is shown in Figure 2.2. Here F_C is the cornering centrifugal force acting at the Centre of Gravity (CG), F_W is the combined cyclist and bicycle weight, F_N is the force normal to the track surface (equal to the sum of F_{N1} and F_{N2} in Figure 2.2), and F_f is the lateral frictional force. There are also two aerodynamic forces in the body-centred coordinate system, the lift force F_L and the side force F_S. These two forces, along with the aerodynamic drag along

the x-axis, will act through the Centre of Pressure (CP) at a height h_{CP} from the tyre/track contact point. There has been little work done determining the values of F_L and F_S and the exact position of the centre of pressure is difficult to determine, so the CP is usually assumed to be located at the CG and that F_L and F_S are assumed to be negligible [12].

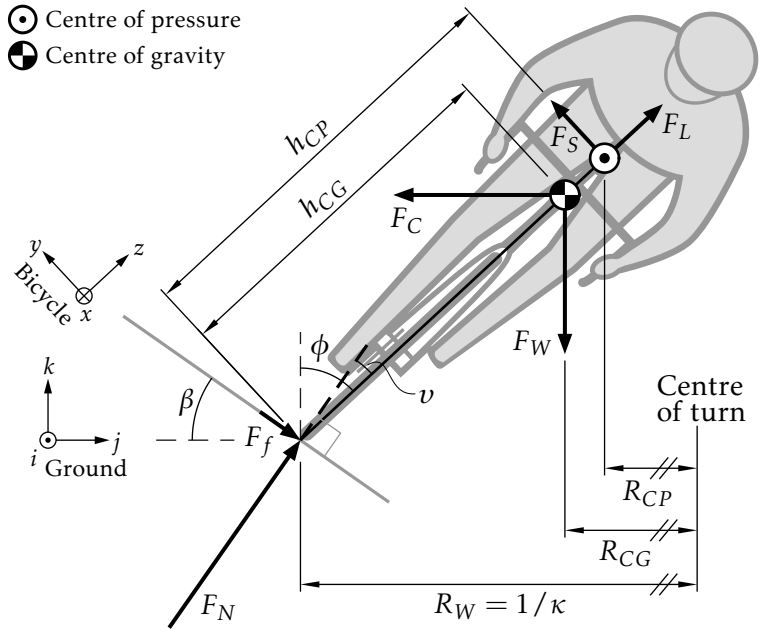


Figure 2.2 Free-body diagram of a cyclist on a level banked corner.

Using a quasi-steady-state approximation, the roll angle (ϕ) can be calculated by summing the moments about the tyre/track contact point to zero and is given by [10–12]

$$\tan\phi = \frac{\kappa V_W^2}{g}\left(1 - h_{CG}\kappa\sin\phi\right). \tag{2.3}$$

In this equation V_W is the velocity of the wheels, κ is the turn curvature which is defined as the inverse of the turn radius of the wheels, h_{CG} is the height of the CG, and g is the gravitational acceleration. Once the roll angle has been determined, the velocity of the CG (V_{CG}) can be found with

$$V_{CG} = V_W\left(1 - h_{CG}\kappa\sin\phi\right). \tag{2.4}$$

The four forces for steady-state equilibrium can then be determined with

$$F_C = m\kappa V_W^2\left(1 - h_{CG}\kappa\sin\phi\right), \tag{2.5}$$

$$F_W = mg, \tag{2.6}$$

$$F_N = mg\frac{\cos\upsilon}{\cos\phi}, \tag{2.7}$$

$$F_f = mg\frac{\sin\upsilon}{\cos\phi}, \tag{2.8}$$

where m is the combined mass of the cyclist and bicycle and υ is the camber angle which is defined as the difference between the roll angle and the bank angle with $\upsilon = \phi - \beta$.

Equations (2.3), (2.7) and (2.8) are based on the quasi-steady-state assumption where the bicycle is able to move between discrete steps, but is stationary when calculations are taken. This assumption is valid for periods of constant roll angle, but becomes inaccurate during transition periods. To improve mathematical accuracy, an unsteady analysis of the inverted pendulum model would require solving the second-order non-linear differential equation for roll acceleration [28, 29]

$$\ddot{\phi} = \frac{1}{h_{CG}}\Big(g\sin\phi - \kappa V_W^2\cos\phi(1 - h_{CG}\kappa\sin\phi)\Big). \tag{2.9}$$

However, Equation (2.9) produces oscillatory results that are unfeasible because of the instability of an inverted pendulum model. This is due to the lack of damping which would typically be provided by three-dimensional bicycle geometry and rider input. The accuracy of the quasi-steady-state assumption for track cycling, particularly on the velodrome bend transitions, has not yet been fully determined.

As outlined by Lukes et al. [9], when a cyclist travels around a velodrome track bend there is a critical wheel speed V_{CRT} at which the bicycle is perpendicular to the track surface. At this speed there is no lateral frictional force, the roll angle equals the bank angle, and the camber angle is zero ($F_f = 0,\ \phi = \beta,\ \upsilon = 0$). If a cyclist is travelling slower than the critical speed ($V_{CG} < V_{CRT}$) then the bank angle is too great and the bicycle has a tendency to slip down the slope ($F_f < 0,\ \phi < \beta,\ \upsilon < 0$). Conversely, if the cyclist is travelling faster than the critical speed ($V_{CG} > V_{CRT}$), the bicycle has a tendency to slip up the slope ($F_f > 0,\ \phi > \beta,\ \upsilon > 0$). A cyclist will counter the tendency to slip through steering, producing a lateral frictional force. The critical velocity for a given corner can be found by assuming the lean angle is equal to the bank angle ($\phi = \beta$) with

$$V_{CRT} = \sqrt{\frac{g\tan\beta}{\kappa\,(1 - h_{CG}\kappa\sin\beta)}}. \tag{2.10}$$

2.1.2 Aerodynamic drag

The power dissipation due to aerodynamic drag is

$$P_D = \frac{1}{2}\rho V_A^2 V_{CG}\Big([C_D A]_\psi + C_{RD}\Big). \tag{2.11}$$

The most important factors here are the coefficient of aerodynamic drag (C_D), the projected frontal area (A), and the wheel rotational drag area (C_{RD}). The two components C_D and A are generally interlinked with one affecting the other. These are difficult to determine independently so they are often combined as $[C_D A]_\psi$, also known as the 'drag area'. In this form, the underscore ψ indicates that the $C_D A$ is measured at a particular yaw angle (ψ). A yaw angle is when the airflow is incident on the cyclist at an angle of ψ in the horizontal plane. In addition to a yaw angle, the airflow on a cyclist could also be incident at a pitch angle (θ). However, this is generally considered negligible as the ground plane will typically only permit horizontal flow relative to the cyclist.

The yaw angles experienced by a cyclist can have a significant influence on their aerodynamic drag and side forces. However, it has generally been assumed that while there can be yaw angles for road cycling, there is no yaw inside a velodrome [9–12]. A study by Fintelman et al. [30] measured all three body-centred aerodynamic force coefficients for a cyclist across a yaw angle range of 0° to 90°. Fintelman et al. [30] showed that when increasing the yaw angle, the drag coefficient decreased, side force increased, and the lift coefficient remained approximately constant. Barry et al. [31] tested a variety of front wheels at a yaw angle range of 0° to 30°, also demonstrating increasing side force with increasing yaw angle.

Measurement and reduction of a cyclist's and/or bicycle's $C_D A$ are the primary aims of cycling aerodynamic research. The coefficient of drag has previously been assumed to be Reynolds-number independent for typical cycling speeds (i.e., C_D remains constant with varying speeds) [32]. However, there have been few studies that attempt to conclusively answer this question. A study by Terra et al. [33] provided a survey of the flow downstream of a stationary cycling mannequin's left arm, leg, and hip for a range of speeds from 5 m/s to 25 m/s. Terra et al. [33] show a distributed drag crisis with differing wake widths behind the arms and legs for different speeds, indicating an influence of Reynolds number effects. Studies have also measured the projected frontal area (A) of a cyclist to either estimate the $C_D A$ or to help determine the C_D [11, 34, 35].

The wheel rotational drag is generally more difficult to determine than $C_D A$, but is an area of increasing research over the last few years [36]. Whilst

some studies will measure the C_{RD} independently [13], others will include it as part of the coefficient of rolling resistance [37].

The velocity of the air relative to the cyclist (V_A) can be determined from the vector addition of the airspeed with the bicycle speed. This vector addition is typically done for outdoor road cycling [38], however most indoor track cycling models assume that the airspeed is equal and opposite to the centre of gravity speed ($V_A = -V_{CG}$) [6–11]. Fitton and Symons [12] specify a bulk airflow in the same direction of motion of the cyclists due to the movement of cyclists around a velodrome. The speed of this airflow is measured with an anemometer but is unspecified in their publication.

The final parameter in Equation (2.11) is the density of air (ρ) which can be found from the atmospheric temperature, pressure and relative humidity [39]. A simple strategy to lower aerodynamic drag is to reduce ρ by either increasing the temperature inside a velodrome or decreasing the atmospheric pressure by racing at high altitude. Both of these effects would be felt by all cyclists and so are unlikely to affect the outcome of a race from the point of view of aerodynamic drag alone. However, the effects are considerable enough that there can be a second, unofficial, category of world records (World bests) for the record at sea level compared to the official record that can be achieved at any altitude [40]. From a non-aerodynamic viewpoint, racing at altitude and in higher temperatures creates physiological issues that can be mitigated with acclimatisation [41]. A study by Bassett et al. [42] compared performances in hour-record attempts and determined an optimal elevation to be 2500 m for acclimatised riders and 2000 m for unacclimatised riders.

2.1.3 Rolling resistance

The power dissipation due to rolling resistance is

$$P_{RR} = mg\frac{\cos\upsilon}{\cos\phi}C_{RR}C_S V_W. \tag{2.12}$$

Here C_{RR} is the coefficient of rolling resistance which quantifies the resistance to forward motion due to rolling of the tyre on the track surface. There have been several studies measuring C_{RR} which falls typically in the range of 0.0015 to 0.0025 for track cycling [27].

Equation (2.12) has two modifiers of note for track cycling compared to typical road cycling. Firstly there is the term $\frac{\cos\upsilon}{\cos\phi}$ which describes the increase in the normal force due to the centrifugal force and banking on the corners. The centripetal acceleration greatly increases the non-dimensional g-force in the corners, equal to $1/\cos\phi$. For example, a cyclist leaning at 60° (which

is plausible for a sprinter at 70 km/h) would experience twice the normal gravitational acceleration, increasing the rolling resistance.

Secondly, there is the scrubbing coefficient C_S which is the increase in rolling resistance due to tyre scrubbing [9, 37]. Scrubbing is when the bicycle wheels do not undergo pure rotation, rather they will roll and slip simultaneously. Scrubbing is proportional to the camber angle, which is the angle between the bicycle roll angle and perpendicular to the track. To maintain an upright trajectory, the cyclist will steer the front wheel, creating a mismatch between the direction of motion of the cyclist and the direction of roll of the front and rear wheels, increasing rolling resistance. The increase in g-force and tyre scrubbing can both be observed in road cycling, but they are not as prominent due to the unique combination of high speed and small turn radii which are only experienced in track cycling with banked corners. Fitton and Symons [12] determined the energy loss due to scrubbing by combining empirical cornering and camber stiffness coefficients with calculations of wheel slip and camber angles. Other models [9, 11, 43] have used the bicycle camber angle as a proxy for wheel slip and camber angles to determine C_S using data from Kyle [37].

2.1.4 Potential and kinetic energy

During track cycling there can be changes to potential energy from three separate factors. These include travel up and down the bank, change in altitude of the track datum line (black line, see Section 2.5), and changes in height of the centre of mass of the cyclist due to roll. For most models, it is assumed that the cyclist will not divert from the datum line and that the datum line is in the horizontal plane, preventing changes in potential energy from the first two factors [7, 9–11, 42]. Fitton and Symons [12] presents the only known model to account for a change in height of the datum line. A study by Benham et al. [44] is based around how to best transform potential energy into forward speed when descending from the top of the track at the start of a 200 m sprint time trial. However, a significant limitation to that study is the position of the cyclist's CG. The cyclist is assumed to be a point mass at the surface of the track, rather than a point mass at a fixed distance above the track surface, a factor which would influence the presented results.

The change in potential energy from raising and lowering of the centre of gravity due to leaning in the bends is only included in two models [12, 45]. Fitton and Symons [12] assumes both positive and negative work from leaning, such that the total change in energy averages to zero across a lap. In contrast, a preprint article by Bos et al. [45] proposes that when a cyclist leans inwards

the potential energy is not converted into forward motion, but returning from a lean requires work by the cyclist. That is, there is no speed gain from leaning and there is an energy cost in recovering from the lean. Bos et al. [45] calculate an instantaneous power requirement of >2000 W during bend exits due to changes in kinetic and potential energy which greatly exceeds that seen in experimental power measurements [46]. It is clear that further work on the influence of leaning on the power demand is required.

The power demand from changing kinetic energy can come from a variety of sources. The predominant factor is the kinetic energy due to acceleration of the centre of mass, included in all mathematical models. A study by Olds et al. [47] measured the kinetic energy of the cyclist's legs, cranks, pedals, drivetrain, and wheels, showing a kinetic energy requirement of approximately <10 J (≈0.2 %) for the cyclist body segments, a negligible amount for the drivetrain, and ≈80 J (≈1.8 %) for the wheels. As such, models will often include the rotational kinetic energy in the wheels [12], but omit the rotational kinetic energy of the legs and/or drivetrain.

2.2 Aerodynamic drag production in track cycling

The production of drag in typical incompressible flow aerodynamics is usually from either pressure drag, which is the drag associated with the surface pressure distribution, or skin friction drag, which is the drag due to shear stress, or both. For cycling, where the combined cyclist and bicycle are generally considered as a bluff body, the predominant component is generally the pressure drag.

The primary governing parameter for aerodynamic analysis is the Reynolds number, representing the ratio of inertial to viscous forces with

$$Re = \frac{U_\infty l}{\nu}, \tag{2.13}$$

where U_∞ is the freestream velocity, ν is the fluid kinematic viscosity, and l is the characteristic length of the body in question. For cycling, the chosen length l can vary depending on the required application. For a complete cyclist, it is typically the torso chord length [33, 48], whilst when analysing body components, the segment diameter is typically used. When undertaking aerodynamic analysis, it is important that the Reynolds number used when performing experiments matches that found during the relevant cycling activity.

A key aerodynamic phenomenon that must be considered when performing cycling aerodynamic analysis is the drag crisis. This is where

the boundary layer on a bluff body transitions from a laminar to turbulent state at a critical Reynolds number. The turbulent boundary layer energises the flow, delaying boundary layer separation and thereby producing a smaller wake and lower pressure drag. In addition, the transition to turbulence also increases the skin friction, but generally the reduction in pressure drag is greater than the increase in skin friction, resulting in an overall reduction in aerodynamic drag. The drag crisis is typically observed on cylinders or spheres. Since a cyclist's body segments are similar to an interconnected series of cylinders [49, 50], all of which exhibit such behaviour, the occurrence or onset of the drag crisis can lead to a significant drag reduction of a cyclist.

The critical Reynolds number at which the drag crisis occurs can be altered through the surface roughness or freestream turbulence [38, 51, 52]. Several researchers have investigated the influence of the surface roughness of clothing fabrics on inducing the drag crisis for a drag reduction [53–56]. As different body segments have different characteristic lengths and local flow speeds, skinsuits can be designed with different fabrics in different zones [53]. This allows specific tailoring to induce the drag crisis with regards to the local Reynolds number.

2.2.1 Freestream turbulence

Freestream turbulence is a measure of the velocity fluctuation of the incident flow experienced by an object in an airflow. It is generally described by its intensity, integral length scale, and frequency spectrum [57]. These three factors are influenced by the environment in which the cycling event takes place, one extreme being indoor velodromes, which provide a minimal amount of turbulence. The atmosphere inside an indoor velodrome is often controlled with air-conditioning, with care taken in the design to keep the airflow speeds to below 0.25 m/s at track level [58]. This ensures that, in general, the air in an indoor velodrome is less turbulent in comparison to an outdoor velodrome, but turbulence cannot be ignored. Even indoors there is a turbulent flow field due to air conditioning systems, natural or forced convection, and the turbulent flow field produced by the wake of each cyclist. During a competitive event the movement and body heat produced by cyclists on the track, officials and team members in the centre of the track, and the crowd around the outside, would all contribute to a turbulent atmosphere.

A review paper by Crouch et al. [38] describes the existence of a turbulent freestream flow in a velodrome originating from: *"wind currents generated by natural or forced convection and also the decaying remnants of turbulent eddies left in the wakes of team members and other competitors"*. This is only an educated

assumption, as no experimental results quantifying the freestream turbulence are provided and Crouch et al. [38] detail the need for an analysis of the wind environment. A theoretical study by Watkins and Alam [59] outlines the requirements to consider the turbulent environment when studying sports, but also provides no experimental measurements for cycling.

Atmospheric freestream turbulence can influence the aerodynamic properties of a track cyclist. Early work by Fage and Warsap [51] on the drag crisis of a cylinder showed a lowering in the critical Reynolds number required for the drag crisis with increasing turbulence levels, shown in Figure 2.3. Fage and Warsap [51] used a mesh placed at various distances upstream of a cylinder in a wind tunnel to introduce freestream turbulence. A more detailed overview on the influence of turbulence on the flow around bluff bodies was given by Bearman and Morel [60] who observed three mechanisms by which turbulence influences the flow over a bluff body. These are an accelerated transition to turbulence, enhanced mixing and entrainment, and distortion of the freestream turbulence by the mean flow. From these influences, the primary factors in regards to cycling are an increase in skin friction with increasing turbulence and a delay in the boundary layer separation of bluff bodies. These two factors influence the drag of a cyclist, typically the first detrimentally and the second beneficially.

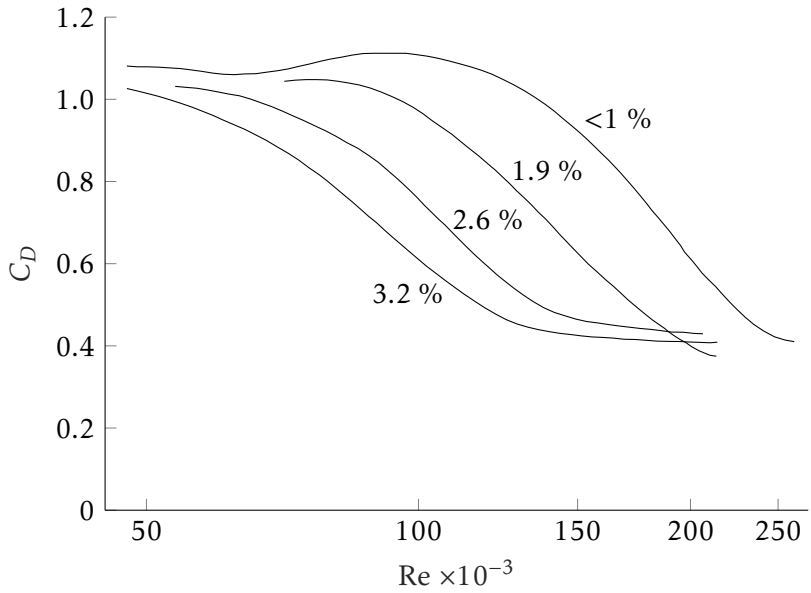


Figure 2.3 Effect of freestream turbulence intensity on the drag crisis of a 2D circular cylinder. Adapted from Fage and Warsap [51] with turbulence intensity values from Bearman and Morel [60].

The influence of turbulence on the drag crisis is so well defined in that it can be used as a measurable value of the turbulence in a wind tunnel when using a 'turbulence sphere'. This is a sphere mounted in a wind tunnel and tested over a range of Reynolds numbers. The critical Reynolds number for the sphere's drag crisis can then be determined through either drag measurements or surface pressure measurements [61]. This critical value can then be related to a turbulence factor for the tunnel which can be empirically related to turbulence intensity [62].

There has been extensive research on the effects of freestream turbulence in a variety of different fundamental aerodynamic applications such as cylinders, spheres and flat plates [63], but there is a lack of research on its effects on cyclists. Different works on cycling will mention that turbulence is known to influence the flow around a cyclist, but there have been few studies quantifying the turbulence values experienced by a cyclist [33, 38, 64].

Work on measuring the on-road turbulence and replicating it within a wind tunnel has been completed for motor vehicles [65–67]. Furthermore, it has been a well established fact for decades that the atmospheric boundary layer is required to be replicated for proper analysis in wind engineering [68]. Replication of the atmospheric boundary layer in a wind tunnel requires special consideration of the turbulence intensity and length scales.

A study of speed skating was completed by D'Auteuil [69] and D'Auteuil et al. [70] who measured the turbulence levels inside a skating dome using a three-component velocity probe 0.5 m ahead of a skater, mounted at waist height. In this investigation it was found that the airflow around a speed-skating rink is highly turbulent. It was proposed that the turbulence arises from the movement of the speed skaters and the temperature gradient in the air due to cooling by the ice. The measured turbulence was then replicated in a wind tunnel and the drag coefficient on a skating mannequin measured. D'Auteuil et al. [70] showed a lowering of the airspeed at which the drag crisis occurs with increasing turbulence levels. It also demonstrated the need to appropriately simulate the flow conditions in a wind tunnel in order to measure any meaningful drag reduction. Speed skating has a similar Reynolds number range and bluff-body geometry to track cycling and, with the exception of a temperature gradient due to the ice, the results are applicable to track cycling.

2.2.2 Cornering flow

In the literature on track cycling, several authors have assumed that the cyclist is riding in still air and there is no component of yaw or pitch in the

incident airflow [9–11, 42]. Fitton and Symons [12] include the effect of yaw throughout their mathematical formulation, but when applying the results they assume that the airflow is aligned with the cyclist's direction of motion. The zero-yaw/pitch assumption greatly simplifies the aerodynamic analysis of track cycling but it may not accurately model the real situation, as shown in a study by Kyle [37]. In this investigation, the airflow around a velodrome track was observed by recording the wind angle anterior to the handlebars of a bicycle as it traversed a track. The data was observed by mounting a mylar tuft on a protractor anterior to a bicycle head tube and recording it with a camera [71]. The only results presented are provided in Figure 2.4 with the approximate locations of the straights and bends indicated. Kyle [37] describes the creation of this yaw arising due to the bicycle turning on a track, shifting the incoming wind direction and causing a yaw angle as the track curves. No measurements of the airflow speed or pitch angle were recorded.

Figure 2.4 Yaw angle of the airflow anterior to a bicycle travelling at 30 mph (13.4 m/s) around a 250 m indoor velodrome track. Approximate locations of the straight and bend are highlighted. Adapted from Kyle [37].

In speed skating, D'Auteuil [69] measured the flow relative to a skater around several laps of a skating dome, recording 2° to 3° of yawed airflow in the corners. The aerodynamic influence of cornering has also been investigated in the automotive industry [72–74]. Keogh et al. [75] performed Computational Fluid Dynamics (CFD) studies on a generic four-wheeled vehicle (an Ahmed body [76]) in steady-state cornering. Keogh et al. [75] found an increase in the aerodynamic drag, an introduction of a yawing moment opposing the vehicles rotation, and a side force towards the centre of the corner resulting from the cornering airflow.

When riding outdoors in normal road cycling, there is often a yaw angle present from the vector addition of the cyclist's velocity with the natural wind. As such, several studies measuring the aerodynamic impact of a yaw angle on a cyclist have been completed [30, 31, 77–80]. However, all prior studies have

investigated the influence of a constant, yawed airflow with no pitch angle, as demonstrated in Figure 2.5a.

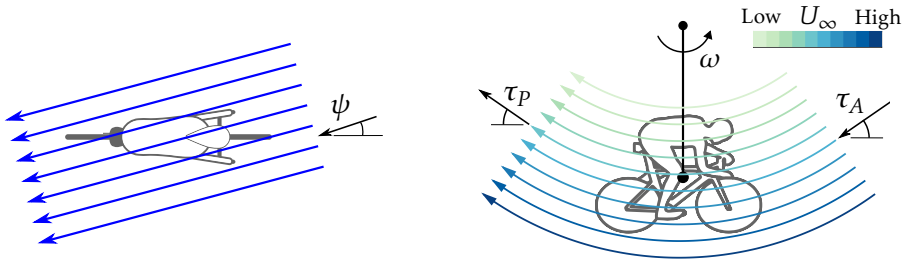


Figure 2.5 Plan view diagram of steady-state **(a)** yawed airflow and **(b)** curved, leaning flow.

When undergoing uniform circular motion on a level corner, a cyclist will experience curved relative airflow, with airflow incident from the inboard side anterior to the CG (τ_A), and exiting towards the inboard side posterior to the CG (τ_P), as shown in Figure 2.5b. In addition, there will be an increase in velocity on the outboard side of the cyclist compared to the inboard side. Due to the lean angle of the cyclist in a level bend, the curved flow in the horizontal plane would be composed of both a yaw and pitch angle relative to the cyclist. The instantaneous yaw and pitch angle will vary across the length of the cyclist.

A common feature in most cycling studies is that they only consider the effects of a constant yaw and do not take into account other aerodynamic considerations such as curved flow, pitch angle, or air speed relative to bicycle speed. As such, a comprehensive study detailing the aerodynamic effects of riding indoors that observes cornering flow characteristics would be highly beneficial to enhance the current knowledge of track cycling.

2.2.3 Cadence

A key feature in the aerodynamics of cycling is the change in airflow produced by the movement of a cyclist's legs. These large bluff bodies greatly influence the flow field around a cyclist. A measure of the effects of pedalling speed (cadence) is given by the ratio of the foot speed to the bicycle speed, known as the reduced frequency

$$k = \frac{2\pi r f}{U_\infty}, \tag{2.14}$$

where r (m) is the crank length, f (rad/s) is the pedalling frequency and U_∞ (m/s) is the freestream velocity [48]. The reduced frequency is an important

parameter that indicates the influence of unsteady effects in the flow around a cyclist's legs. At low k, the flow around the legs can be modelled as quasi-steady where only the position of the legs, not their velocity, influence the flow. For higher values of k, typically arising from either a high cadence or low bicycle speed, the influence of unsteady effects becomes more pronounced and a combination of the leg position and velocity will impact the flow. The exact value of k where the quasi-steady assumption becomes inaccurate is unclear and likely to be dependent on factors such as leg shape/size or freestream turbulence.

One of the earliest studies into cadence was by Baidya et al. [81] who measured the flow velocity in the wake of cycling legs. Baidya et al. [81] used a low flow speed and low-frequency cadence to maintain an acceptable k. This study did not include the effects of a cyclist's upper body or the bicycle and so cannot be directly compared to other studies, but it provided a reasonable comparison to more complete studies. Baidya et al. [81] tested a single reduced frequency of 0.11 (120 rpm at 19.6 m/s) and showed a fluctuating C_D with a changing crank angle.

Quasi-steady experimental studies of a pedalling mannequin have detailed the large wake and three-dimensional flows produced behind a cyclist through a phase-averaged quasi-steady study over the 360° crank cycle at 0° yaw angle [48, 82–84]. Figure 2.6, by Crouch et al. [48], demonstrates that the cyclist's drag area (C_DA) fluctuates with the leg position, with large variations in C_DA over the course of each crank cycle. Crouch et al. [48] demonstrated a minor variation of the frontal area with the pedal cycle that matched the phase of the variation in drag but did not correspond to the magnitude of the drag fluctuation, demonstrating the presence of an aerodynamic phenomenon that causes the majority of the variation in drag. The minimum drag regime occurred when both thighs were parallel and featured a quadruple arrangement of streamwise vortices in the cyclist's wake that were symmetrically aligned and which reduced the size of the near wake. The high-drag regime correlated with large asymmetrical streamwise vortices produced from the hips of the misaligned thighs that persisted far into the wake. This study clearly demonstrated the need to include variation in leg position with any experimental investigations.

Further dynamic work has been completed, where the wake of a cyclist is measured while the legs are pedalling. Crouch et al. [49] used experimental measurements of a mannequin in a wind tunnel to observe the wake at a variety of reduced frequencies ranging from $k = 0$ to $k = 0.115$. Griffith et al. [50] completed a CFD analysis of a pedalling mannequin with a morphing mesh and moving geometry, achieving reasonable agreement with wind tunnel

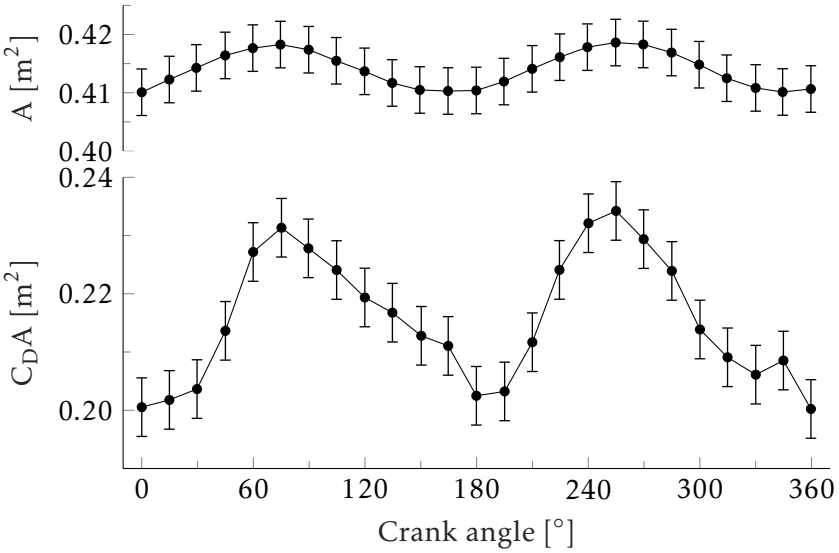


Figure 2.6 The variation in drag area and frontal area over the course of a single pedal cycle. The 0° crank position is defined when the cranks are horizontally aligned and the right leg is forward. Adapted from Crouch et al. [48], reproduced with permission.

values. Spoelstra et al. [85] measured the wake of a pedalling cyclist through PIV measurements. This research has shown that it is likely that the quasi-steady assumption holds true for cadences at least up to $k = 0.11$ (≈100 rpm at 16 m/s).

2.2.4 Drafting

There is a change in the aerodynamic forces experienced by a cyclist when riding within the area of aerodynamic influence of other cyclists, cars, or motorcycles. The typical case, otherwise known as drafting, is for a cyclist to ride directly behind one or more other cyclists to shelter themselves in their wake where they experience less drag [38]. This is shown as position A relative to the primary (blue) cyclist in Figure 2.7. Quantifying the influence of an upstream body on the aerodynamic drag of a following cyclist is an area of extensive research with numerous groups applying different methods to determine the relative drag decrease compared to a solo rider [22, 32, 86–100]. The primary factors that influence drafting behind a single cyclist are: the longitudinal distance behind the primary cyclist (d_T), the lateral offset from the primary cyclist (d_y) and the respective sizes of both the drafter and draftee. These three factors influence how well the draftee fits within the wake of the drafter and consequently the drag force experienced.

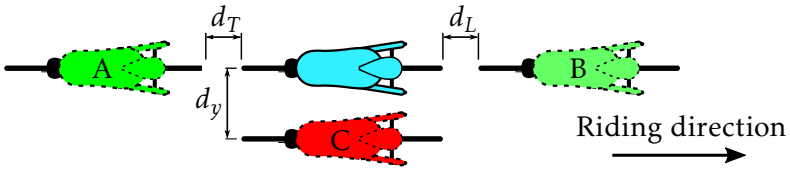


Figure 2.7 The primary areas of aerodynamic influence relative to the primary cyclist (blue, unlabelled) on another cyclist (A, B, C).

The magnitude of the drag reduction is inversely proportional to the longitudinal separation behind two cyclists and so typically cyclists will ride together as close as is safely possible. As such, most drafting research is conducted with a distance between two cyclists of <1 m and the exact distance where the effect of drafting becomes negligible is unknown. The greatest known drafting distance measured is a CFD study that demonstrated a 7 % drag reduction for a cyclist riding 50 m behind a motorcycle [22]. This value is likely to be higher than the equivalent reduction behind a cyclist as a motorcycle will produce a much larger wake, but it demonstrates that the drafting effect is present for an extended distance behind a cyclist. In an individual or team pursuit event, the opposing riders will begin half a lap (125 m) ahead and exactly how much of a drafting influence the opposing rider or team has remains an open question.

Studies that measure the lateral offset when drafting have shown that there is a decrease in the drag reduction when the trailing cyclist moves laterally away from the leading cyclist's centreline [91, 96, 98, 99]. A study of drag reduction whilst behind a motorcycle and laterally offset by 1.3 m showed an approximately constant drag reduction of 2 % from 2.9 m to 7.2 m [99]. Blocken et al. [99] proposed that this was due to the simultaneous effects of a widening wake with increased downstream distance and decreasing wake velocity defect balancing out, resulting in a constant drag reduction.

In addition to the benefit to a following rider, the preceding rider (position B) can also experience a drag reduction. This is due to the upstream effect of a following body filling the wake of the first cyclist, first identified by Íñiguez-de-la Torre and Íñiguez [88]. This means that both a rider behind and a rider in front can reduce the aerodynamic drag of a cyclist. This leads to the lowest drag position being the second-to-last (as opposed to the last) in a drafting line of four [95] or greater than five cyclists, [97, 100].

Contrasting to in-line drag reduction, there can be a drag increase from two cyclists riding parallel (position C). This has been observed in studies involving an overtaking cyclist [91] and motorcycle [99]. This drag increase has been observed to occur due to an increase in the size of the low pressure

area around the waist of the cyclist from a parallel cyclist/motorcycle [99]. This is particularly important for cyclists when overtaking [91] or changing positions in a team pursuit.

2.3 Methods for cycling aerodynamic analysis

This section will outline the three overarching methods of cycling aerodynamic analysis. Each method can provide a measure of a cyclist's C_DA through independent means with differing confidence levels and each can provide differing information detailing the causes of drag. One common issue for all three methods that is not typically mentioned is the skill level and experience of the researcher, which can often be the limiting factor that produces the greatest error.

There is a large level of uncertainty for cycling aerodynamic drag analysis due to a variety of reasons. The primary factor is that measurements are generally taken of human subjects which have considerable variability. This is in contrast to typical fundamental aerodynamic measurements which can be of well-established geometric profiles such as the National Advisory Committee for Aeronautics (NACA) aerofoil series [101] or the standard Ahmed body for cars [76]. Even when anthropomorphic mannequins are used to increase repeatability, the mannequin and bicycle from each research group are different and direct comparisons are impossible. An example of the spread of C_DA ranges for different measurement techniques and different participants/mannequins is provided in Figure 2.8.

One of the features of cycling aerodynamic analysis is that research is often completed behind closed doors as teams and companies seek to gain a competitive advantage. This is demonstrated in a LinkedIn post by a McLaren Applied employee showing a CFD analysis of a pedalling cyclist [114]. No details or results are provided on this model; just a video showing the pressure coefficient and an unknown isosurface for one pedalling cycle. It is evident that other researchers in industry have completed extensive cycling aerodynamic analysis, particularly with CFD, but most information is not publicly available.

2.3.1 Wind tunnel experiments

Experimental wind tunnel measurements are often seen as the 'Gold Standard' in aerodynamic drag testing as they are considered the most accurate. Traditionally, cycling analysis was conducted in wind tunnels built for aerospace [115] or motor vehicles [116, 117]. However, over the last decade

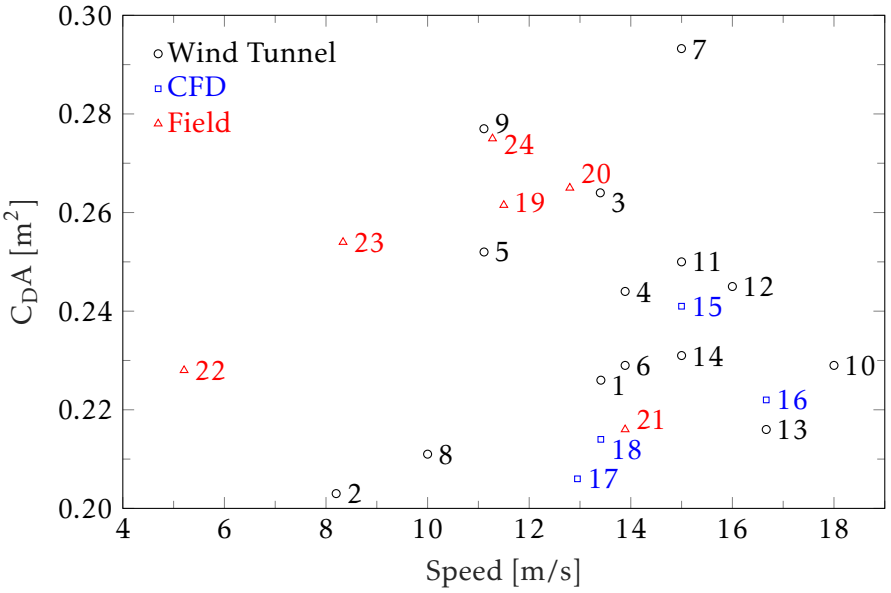


Figure 2.8 Measurements of drag area of a cyclist in a time-trial position from a variety of studies with different measurement techniques. For studies with several C_DA measurements, the mean of all measurements were taken. Data from: (1) Kyle [102], (2) Zdravkovich et al. [103], (3) Martin et al. [13], (4) Padilla et al. [104], (5) Jeukendrup and Martin [16], (6) Gibertini and Grassi [105], (7) García-López et al. [106], (8) Defraeye et al. [107], (9) Underwood et al. [108], (10) Barry et al. [92], (11, 15) Blocken et al. [94], (12) Crouch et al. [49], (13, 16) Chi et al. [109], (14, 18) Malizia et al. [36], (17) Javadi et al. [110], (19) Grappe et al. [111], (20) Candau et al. [112], (21) Fitton et al. [95], (22, 23) Spoelstra et al. [85], (24) Valenzuela et al. [113].

there have been several dedicated cycling wind tunnels constructed [118–121]. Wind tunnel experiments can be very expensive [117, 122] and there are a limited number of facilities available. A comprehensive outline of wind tunnel testing for cycling is provided by Brownlie [123].

Typical wind tunnel experiments include either a live cyclist on a bicycle, a mannequin on a bicycle, or the bicycle alone, and measure the total aerodynamic forces and moments on the cyclist/bicycle. These experiments are very repeatable, particularly if a mannequin rather than a live cyclist is used. The use of an athlete in a wind tunnel experiment is the greatest cause of repeatability issues due to movement of the cyclist between and during tests. There can also be some limits to the flow speed used for live riders due to safety concerns. Mannequins can have a fixed leg position [33], have the legs moved quasi-statically [48], or have powered legs that pedal automatically [49, 81].

Force measurements are commonly provided by a load cell in the wind

tunnel floor with a typical accuracy of ≈1 % [123]. Measurements are generally very quick to conduct with the drag results displayed live and quick changes to flow speeds and yaw angles readily available. Another method of drag measurement is through a wake momentum balance [124].

When using force balances in a wind tunnel, there can be a lack of fine detail as to the flow pattern around the cyclist/bicycle and the influence of the various geometric features. However, there are several methods to investigate the flow pattern around the cyclist/bicycle and the geometric features that contribute most to the drag. These include: pressure probes, hot-wire anemometry, Particle Image Velocimetry (PIV), surface pressure measurements, and wool tufts.

One of the largest limiting factors with wind tunnels is the blockage which can refer to solid-body blockage, wall interference effects, or longitudinal pressure gradients. To minimise blockage effects, it is generally best to keep the blockage ratio, which is the ratio of projected frontal area of the test object to the cross-sectional area of the test section, below 5 % [61] where the effects are negligible. Additionally, an open-jet test section has a smaller blockage effect than a closed-jet test section [61]. Blockage can be ameliorated by the use of a scale model of the cyclist/bicycle. However, this requires increasing the flow speed to maintain Reynolds number similarity [32], although this is often difficult to achieve in practice. If the blockage ratio is acceptable, it is generally best to use a full-scale cyclist/bicycle.

2.3.2 Numerical computation

Numerical analysis through Computational Fluid Dynamics (CFD) is an area of extensive research for cycling. CFD has the advantage that it can be far cheaper and more readily accessible than wind tunnel testing and can provide much greater detail. The complete flow field is analysed and is available for the discerning researcher, providing fine detail as to the cause of a cyclist's drag. The forces on different sections of a cyclist or bicycle can be directly measured and compared.

However there can be difficulties in verifying the accuracy of the results due to the number of assumptions and turbulence models used during analysis. There can often be a trade-off between the accuracy and computational time for numeric modelling, particularly with the size and resolution/quality of the mesh used to model the domain. A highly detailed mesh with numerous nodes requires considerably more computational time to complete an analysis. The most detailed cycling CFD analysis to date was conducted on a complete cycling peloton, had nearly 3 billion cells and took

54 h per case to complete on a supercomputer [32]. This is a detailed study with many separate geometries and is far beyond the computing abilities of most institutions.

Typical CFD work for cycling is generally completed with static geometry due to the difficulty and high computational cost of modelling a pedalling cyclist. A notable exception is the work of Griffith et al. [50] who completed a CFD study with legs moving in 1° increments in a continuous flow field. Another CFD study with pedalling legs has been completed in industry, but only minimal details were publicly provided [114].

2.3.3 Field measurements

The third area for cycling analysis is through field testing which can be achieved through the use of a variety of on-bike and off-bike sensors. The two primary requirements are a wheel speed sensor and a power meter, although secondary sensors are also available. The advantage of field testing is the availability and low cost of the testing equipment. This allows a greater number of cyclists to determine their aerodynamic drag and understand possible improvements. Secondly, as field measurements are taken in-situ, all environmental factors are as-experienced by a cyclist. Therefore, factors such as freestream turbulence, which is typically governed by wind tunnel design and chosen CFD parameters, are close to those that would be found during competitions. However, field testing does not provide the accuracy, resolution, or fine details of the flow field that can be observed in either wind tunnel or CFD studies.

The earliest field tests were simple coast-down tests that measured the time and distance for a cyclist to coast to a stop from a constant velocity with no pedalling [1]. A coast-down test has the distinct advantage that no specialist instruments are required on the bicycle and so it can be used with very little participant effort [125]. More advanced testing was done by Martin et al. [7] who demonstrated the ability to combine a power meter, wheel speed sensor and a mathematical model to measure a cyclist's C_DA and C_{RR}. Several other researchers have since used similar models to calculate a cyclist's C_DA in a velodrome [10, 11, 95].

At least two commercial probes specifically designed for drag measurment in cycling have been released. Devices such as the Notio Aerometer (Notio Technologies, Canada) [126] and AeroPro (AeroLab Tech, Canada) [127] are Pitot-static tubes mounted to the handlebars anterior to the rider. These are used to provide a measure of the airspeed to increase accuracy of C_DA measurements, rather than measuring the airflow for research purposes [113,

128]. Both the Notio and AeroPro have software configurations for C_DA testing inside a velodrome.

One of the largest difficulties with field testing is extracting just the aerodynamic drag component from the various dissipative forces. As typical field testing is essentially solving Equation (2.1) for C_DA, the accuracy of all other input values can have a significant influence on the accuracy of the final result. For example, if the input value of C_{RR} is too high, then the resultant C_DA value will be low. Some analysis methods solve for C_DA and C_{RR} simultaneously [129] whereas others require a constant C_{RR} to be input [10, 11, 95].

More advanced field testing has been completed by a group who measured the wake of a cyclist transitioning through a plane with large-scale stereoscopic PIV [25, 85, 130]. The C_DA of a cyclist can then be determined via wake momentum analysis. As the cyclists traverse through a bubble-filled tent, any environmental wind or turbulence is minimised and so the true environment found in typical cycling is not completely replicated, but this method of testing combines a typical cycling setup and semi-realistic environment with the fine measurement detail usually only possible in a wind tunnel. This method requires specialist equipment and expertise and so is not able to be conducted by typical researchers without significant effort and cost.

2.4 Bicycle dynamics and steering

Cycling dynamics is an area of considerable research dating back to the early work of Whipple [131] and Carvallo [132] who produced the first mathematical models of bicycle dynamics. The understanding of bicycle dynamics and stability have since been developed by various researchers, with a detailed summary provided by Meijaard et al. [133]. However, the vast majority of bicycle dynamics research is on the stability of a typical road bicycle ridden in an upright position at low speeds, rather than a track bicycle in a pursuit position and at high speeds. The standard equations presented by Meijaard et al. [133] are linearised based on the assumption of small roll and steering angles, however this is likely to be inaccurate for track cycling where high roll angles (>45°) are common. Rather, more complete non-linear bicycle dynamics equations, such as those shown by Wang et al. [134], would be required for track cycling. However, the non-linear equations are typically too complex to derive without the help of symbolic computer programming [134].

Whilst there are obvious similarities between a motorcycle and a bicycle, there are important differences between the two that influence their dynamics

and whether motorcycle research can be translated to bicycle research. A significant factor is the difference in mass ratio between the rider and the vehicle. A motorcycle can account for as much as 80 % of the total mass, whilst a bicycle will compose closer to 10 % to 20 % of the total mass [29]. Additionally, a motorcycle rider is much more likely to move their body mass relative to the bicycle compared to a track cyclist who will maintain a fixed position in order to reduce aerodynamic drag.

Typical velodrome models [7–11] will use simple bicycle dynamics equations that assume the cyclist/rider is a point-mass inverted pendulum rather than more complete equations [133]. This has the distinct advantage that the only measurements required are wheel speed, power, lap time, mass, and centre of gravity height; all of which are easily measured or estimated in the daily training environment. Otherwise, extensive measurements of the bicycle and rider are required to determine the correct mass and moment of inertia distribution [135].

Several studies have calculated the roll angle for a cyclist in a velodrome using Equation (2.3), but they have not compared the calculation to experimental measurements [9–12]. A key feature of the presented roll calculations is the assumption that the cyclist will follow the datum line exactly. This becomes an issue based on the assumptions used to model the datum line. Some models will use a datum line model consisting of straights and circular bends, but these produce a discontinuity in the calculated roll angle due to discontinuities in the modelled track turn radius [10, 11]. Others have used theodolite measurements to produce a continuous model of the datum line [12]. Additionally, how closely a track cyclist will follow the datum line has not been researched.

The only known work to experimentally measure the steering angle in a velodrome is by Kyle [37] and is shown in Figure 2.9. Kyle [37] shows an average steering angle of 1° on the straights, increasing to 4° in the bends. On top of this, a ±2.5° oscillation is also shown within each pedal cycle as the rider moves the front wheel left to right. However, it is unclear where exactly along the lap this data was obtained. This experiment was conducted with an elite athlete and used a protractor mounted to a head tube that was filmed with a camera mounted to the top tube [71].

Fitton and Symons [12] use the bicycle geometry with a forward integration model and equations developed by Pacejka [136] to determine the bicycle steering angle around a velodrome. These steering angle calculations involve the determination of the slip and camber angles of both the front and rear wheels from experimentally measured wheel camber and cornering stiffness coefficients. This requires calculation of the bicycle heading angle,

Figure 2.9 Steering angle on a bicycle travelling at 13.4 m/s (30 mph) around a 250 m indoor velodrome track. Approximate locations of the straight and bends are highlighted. Adapted from Kyle [37].

which is the angle between the bicycle velocity vector (V_{CG}) and the longitudinal axis of the bicycle frame. The steering input at the bend apex was shown to increase from 1.35° at low speeds to a maximum of 1.75° at V_{CRT} before decreasing at higher speeds. The steering angle across a lap was not presented and Fitton and Symons [12] did not experimentally verify the calculations.

2.5 Velodrome design

All track cycling events take place on a velodrome track, which is a custom-designed oval track. The sizes and shapes of velodromes can vary, with few official regulations provided by the UCI [4]. The current research will focus on Category 1 velodromes which can be used for Elite World Championships and Olympic Games. These tracks are 250 m long and form the majority of velodrome designs. A diagram describing the features of a velodrome track is shown in Figure 2.10, detailing the change in bank angle and relevant race lines.

The official requirements for a Category 1 velodrome are summarised below. These values were calculated by the UCI for maximum safe speeds of 85 km/h to 110 km/h [4].

- The inner edge of the track must consist of two circular arc bends and two parallel straight lines, with a gradual transition curve connecting the straights to the bends.

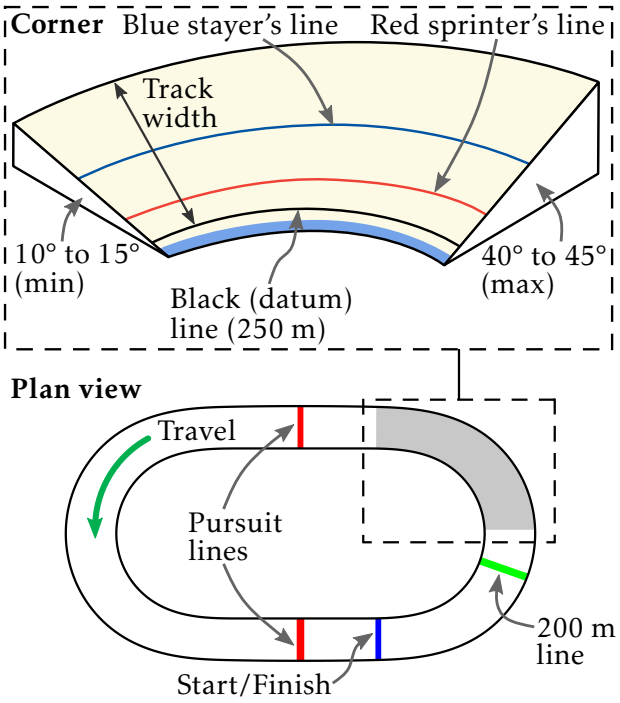


Figure 2.10 Cross-section diagram of a typical velodrome track with the required line markings.

- The track banking is to be determined by the turn radius and the maximum speed in each discipline.
- A lap length of 250 m with a tolerance of +0.0000 m to +0.0125 m.
- A minimum turn radius of 19 m to 25 m.
- A constant track width of 7 m to 8 m with a straight cross-sectional profile.

These regulations provide substantial room for variation in track design, particularly in regards to the bank angle profile and bend transition curve. The bank angle typically varies from a minimum of 10° to 15° in the straights to a maximum of 40° to 45° in the bends, however each track has its own particular geometry. The bank angle is typically steeper on the track exit than the track entry to provide greater speed for cyclists exiting the bend [137]. Velodrome datum lines are generally level in the horizontal plane, although there are some exceptions. Fitton and Symons [12] describe the only known track cycling model that includes a change in the elevation of the velodrome datum line.

Velodromes can be built outdoors, however the present research focuses on indoor velodromes that are enclosed to exclude the natural elements and where high-level track events are conducted. These are large buildings that have a roof, an empty space in the centre of the track for athletes and coaches, and seating for spectators around the outside. The atmospheric environment is often controlled, with air-conditioners moderating the heating and cooling so that track management can provide a comfortable environment for spectators and athletes. Additionally, the air temperature will often be increased to a higher than typical value to lower the air density, allowing cyclists to ride faster, leading to more exciting race events and increasing the likelihood of breaking world records. This method of atmospheric control is not standardised.

2.6 Concluding remarks

This chapter reviewed the literature in areas related to this research, providing the groundwork for understanding how the later chapters fit within the current research. An overview of the power demand requirements and methods for aerodynamic analysis were presented to outline how and why cycling analysis is completed. Different methods of drag production by a cyclist and common methods of drag reduction were outlined. A brief overview of relevant bicycle dynamics and velodrome design provides an outline of the movement of a cyclist in a velodrome.

From this review of the literature, it can be seen that there are a number of gaps in our understanding of the aerodynamic environment inside a velodrome. These issues are detailed in the following paragraphs.

- There is a lack of understanding of the yaw, pitch, and speed of the airflow incident on a rider inside a velodrome. Current models and experimental work generally assume that the airflow velocity is equal and opposite to the rider's velocity. However, if there is a deviation in any of the yaw, pitch or speed, the rider's aerodynamic drag can vary.

- There have been no published measurements of the turbulence inside an indoor velodrome and no replication in wind tunnel or CFD research. The majority of cycling aerodynamic analysis is completed in wind tunnels or CFD codes with low turbulence as this approach produces the most reliable and definitive results. However, there can be a difference in the aerodynamic environment experienced on the track compared to that replicated in the wind tunnel or through CFD.

- There have been several mathematical models involving calculations of the roll angle that have not verified the accuracy of Equation (2.3). Additionally, typical models will have disjointed and inaccurate models of the track geometry that can influence the accuracy of calculated roll angles and velocity.
- There has been minimal work measuring or calculating the steering angles across a lap or within a pedal cycle. The steering angle can influence the bicycle rolling resistance and aerodynamic drag around a lap and within a pedal cycle.
- There is the potential for further research into the effects of cadence on the flow around the bicycle frame, particularly if the research is completed outside of the controlled environment in a wind tunnel with a mannequin.

The majority of these aims can be achieved through field testing. Field testing, as outlined in Section 2.3.3, has the distinct advantage that the testing environment is virtually identical to the true race environment, however it can produce greater errors than wind tunnel or CFD tests. A method of achieving the realism of field tests with the accuracy of wind tunnel or CFD experiments involves measuring the aerodynamic environment in track cycling and then replicating that environment in the wind tunnel or in CFD experiments. This research undertakes the first component of this approach.

Furthermore, extensive work has been completed on modelling track cycling, both in the academic literature and with national sporting organisations or private analysts. It is clear that there is a need for cycling analysis, and that all models have a variety of assumptions built into them. This work will attempt to reduce the number of assumptions and experimentally compare measured to calculated values of lean and steering angles.

It is intended that this research will result in a greater understanding of the environment experienced by a track cyclist inside a velodrome. This can then be used in the research and development of aerodynamic components as well as to improve race analysis.

— Chapter 3 —

The in-situ aerodynamics of a team pursuit

This chapter outlines experimental work measuring the airflow experienced by a track cyclist when riding in a team pursuit formation around an indoor velodrome. A review of previous research into the aerodynamic environment in cycling and other sports is presented. Theoretical calculations for the flow experienced by a cyclist in uniform circular motion while leaning are then developed. An instrumented bicycle with a three-component velocity probe was used to measure the flow anterior to a single cyclist in a team pursuit.

Results show that the airflow in a velodrome is dependent on the rider's position relative to other cyclists, their position in the lap, and their location in the crank cycle. The measured yaw angles on the bends were much greater than the theoretically calculated values, with further research required to fully understand the reasons for this. The turbulence intensity was shown to increase significantly when the instrumented bicycle was ridden behind other riders and consideration for this is required when performing future track cycling aerodynamic studies.

This chapter has been published in the *Journal of Wind Engineering and Industrial Aerodynamics* and has been reformatted for this thesis. The as-published article is available at:

Fitzgerald, S., Kelso, R., Grimshaw, P., and Warr, A. (2019) 'Measurement of the air velocity and turbulence in a simulated track cycling team pursuit race' *Journal of Wind Engineering and Industrial Aerodynamics*, 190, 322–330, DOI: 10.1016/j.jweia.2019.05.014.

Statement of Authorship

Title of Paper	Measurement of the air velocity and turbulence in a simulated track cycling team pursuit race
Publication Status	☑ Published ☐ Accepted for Publication ☐ Submitted for Publication ☐ Unpublished and Unsubmitted work written in manuscript style
Publication Details	Fitzgerald, S., Kelso, R., Grimshaw, P., Warr, A. (2019). 'Measurement of the air velocity and turbulence in a simulated track cycling team pursuit race' *Journal of Wind Engineering and Industrial Aerodynamics,* 190, 322–330, DOI: 10.1016/j.jweia.2019.05.014.

Principal Author

Name of Principal Author (Candidate)	Shaun Fitzgerald		
Contribution to the Paper	Co-designed the research concept. Reviewed the literature and developed calculations for flow in a velodrome bend. Developed the experimental equipment for the bicycle. Conducted the experimental testing and completed all data analysis. Prepared the manuscript and generated all figures. Acted as corresponding author.		
Overall percentage (%)	80		
Certification:	This paper reports on original research I conducted during the period of my Higher Degree by Research candidature and is not subject to any obligations or contractual agreements with a third party that would constrain its inclusion in this thesis. I am the primary author of this paper.		
Signature		Date	12/11/2021

Co-Author Contributions

By signing the Statement of Authorship, each author certifies that:

i. the candidate's stated contribution to the publication is accurate (as detailed above);

ii. permission is granted for the candidate in include the publication in the thesis; and

iii. the sum of all co-author contributions is equal to 100% less the candidate's stated contribution.

Name of Co-Author	Richard Kelso		
Contribution to the Paper	Co-designed research concept. Guided research direction, supervised work development and interpretation, helped generate ideas and concepts, and edited the manuscript.		
Signature		Date	15/11/2021

Name of Co-Author	Paul Grimshaw		
Contribution to the Paper	Guided research direction, supervised work development and interpretation, helped generate ideas and concepts, and edited the manuscript.		
Signature		Date	15/11/2021

Name of Co-Author	Andy Warr		
Contribution to the Paper	Guided research direction, supervised work development and interpretation, helped generate ideas and concepts, and edited the manuscript.		
Signature		Date	16/11/2021

Measurement of the air velocity and turbulence in a simulated track cycling team pursuit race

S. Fitzgerald, R. Kelso, P. Grimshaw, A. Warr

Abstract

There are many cycling events undertaken in a velodrome which involve close interactions between cyclists. During a single race, particularly the team pursuit, a cyclist can alternately be ahead of or behind another rider; two positions which have very different flow fields. Additionally, as a cyclist travels around a level corner, the relative flow experienced by the cyclist becomes curved. Due to the lean angle of the cyclist, this resolves into a change in both the yaw and pitch angle as well as the flow speed relative to the cyclist. An experimental investigation was conducted with a bicycle fitted with a three-component velocity probe placed anterior to the rider in a simulated team pursuit race. The results demonstrate a reduction in the airspeed-to-wheel speed ratio for each drafting cyclist, down to 46 % for the 4^{th} rider. The turbulence intensity increased for each drafting position, from 1.5 % to 18.5 %. A yaw angle of up to 7° and pitch angle of −3° were observed on the velodrome bends. In addition, a fluctuation in the yaw angle due to the cadence cycle was observed. The results demonstrate the aerodynamic conditions experienced in track cycling and can be used to inform further investigations.

3.1 Introduction

At typical race speeds, aerodynamic drag accounts for greater than 90 % of the total resistive force on a cyclist and the power required to maintain a constant speed is proportional to the velocity cubed [1]. Numerous methods have been proposed to reduce the aerodynamic drag of a cyclist, both in the academic literature and in industry [38]. However, the majority of these studies have been conducted with a number of assumptions on the aerodynamic environment experienced by the cyclist and bicycle, most notably for track cycling being that the only component of airflow is a direct headwind equal to the cyclists' velocity. However, if there is an external factor affecting the airflow, then there will be an angle of incidence between the airflow relative to the cyclist and their direction of travel. This angle can be split into two components; the yaw and pitch angles, where yaw is the angle between the

direction of motion and the relative wind in the transverse (xy) plane, and pitch is the angle in the sagittal (xz) plane, both shown in Figure 3.1.

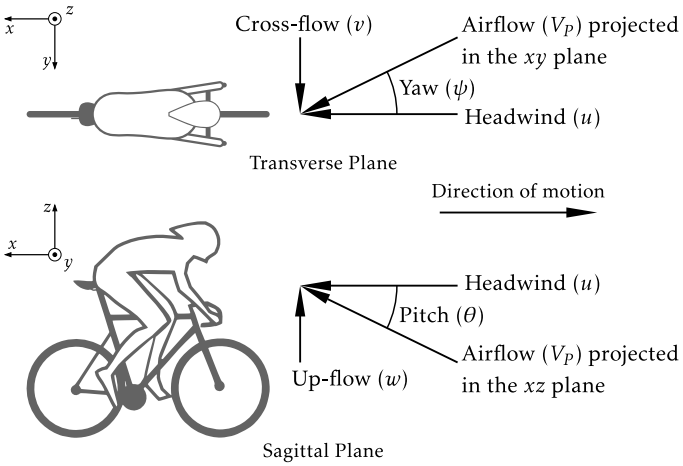


Figure 3.1 The three components (u, v, w) of total air velocity (V_P) and the yaw (ψ) and pitch (θ) angle definitions. The xyz coordinates are defined relative to the cyclist.

During outdoor cycling, yawed airflow typically occurs as a result of a natural cross wind; however, within an indoor velodrome there is no natural wind and the current industry standard is to assume there is no yawed or pitched airflow [9, 11, 43]. This assumption greatly simplifies the aerodynamic analysis of track cycling but it may not accurately model the realistic situation, as shown in a study by Kyle [37] where the airflow around a velodrome was observed by recording the wind angle anterior to the handlebars of a bicycle as it traversed a track. Kyle [37] proposes that this yaw angle arises due to the bicycle turning on a track, shifting the incoming wind direction and causing a yawed flow relative to the bicycle as the track curves. To the best of the authors' knowledge there have been no other previous studies on the airflow experienced by a cyclist during cornering. Similar work has been completed in the automotive field on the effects of cornering, notably by Keogh et al. [75] who completed a Computational Fluid Dynamics (CFD) analysis of curved airflow over a generic vehicle four-wheeled (Ahmed) body. Comprehensive studies on the wake of a single cyclist have been completed by a number of groups [48, 49, 124], however these studies have all been completed in a wind tunnel with straight, consistent airflow. The study by Keogh et al. [75] on an Ahmed body demonstrated a significant difference in the flow field and aerodynamic forces due to the influence of curved airflow over the length of the vehicle body. Whilst there are obvious differences in the geometry and lean angle for a vehicle body compared to a cyclist, the clear differences in the

wake for curved flow compared to straight flow demonstrates the requirement to accurately model the true aerodynamic conditions.

The effects of yawed airflow on the aerodynamic drag of a cyclist has previously been studied by Íñiguez-de-la-Torre and Íñiguez [77] who found that with an increasing crosswind there was an increase in the drag force on a cyclist. These authors assumed a constant coefficient of drag and frontal area (i.e. constant C_DA) for all yaw angles, but this may not accurately replicate the true conditions where the C_DA for a cyclist can be highly dependent on the yaw angle [30, 31] and the total drag could decrease at higher yaw angles due to a lower C_DA.

Previous studies in cycling have used wind tunnels or CFD codes with low turbulence intensity, namely 0.2 % [32, 97], 0.5 % [124], 1.4 % and 1.6 % [48]. However, there is often little discussion about why these values were chosen, and the true turbulence levels experienced by a cyclist on the road or in a velodrome have not been measured. The measurement and replication of turbulence is an area that has been extensively studied in other contexts, such as wind engineering where an understanding of the atmospheric boundary layer has been an industry standard for decades, and in vehicle aerodynamics where the turbulence relative to a moving vehicle has been extensively studied [65]. However there is a lack of turbulence measurements in regards to sports, an exception being work by Watkins and Alam [59] who provide a theoretical review of possible sources of turbulence. Crouch et al. [38] also mention that the turbulent flow field inside a velodrome is not well understood and could arise from natural or forced convection and the wakes of other cyclists. This could have an impact on many techniques for reducing the aerodynamic drag of a cyclist which involve 'tripping' the boundary layer into turbulence where the effects of freestream turbulence are known to induce this transition at lower speeds [38].

A series of studies investigated the effects of turbulence on the drag of speed skaters on a skating rink using a three-component velocity probe [69, 70]. In these investigations it was found that the airflow around a speed-skating rink is highly turbulent and there are components of yawed airflow relative to the skater around the corners. These authors describe a turbulent flow created by the skaters circling the track. This turbulence is caused by the skaters, structures surrounding and inside the track, and the temperature gradient from the surface of the ice. D'Auteuil et al. [70] replicated their characterised on-track turbulence in a wind tunnel and observed a significant difference in the drag force on a mannequin in turbulent flow compared to smooth flow, highlighting the importance of correctly measuring and replicating the flow conditions. Track cycling operates in

a similar environment and Reynolds number regime to speed skating and, with the exception of the temperature gradient due to ice, is likely to induce a similar turbulent flow pattern around the track.

Extensive work on the influence of drafting on the reduction of aerodynamic drag for a cyclist has been completed by previous authors for two cyclists [89, 93], four cyclists [90, 92, 95], or more up to a full peloton [32, 97]. For a comprehensive review of the effects of drafting see Fitton et al. [95] and Crouch et al. [38]. Work on the influence of a cyclist's posture and position within a group has been completed by Defraeye et al. [90] who observed a difference in drag reduction dependent upon the relative position of different riders. An experimental study was competed on the wake interactions between two tandem cyclists by Barry et al. [93] who found that the wake behind a second cyclist maintains strong similarity to that of a single cyclist for large separation distances and deviates from the single cyclist wake for close separation, largely regardless of leg position. Work has also been completed for a pace line of up to 9 riders by Blocken et al. [97] who demonstrated a decreasing drag force from the 1^{st} to 4^{th} rider before the relative drag plateaus and all riders from 5^{th} to 9^{th} have a very similar drag force. A limitation in all of these studies on drafting is that they only consider a simple headwind equal to the cyclist's speed. If a crosswind is present then the drafting effect is likely to be reduced due to the wake from the leading cyclist being offset by the yaw angle, limiting the aerodynamic shelter provided to the trailing riders. This is observed in work by Belloli et al. [138] who measured the drag of two cyclists for yaw angles of 0°, 3° and 5° and found a diminishing drag reduction effect at increasing yaw angles.

To the best of the authors' knowledge, there have been no previous studies that measure the aerodynamic flow field anterior to a cyclist in-situ during a team pursuit event inside a velodrome. The present study aims to investigate the aerodynamic conditions experienced by a track cyclist in order to further our understanding of the true flow field conditions experienced inside a velodrome. A developed understanding of these aerodynamic conditions will enable the flow field to be simulated more effectively in further wind tunnel or CFD-based research.

3.1.1 Cornering theory

For this work, two right-handed Cartesian coordinate systems will be used. The first is a non-inertial body coordinate system (xyz) fixed in origin and orientation to the bicycle and cyclist system, as shown in Figure 3.1. Here the x-axis is directed to the posterior of the cyclist, the y-axis is directed to

the cyclist's right and the z-axis is directed upwards. The airflow experienced by a cyclist is composed of three components; u, v, w that correspond to the three primary axes x, y, z respectively. The second system is a ground-based inertial coordinate system (ijk) that is fixed with its origin at the centre of a velodrome. Here i is directed towards the centre of a straight, j is directed away from the centre of a bend, and k is directed upwards.

Figure 3.2 shows the steady-state cornering condition for a leaning cyclist turning at a constant speed around a level corner in still air. The cyclist rotates at a constant rotational velocity about an external point, the Centre of Rotation (CR), and the relative airflow is equal and opposite to the velocity of the Centre of Gravity (CG) of the cyclist. This results in curved airflow with a variation in the airflow angle and magnitude over the length of the cyclist and bicycle. Assuming an anti-clockwise corner, then anterior to the cyclist there will be an airflow angle (τ) in the horizontal (ij) plane. This airflow initially comes from the cyclist's left, transitions to a zero angle at the CG, and then exits towards the cyclist's left when it is posterior to the CG, as shown in Figure 3.2. As a cyclist leans during cornering, this angular airflow across the cyclist and bicycle results in both a yaw and a pitch angle. In addition to the change in direction, the magnitude of the airflow, and hence the dynamic pressure, will increase with radial distance from the CR. Due to the substantial lean angle of a track cyclist relative to the horizontal plane, this change in magnitude results in a slower air velocity at the top of the cyclist's body than at the wheels.

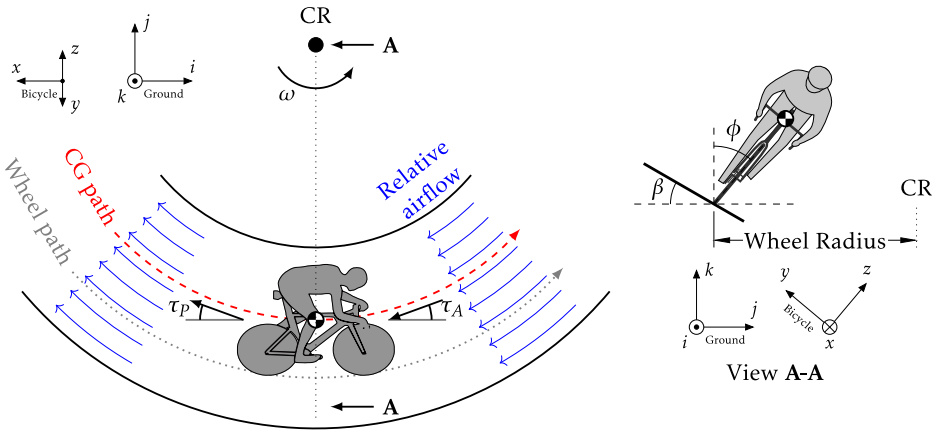


Figure 3.2 The steady-state airflow distribution observed by a leaning bicycle and cyclist on a corner of constant radius. Not to scale. Coordinate systems are shown displaced from their origin.

Shown in Figure 3.3 is the free-body-diagram of a steady-state cornering cyclist represented as a point mass. Representing a cyclist as a single point

mass is a simplistic model as factors such as bicycle geometry, wheel path, rider size and rider position, can affect the validity of calculations, however it has been shown to provide a high level of accuracy [12] and as such will be used in this research.

When a cyclist traverses a bend, a centrifugal force ($F_C = mV_{CG}/R_{CG}$) acts radially outwards from the CR. This force produces a moment about the wheelbase which is counteracted by the cyclist leaning into the corner and using their weight force ($F_W = mg$) to create a counter-moment to prevent the bicycle from tipping. Due to the flow curvature, there will be a horizontal aerodynamic force ($F_{A(\tau)}$), acting at the centre of pressure (CP), that is dependent on the angle of airflow. Anterior to the CG, this force will be directed outwards from the CR and posterior to the CG it will be directed inwards, producing a clockwise yawing moment about the k-axis. Additionally, due to the radial change in airflow magnitude, there is a higher mean pressure on the inward side of the cyclist than the outward side. This pressure difference will produce an aerodynamic force acting outwards from the centre of rotation ($F_{A(P)}$) [75]. The magnitude of $F_{A(P)}$ is small in comparison to F_C and is omitted for the following theoretical calculations.

Due to the lean of the bicycle, the radius of the CG (R_{CG}) is less than the radius of the wheel/track contact point (R_W). Assuming that the turn radius of the wheels equals the radius of the black line on the velodrome track and if the height of the CG (h_{CG}) is known, then the lean angle (ϕ) for a given wheel velocity V_W can be calculated using Equation (3.1). This equation is implicit in ϕ and so requires an iterative method to solve, however it converges to 99 % of its final value in less than 3 iterations.

$$\tan\phi = \frac{V_W^2(R_W - h_{CG}\sin\phi)}{gR_W^2} \tag{3.1}$$

Figure 3.3 defines point P, a horizontal distance L_P anterior to the CG and a distance h_P above the wheelbase, and point P^*, the intersection of a horizontal line through P and a line from the CG to the ground. The points P and P^* have the same angular velocity but with turn radii of R_P and R_{P^*} respectively. As such there is a component of cross-flow (V_{P_j}) at point P which induces a yawed and pitched airflow relative to the bicycle. The cross-flow angle in the horizontal (ij) plane can be calculated with

$$\tan\tau = \frac{L_P}{R_W - h_P\sin\phi}. \tag{3.2}$$

and the velocity at P can be calculated by

$$V_P = \frac{V_W}{R_W}\sqrt{L_P^2 + \left(R_W - h_p\sin\phi\right)^2}. \tag{3.3}$$

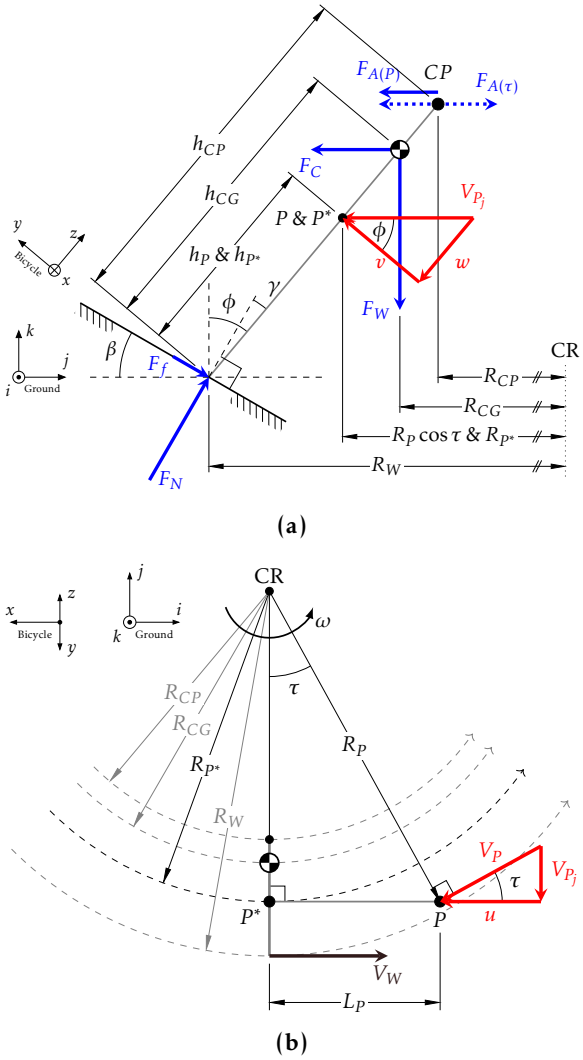


Figure 3.3 The steady-state free-body diagram of a bicycle traversing a level banked corner with the positions of the CR, CP, CG, P and P^*. **(a)** Front view showing the lean angle (ϕ), bank angle (β), wheel camber angle (γ) and various different turn radii. The force vectors in blue show the centrifugal force (F_C), weight force (F_W), aerodynamic force due to flow curvature ($F_{A(\tau)}$), aerodynamic force due to radial pressure ($F_{A(P)}$), normal force (F_N) and tyre friction force (F_f). The airflow velocity vectors in red show the bicycle-coordinate relative velocity components (v & w) that compose the lateral velocity (V_{P_j}) due to cornering. **(b)** Plan view showing the velocity of the wheels (V_W) and the different turn radii about the centre of rotation. The velocity of the probe (V_P) is composed of u and V_{P_j} and acts normal to the line between P and CR.

The yaw angle can then be calculated with

$$\psi = \tan^{-1}\frac{v}{u} = \tan^{-1}(\tan\tau\cos\phi), \tag{3.4}$$

and the pitch angle by

$$\theta = \tan^{-1}\frac{-w}{u} = \tan^{-1}(-\tan\tau\sin\phi). \tag{3.5}$$

Inputting values to be used later in this paper, for a cyclist travelling at $V_W = 14.7$ m/s with $R_W = 22.5$ m, $h_{CG} = 1$ m, $h_P = 0.660$ m, and $L_P = 0.9$ m this equates to $V_P = 14.4$ m/s, $\psi = 1.7°$, and $\theta = 1.6°$ in the centre of the bends and $V_P = V_W$, $\psi = \theta = 0°$ in the straights. Details of the track geometry and h_P were directly measured, while h_{CG} and L_P were estimated from cyclist body measurements.

An experimental test was conducted to measure the airflow on a bicycle ridden around a velodrome. The measurements were taken at the point P with a probe fixed to the frame of the bicycle so that it moved with the bicycle coordinate system and measured the air velocity relative to the cyclist.

3.2 Methods

Data was collected using a four-hole pressure probe (45 m/s, 150 Hz, Cobra probe, TFI, Australia) that measures the three components of velocity. This was fixed to an aluminium arm cantilevered anterior to the head tube of a generic track bicycle (size medium Pista, Hillbrick, Australia) and was used to measure the airflow relative to the bicycle in the body-centred xyz coordinate system. A reference static pressure was supplied to the Cobra probe via a static pressure probe attached to the forward component of the aluminium arm. The forward limit of the Cobra probe and static port were constrained by remaining behind the leading edge of the wheel to ensure the bicycle did not impact with another bicycle during team pursuit transitions. Two Hall-effect sensors were attached to the frame with a corresponding magnet on the rear wheel and the left crank arm to measure the wheel-speed and a pedal cadence respectively. The velocity probe and Hall-effect sensors were sampled at a frequency of 1250 Hz and were controlled by a TFI Data Acquisition System (DAQ) and laptop that was carried in a backpack by the rider. The total mass of the instruments was approximately 4 kg and the bicycle setup for testing is shown in Figure 3.4. The position of the Hall-effect sensor on the frame was known and by assuming a constant rotational velocity of the cranks during a single pedal cycle the leg position at any point in the cycle was estimated.



Figure 3.4 The instrumented bicycle with the position of the probe tip.

Stationary testing of the instrumented bicycle was completed at the University of Adelaide Thebarton wind tunnel. This is a closed-return wind tunnel with a cross sectional area of 2.75 m × 2 m, a maximum speed of 30 m/s and turbulence intensity <0.5 %. The bicycle was held on a fixed stand in the tunnel and tested with the probe in position with no rider, a rider sitting still, and a pedalling rider; all in conditions of 0° yaw.

On-track testing took place at the Adelaide Super-Drome, a 250 m indoor velodrome with bends of a maximum bank angle of 43° and minimum turn radius of 22.5 m. Four international-level elite male cyclists were used in this testing. The athletes provided informed consent and testing was conducted according to the University of Adelaide Human Research Ethics Committee guidelines. The first athlete rode the instrumented bicycle whilst the other three athletes rode their typical track bicycle. The athletes assumed their typical riding posture and rode in a team pursuit formation for 16 laps (4000 m) from a standing start in simulation of a competitive event. The team changed position every two laps so that data was collected twice at every position along the team line. The athlete on the instrumented bicycle led out the team in position 1 at the start of the race. Over the final 50 m the team abandoned the strict linear formation and the leading three riders spread out across the track to cross the pursuit line, in simulation of a competitive finish. The testing was filmed using a high-definition camera at 50 frames per second and the timestamp visually synchronised with the velocity probe data to find lap and position change times. Two races were completed with identical

conditions, both producing very similar results indicating repeatability and confirming the results, with one of the tests detailed in this article.

The flow measured by the velocity probe was found to be highly periodic and hence the measured velocity components were split into their periodic and turbulent components by

$$f(t) = f + f' \tag{3.6}$$

for $f = u, v, w, \psi, \theta$ [139]. Here f is the phase average value of the flow at a given time t and f' is the turbulent velocity fluctuation at t. Two different phase average time-series were obtained by twice applying a Savitzky-Golay filter with a quartic polynomial and two different window sizes for laps 2 to 16 [140]. The first lap was omitted as it was an acceleration phase. The first window is equal to the mean pedal cycle period of 0.56 s (108 rpm) and the second window is equal to the mean lap time of 17.27 s. The principal turbulence intensity was then calculated by the turbulent variation of the flow about the phase-averaged value with

$$I_{uvw} = \frac{1}{\overline{V_P}} \sqrt{\frac{1}{3}\left(\overline{(u - \langle u \rangle)^2} + \overline{(v - \langle v \rangle)^2} + \overline{(w - \langle w \rangle)^2}\right)}. \tag{3.7}$$

The alignment of the pressure probe to the bicycle coordinate system provides the greatest source of error in this experiment and has the potential to affect the absolute values of yaw and pitch. The probe was mounted to an aluminium arm cantilevered out from the head tube of the bicycle and aligned parallel to the bicycle and level. To align the probe, the bicycle was first geometrically aligned along the centreline of the University of Adelaide's 0.5 m × 0.5 m wind tunnel. This tunnel is far smaller than the bicycle, however it provided ease of alignment and the probe tip was encased in a low turbulence, well-conditioned airflow, unaffected by the asymmetric crankset and chain drive. The yaw angle of the probe was then aligned with the flow and marked in position with several scribe marks which were used to realign the probe before in-field testing at the velodrome. The pitch angle was dependent on the trueness of the hole in the cantilever arm and the level of the arm relative to the ground. The probe was removed from the bicycle and replaced in the wind tunnel multiple times to determine the accuracy of this method. A conservative estimate for maximum absolute error in yaw and pitch for placement of the probe is <2°. The effect of this error would be to linearly translate the results by the misalignment of the probe and would not alter the relative changes in yaw and pitch observed during a test. The probe manufacturers claim an accuracy of ±0.3 m/s and ±1.0° for the flow range of 2–45 m/s in a ±45° cone.

3.3 Results and discussion

3.3.1 Stationary wind tunnel testing

Stationary testing conducted in the 2.75 m × 2 m Thebarton wind tunnel showed a deceleration of the air velocity at the probe tip, shown in Table 3.1 for V_P / V_T where V_P is the measured probe velocity and V_T is the freestream velocity of the tunnel measured by a Pitot-static tube. This upstream disturbance can be seen to be partly due to the bicycle only and partly due to the influence of the rider. The yaw angle of 1.2–1.4° is due to misalignment of the probe or asymmetries in the flow and bicycle. The pitch angle of 4.63° with no rider is likely due to these same factors in addition to the presence of the front wheel which causes an upwards deflection of the flow. When the rider is present there is a decrease in the pitch angle of 1.8° due to the upstream influence of the rider's arms and hands turning the airflow down towards the ground.

Table 3.1 Summary of data from stationary testing of the instrumented bicycle (Mean ± Standard Deviation). Values are obtained by averaging results across tunnel velocities of 9, 11, 13 and 15 m/s.

Rider	V_P / V_T	I_{uvw} [%]	ψ [°]	θ [°]
None	0.979 ± 0.0020	0.276 ± 0.037	1.19 ± 0.02	4.63 ± 0.07
Still	0.956 ± 0.0004	0.269 ± 0.020	1.19 ± 0.04	2.82 ± 0.05
Pedalling	0.954 ± 0.0021	0.775 ± 0.284	1.39 ± 0.02	2.83 ± 0.04

In order to observe if there were any periodic components to the airflow a Fourier transform was applied to the three principal components of velocity, shown in Figure 3.5 for both a rider sitting still (cranks horizontal) and a rider pedalling. In these graphs there is a distinct spectral peak at 3.8 Hz for the u component that is also seen when no rider is present (not shown) and is likely due to a perturbation in the tunnel flow. There is an unknown frequency at 93.7 Hz that is also observable in the velocity data obtained on the track, the cause of which is unknown but could be due to vibration in the probe or bicycle frame.

There is a relative airflow periodic dependence on the rider's cadence, with a peak in the yaw that matches the cadence frequency and peaks at approximately twice the cadence frequency in the total velocity and pitch. This periodic motion is hypothesised to be due to the upstream influence of the rider's legs. During each pedal cycle, one leg will be forwards while the other is rearwards, producing an asymmetric upstream effect which induces a

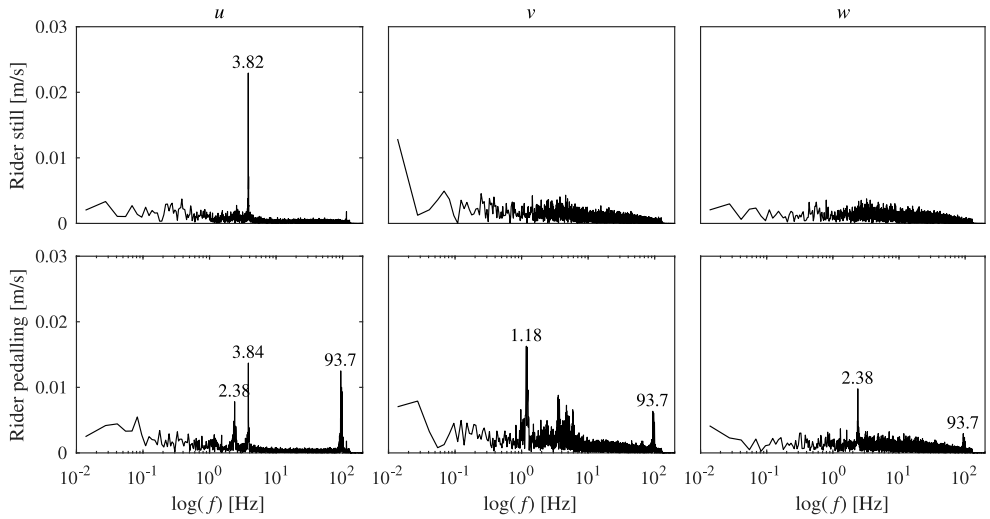


Figure 3.5 The Fourier Transform of the three components of velocity (u, v, w) for stationary testing completed in the wind tunnel at a freestream velocity of 15.0 m/s. The top row is when the rider is sitting still on the bicycle and the bottom row is when the rider is pedalling at an average cadence of (1.20 ± 0.03) Hz $((71.7 \pm 1.8)$ rpm). Notable frequencies are labelled.

periodic yaw angle fluctuation. As one leg produces a positive ψ and the other a negative, the yaw period matches the cadence period. However, the V and θ periodicity are likely due to the forward and vertical motion of each leg and, as these are independent of a particular leg, their period is twice the cadence frequency. Whilst these periodic motions are observed, their amplitudes are small (<0.01 m/s and <0.08°), not greatly above the background turbulence, and hence are likely to have minimal impact on a cyclist.

3.3.2 Velodrome testing

The velodrome testing results indicate that the airflow is highly variant and dependent on three main factors, listed in order of relative magnitude; the rider's position in the team line, their location on the track, and the point in their cadence cycle. Displayed in Figure 3.6 are the three components of air velocity and the wheel speed for the duration of the 16-lap test, showing the clear differences due to position in the team.

A useful metric for this testing is the ratio between the probe velocity and the wheel velocity, V_P / V_W. This represents the relationship between the airflow experienced by the cyclist and their speed over the track. This ratio can be observed in Figure 3.6 by the difference in speed between u and V_W for position 1. In an ideal environment V_P / V_W should be unity, but there

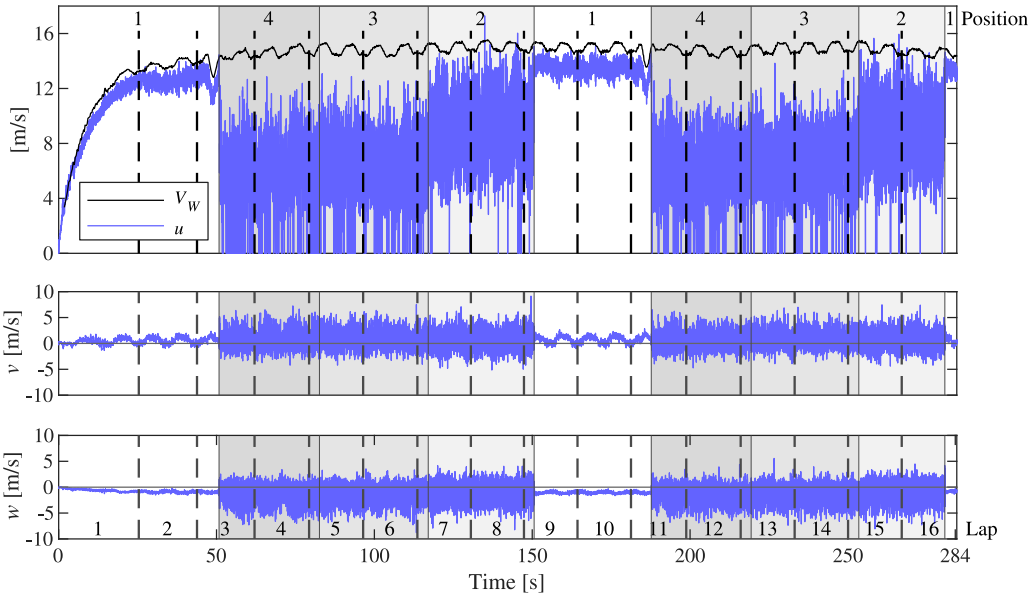


Figure 3.6 The three components of air velocity as well as the wheel speed for the length of a simulated team pursuit race. Lap markers are indicated by the dashed vertical lines and the bottom numbers 1 to 16. The bicycle's position along the team line is indicated by the shaded areas and the top numbers 1 to 4.

are a number of factors that influence this. The most significant contribution arises from the upstream disturbance of the bicycle and cyclist slowing the airflow at the probe tip. A summary of stationary testing completed in the 2.75 m × 2 m wind tunnel, shown in Table 3.1, demonstrates the deceleration of the air velocity at the probe tip. This deceleration of the airflow ahead of the rider has been previously reported by Blocken et al. [32] who used Computational Fluid Dynamics (CFD) calculations to measure the streamwise component of airflow at three different distances ahead of a cyclist in a peloton at 15 m/s and across the full height of a cyclist in the sagittal plane. The mean value for each distance was plotted and for the rider at the front in clear airflow $V_P / V_W = 0.97$. The distances of the planes ahead of the rider are not presented; however, they are likely to be further ahead of the rider than P and so the airspeed deceleration at P is likely to be greater. A second difference between V_P and V_W is seen in the earlier theoretical calculations which predicted $V_P / V_W = 0.98$ due to the faster speed at the wheels than P when on the bends.

3.3.3 Effect of rider position

Observing Figure 3.6, the clearest trends are seen in the effect of rider position on the three components of air velocity. When the cyclist is in position 1, they are leading the team and the magnitude of the air velocity is relatively close to the wheel speed. However, when they move to the rear of the team pursuit line in position 4, the headwind is much lower than the wheel speed and the turbulence intensity greatly increases: values are provided in Table 3.2. This is due to the cyclist riding in the wake/s of the three preceding riders who produce highly turbulent and attenuated airflow. As the next rider changes position and the instrumented bicycle moves to position 3, there is minimal difference in the air velocity and turbulence intensity compared to position 4. After the third transition, when the instrumented bicycle is in position 2, there is a clear difference to both positions 3/4 and 1. In position 2 there is still a high turbulence intensity and the air velocity is lower than when they are at position 1, but not as low as positions 3 or 4. This demonstrates that the wake from the leading cyclist compounds with that of the second cyclist to retard the airflow further for the third and fourth cyclists. This is also seen in the increase in the pitch angle through positions 1 to 4, indicating that the downwash from each rider compounds to further increase the downwards airflow as measured by the following rider. However, after three riders the effect of a change between positions plateaus and the pitch angle and turbulence intensity increase at a slower rate.

The observed change in the airflow between different positions along the team pursuit line is similar to previous work in the literature on the relative drag force experienced at different positions in the line, as shown in Table 3.2. The drag force for a rider in a given position along the line is provided relative to the drag of that rider on their own by F_{pos}/F_i where F_{pos} is the drag of the cyclist in a given position and F_i is the drag of the same rider on their own. From Table 3.2 it can be seen that the drag reduction increases from first to third position before plateauing from third to fourth position, mirroring the relative airflow observed in the present experiment. The cause of this drag reduction is the greatly reduced dynamic pressure in the wake of the preceding cyclist, shown here as a reduction in V_P for each subsequent rider. This work cannot provide an accurate indication of the drag force as only a single point of the flow experienced by a cyclist was measured; however, it provides a simple indication of the expected flow field.

Table 3.2 Average aerodynamic factors at each position along the team pursuit line from this study (Mean ± Standard Deviation) and $F_{\text{pos}} = F_i$ for each position along the line from a) wind tunnel testing [92], b) CFD testing [32], c) CFD testing [97], and d) in-situ velodrome testing [95]. Position 1 includes the acceleration phase.

Position	1 (Front)	2	3	4 (Rear)
V_W [m/s]	13.20 ± 2.76	14.91 ± 0.33	14.87 ± 0.31	14.67 ± 0.31
V_P [m/s]	12.10 ± 2.46	9.33 ± 1.81	7.06 ± 1.56	6.72 ± 1.62
ψ [°] (Str)	0.68 ± 2.72	1.35 ± 8.81	4.25 ± 10.46	2.69 ± 11.01
ψ [°] (Bnd)	4.18 ± 2.55	5.76 ± 8.29	8.04 ± 10.08	6.98 ± 11.62
θ [°] (Str)	-1.47 ± 0.93	-2.94 ± 8.96	-5.15 ± 11.09	-6.52 ± 11.70
θ [°] (Bnd)	-2.20 ± 0.86	-4.43 ± 8.71	-8.67 ± 10.70	-9.87 ± 11.73
I_{uvw} [%] (Cad)	1.5	14.9	17.3	18.5
I_{uvw} [%] (Lap)	3.2	16.1	19.0	20.3
V_P / V_W	0.92	0.63	0.47	0.46
F_{pos} / F_i[a]	0.95	0.55	0.45	0.43
F_{pos} / F_i[b]	0.98	0.59	0.50	0.46
F_{pos} / F_i[c]	0.98	0.62	0.50	0.47
F_{pos} / F_i[d]	0.96	0.58	0.52	0.53

3.3.4 Effect of location on the track

There is a significant dependence of the airflow on the cyclist's location around the track that is clearly evident when observing the yaw and pitch angles during a lap with the instrumented bicycle in position 1, shown in Figure 3.7 for lap 10. The yaw and pitch angles are highly periodic in nature, with a clear dependence on both the turn location and cadence cycle. Shown in Table 3.2 are the yaw and pitch angles for each of the four positions, split into the averages for when the cyclist is on the straights and the bends. When the cyclist is turning around the bend, a significant increase in the yaw angle, an increase in the pitch angle magnitude, and a minor increase in the wheel speed is observed.

The increase in the yaw angle is much greater than the theoretically calculated value of 1.7° (Equation (3.4)) and could be due to a variety of factors. When cornering, the cyclist will steer the front wheel into the bend and the large surface of the disk wheel would induce a positive yaw angle at the probe tip. Additionally, due to the cyclist riding in a curved flow field rather than a straight headwind, the stagnation point would move from directly anterior to partially around to the left, inducing a positive yaw angle at the position of the probe.

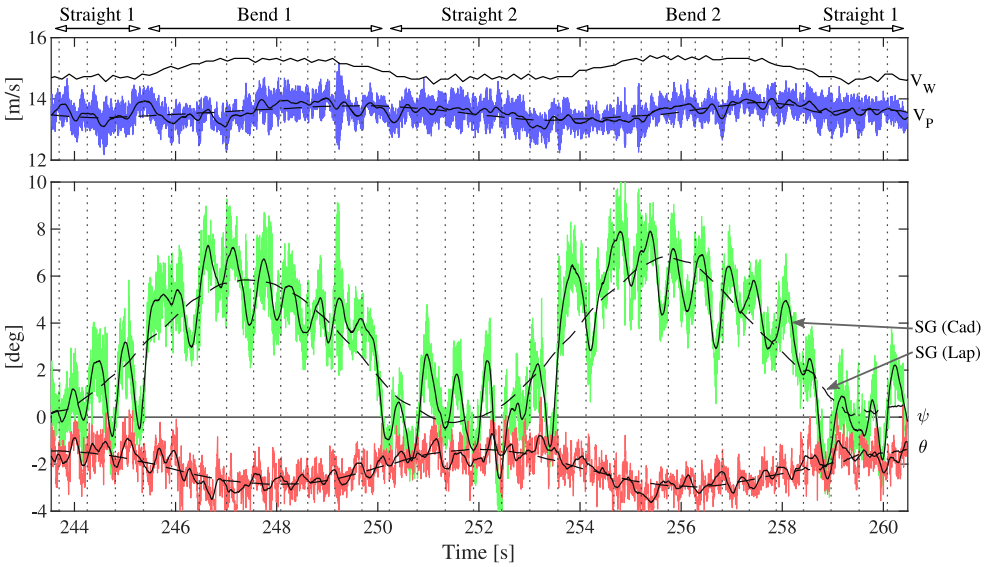


Figure 3.7 Velocity of the wheels (V_W), total velocity (V_P), yaw (ψ) and pitch (θ) over the course of a single lap (lap 10, position 1). The solid black lines represent the Savitzky-Golay filtered data with a window size equal to the cadence period and the dashed black lines are the filter with a window size equal to half of the lap time. Vertical dotted lines are indications of when the left leg is at top-dead-centre (TDC).

Close examination of Figure 3.7 shows that the yaw angle undergoes a rapid change at the entries and exits of the bends. At these locations on the track the rider undergoes a transition from an upright position ($\psi = 0$) to a lean angle of approximately 40° and then back when exiting. Thus, the rider will experience a roll-induced yaw at these locations. The roll-induced yaw will vary from zero at the track surface to a maximum at the rider's head and shoulders, and at the probe height this equates to approximately 2–4°.

In order to better visually display the effect of track location on the yaw and pitch angles, a novel method of displaying the results has been developed and is shown in Figure 3.8. This velodrome plot is based on a number of assumptions and as such is only to be used for qualitative purposes in identifying the major trends. It is produced by approximating the track as two straights and two semicircles and assumes a constant wheel speed based on the lap time and track geometry. The yaw/pitch angle vs time data is then converted to yaw/pitch angle vs lap distance with the lap position shown by the solid black line and the angular magnitude represented by the radial distance from that line. This graph clearly shows the correlation between the yaw and pitch angles and the cyclist's position on the bends and straights. Also shown is the data from the second test which can be seen to follow a very

similar trend to the first test.

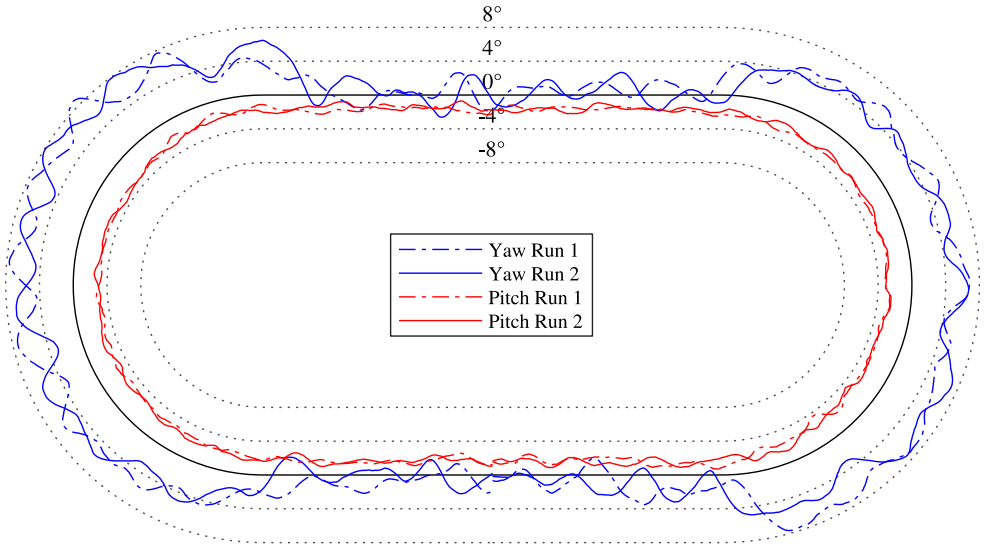


Figure 3.8 The cadence-filtered yaw and pitch angles for lap 10, when the cyclist is in position 1, from both tests, displayed in a velodrome plot.

In order to further investigate the cyclic nature of the velocity field, a Fourier transform was applied to the yaw and pitch data, excluding the first lap which was an acceleration phase, and the results are shown in Figure 3.9. In this figure two clear peaks in the yaw angle signal and a single peak in the pitch angle signal can be observed. The first peak in the yaw angle and the peak in the pitch angle occur at a frequency of 0.116 Hz which corresponds to a lap time of 17.271 s. The mean lap time for laps 2 to 16 was 17.273 s, a 0.01 % difference, showing a clear dependence of the yaw and pitch angles on the bank angle and turn radius. There are also two minor peaks after the cadence peak which are at twice and three times the cadence frequency.

3.3.5 Effect of pedal cycle

The above measurements demonstrate that a significant component of the airflow unsteadiness is related to the cyclist's pedalling cadence with a periodic change in yaw angle that closely follows the cadence frequency. This is clearly seen in the filtered yaw angle from Figure 3.7 where a small-amplitude and high-frequency wave from the cadence cycle is overlaid on top of a high-amplitude and low-frequency wave from the lap cycle. A periodicity can also be visually observed that matches the cadence markers.

The second peak in the Fourier transform of the yaw signal in Figure 3.9 has a frequency of 1.81 Hz which corresponds to a cadence of 108.6 rpm, a

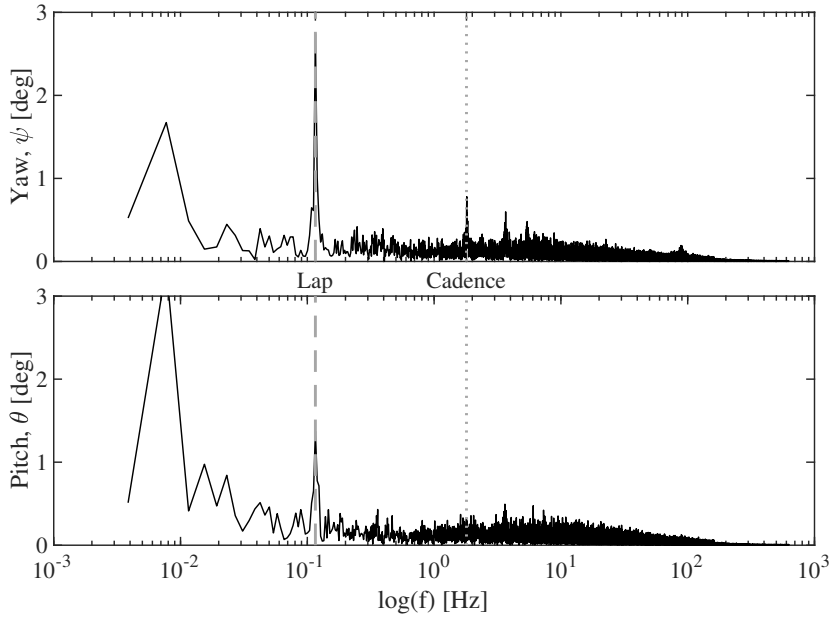


Figure 3.9 Fourier transform of the yaw (ψ) and pitch (θ) angles for laps 2 to 16. The dashed line indicates the measured mean half-lap frequency of 0.116 Hz, and the dotted line indicates the measured mean cadence frequency of 1.80 Hz (108.0 rpm).

difference <0.6 % from the measured mean cadence of 108.0 rpm, implying a clear dependence of the yaw angle on the leg position. The amplitude of this oscillation is 2.75° which is much greater than the 0.07° observed in the wind tunnel, indicating the influence of a secondary factor. The local peak in the yaw angle was estimated to occur when the left leg is 120° forward of top-dead-centre (TDC). Of note is that there is no clear dependence of the pitch angle on the cadence cycle from on-track testing.

The cause of the variation in yaw angle due to the cadence cycle is unknown but it is proposed that it arises due to rocking and weaving of the bicycle as the cyclist pedals. The local maximum in the yaw angle occurs at an approximate leg position of 120° which is just past the centre of the power stroke for the right leg. As a cyclist pushes down with their right leg, the bicycle rocks to the left, sweeping the probe tip laterally right to left, inducing a positive yaw angle with a maximum value at the centre of the power stroke when the bicycle is rocking at the greatest velocity. This process is then mirrored in the second half of the pedal cycle, producing a low magnitude sinusoidal yaw angle of frequency equal to that of the pedal cycle. Preliminary investigations in the 2.75 m × 2 m wind tunnel qualitatively

support this hypothesis and further research would require measuring the crank angle at a higher resolution and recording both the steering angle and the roll angle of the bicycle.

The turbulence intensity has been calculated twice using the filtered signal with both the lap and cadence windows, as shown in Table 3.2. This, combined with the turbulence intensity measured in the wind tunnel, can be used to differentiate the causes of turbulence. By subtracting I_{uvw} (Cadence) from I_{uvw} (Lap) the turbulence intensity due to only the cyclists' cadence is found to be 1.2 %. From the wind tunnel testing, it was observed that the pedalling motion produced a turbulence intensity of 0.5 % above the background tunnel turbulence. As such, it can be seen that the turbulence associated with the periodic velocity fluctuations due to pedalling can be partially attributed to the movement of the legs and partially due to other factors. This has an impact on wind tunnel or CFD investigations where the background turbulence is required to be simulated.

3.3.6 General discussion

The data acquisition system contained in the backpack could influence the results through two different methods. Firstly, the added mass on top of the rider's back would slightly alter the position of the centre of gravity, thereby changing the expected yaw and pitch values due to an altered lean angle. This effect was calculated with Equations (3.1) to (3.5) and a 10 % change in centre of gravity height, much more than possible from the backpack, produces a <0.2 % change in yaw and pitch angles. Secondly, the size and shape of the backpack could have an upstream aerodynamic effect at the probe tip. The influence of this is expected to be minimal due to the much larger body of the cyclist between the backpack and the probe producing the greatest upstream aerodynamic influence. In order to qualitatively assess this behaviour, a test was conducted at a later date with the data acquisition equipment contained on a pannier rack behind the rider and a 'dummy' backpack on the rider's back. The cyclist then rode a number of laps around an empty velodrome both with and without the backpack and no difference was observed in any of the recorded data.

Collating the data obtained over the length of the simulated race, a discrete Probability Density Function (PDF) was produced by binning the data into 1° increments and calculating the probability of each bin value occurring over the length of the data. This details the probability of a certain yaw or pitch angle occurring during riding and is shown in Figure 3.10, split into the four team pursuit positions. The results of the PDF demonstrate an approximate

normal distribution of airflow angles experienced during track cycling. When a cyclist is in position 1, the airflow is relatively constant in direction with a small range of yaw and minimal range of pitch angles, exemplified by a very narrow distribution. However when the cyclist is in positions 2 to 4, the range of yaw and pitch angles increases and the distribution flattens. The obtained PDFs can be used for drag reduction testing in a similar manner to Wind Averaged Drag [78, 141] where the measured drag at a certain yaw angle is weighted according to the probability of that yaw angle occurring. This provides a simple comparison between otherwise difficult to distinguish drag results.

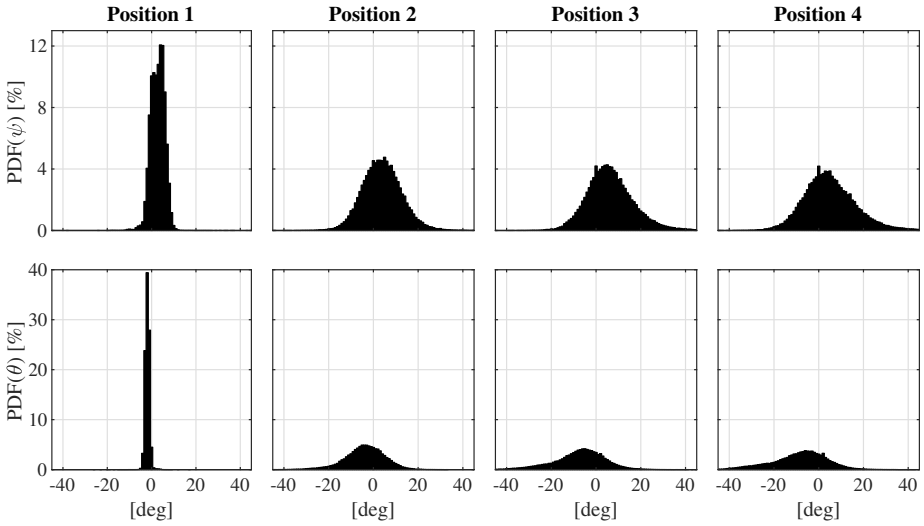


Figure 3.10 Probability Density Function of the yaw and pitch angles.

3.4 Conclusion

In this experimental investigation, the air velocity at a single point anterior to a cyclist was recorded for the length of a simulated team pursuit race. The results indicated a significant dependence of the airflow on three primary factors; the cyclist's position in the team pursuit line, their location around the track, and their cadence cycle. When the cyclist is at the front of the team pursuit line, the airflow magnitude is 92 % of the wheel speed with a turbulence intensity of 1.5 %, however when the cyclist moves position and into the wake of three other riders, the velocity ratio drops to 46 % and the turbulence intensity increases significantly to 18.5 % for the final position along the team pursuit line. This drop in velocity ratio provides a significant

lowering of the dynamic pressure, and hence the drag, experienced by the cyclists along the team pursuit line and follows a similar pattern to previously reported team pursuit line drag ratios.

In addition, it is clear that the effects of cornering have a major influence on the airflow incident on a cyclist. The experimental results display a yaw angle ranging from $-2°$ to $8°$ and a pitch angle range of $-1°$ to $-3°$, which are much greater than the theoretically calculated maximum yaw and pitch values of $1.7°$ and $-1.6°$ respectively. It is also clear that the pedalling motion induces a yaw angle fluctuation on the rider and is this likely due to rocking and weaving of the bicycle. The experiments conducted in this investigation develop our understanding of the flow field experienced during track cycling and a team pursuit event in particular. This can be used in the advancement of wind tunnel or CFD testing through replication of turbulence and flow angles, providing a more realistic environment for experimentation.

— Chapter 4 —

The theoretical impact of a velodrome transition curve

A key feature of this research is understanding the environment experienced by a track cyclist at different locations around a typical lap. This is shown in Chapter 3 where the flow angles are calculated based on lap position, roll angle, and wheel speed. It is also common in the academic literature to calculate roll angles for use in various mathematical models. To complete these calculations accurately requires a model of the track geometry, including the transition curves into and out of the bends.

To date, there has been a lack of track cycling models that include the transition curves and how they can influence the bicycle dynamics around a typical lap. This chapter outlines the creation of a theoretical velodrome geometry model that includes transition curves and which can be adapted to any built velodrome from two simple geometric measurements. The influences of different transition curve profiles are outlined and compared to the typical track model with no transition curves.

Supplementing the work outlined in this chapter, Appendix A outlines the derivation of an additional turn curvature function for use in the velodrome model. The curvature of this function follows a polynomial profile and can provide any desired level of geometric continuity, but is limited by the maximum available transition curve length.

This chapter has been published in *Sports Engineering* and has been reformatted for this thesis. The as-published article is available at:

Fitzgerald, S., Kelso, R., Grimshaw, P., and Warr, A. (2021) 'Impact of transition design on the accuracy of velodrome models' *Sports Engineering*, 24, 23, DOI: 10.1007/s12283-021-00360-3.

Statement of Authorship

Title of Paper	Impact of transition design on the accuracy of velodrome models
Publication Status	☑ Published ☐ Accepted for Publication ☐ Submitted for Publication ☐ Unpublished and Unsubmitted work written in manuscript style
Publication Details	Fitzgerald, S., Kelso, R., Grimshaw, P., Warr, A. (2021). 'Impact of transition design on the accuracy of velodrome models' *Sports Engineering* 24, 23, DOI: 10.1007/s12283-021-00360-3.

Principal Author

Name of Principal Author (Candidate)	Shaun Fitzgerald		
Contribution to the Paper	Conceptualised and developed the mathematical model of velodrome geometry. Reviewed the literature of track cycling modelling, implemented existing bicycle power, roll and speed calculations, developed roll-rate and acceleration equations. Produced and analysed all data. Prepared the manuscript and generated all figures. Acted as corresponding author.		
Overall percentage (%)	85		
Certification:	This paper reports on original research I conducted during the period of my Higher Degree by Research candidature and is not subject to any obligations or contractual agreements with a third party that would constrain its inclusion in this thesis. I am the primary author of this paper.		
Signature		Date	12/11/2021

Co-Author Contributions

By signing the Statement of Authorship, each author certifies that:

i. the candidate's stated contribution to the publication is accurate (as detailed above);

ii. permission is granted for the candidate in include the publication in the thesis; and

iii. the sum of all co-author contributions is equal to 100% less the candidate's stated contribution.

Name of Co-Author	Richard Kelso		
Contribution to the Paper	Guided research direction, supervised work development and interpretation, helped generate ideas and concepts, and edited the manuscript.		
Signature		Date	15/11/2021

Name of Co-Author	Paul Grimshaw		
Contribution to the Paper	Guided research direction, supervised work development and interpretation, helped generate ideas and concepts, and edited the manuscript.		
Signature		Date	15/11/2021

Name of Co-Author	Andy Warr		
Contribution to the Paper	Guided research direction, supervised work development and interpretation, helped generate ideas and concepts, and edited the manuscript.		
Signature		Date	16/11/2021

Impact of transition curve design on the accuracy of velodrome models

S. Fitzgerald, R. Kelso, P. Grimshaw, A. Warr

Abstract

This work outlines the creation of a model of a velodrome datum line constructed from two straights, two circular arc bends, and four transition curves. Different transition curve options are outlined and contrasted with a model with no transition curves. The influence of velodrome geometry on the wheel speed, wheel acceleration, roll angle, roll rate, and power demand of a theoretical cyclist is presented. The results display similar wheel speeds and roll angles for different transition curves, with larger differences when compared with the no-transition-curve option. Greater differences are observed in the acceleration and roll rate, for which calculations are only possible when using a transition curve. Comparisons of the model with theodolite measurements of two velodromes show a mean minimum root mean square error of 0.0398 m. This work can be used to increase the accuracy of existing track cycling analytic models.

4.1 Introduction

The introduction of inexpensive, reliable, and accurate power meters has led to improvements in detailed mathematical models of track cycling. With recordings of the cyclist's power and wheel speed and an accurate bicycle dynamics model, the aerodynamic drag can be calculated [11] or lap times can be predicted [10]. Two unique features of track cycling are the high speeds and low turn radius. These lead to high roll angles (ϕ) in the bends, often exceeding 50° [12]. A high roll angle leads to a discrepancy between the wheel speed (V_W) and the velocity of the bicycle/rider centre of gravity (V_{CG}).

An accurate value for V_{CG} is required for mathematical modelling of a cyclist's power demand, and the roll angle can influence the incident airflow around a bend [142]. Calculation of ϕ and V_{CG} requires knowledge of V_W and the turn curvature (κ). Whilst V_W can be measured accurately using a conventional bicycle speed sensor, an exact κ can be more difficult to determine. Current track cycling mathematical models are generally based on an individual pursuit race, where the cyclist is assumed to follow the datum (black) line (see Figure 4.1) around the velodrome track [12]. Based on this

assumption, the turn curvature can be derived from the geometry of the track datum line, but the accuracy of the datum line model can vary, leading to inaccurate values of V_{CG} or ϕ.

The official requirements of the Union Cycliste Internationale (UCI) for an Olympic-grade velodrome specify a datum line lap length of 250 m, turn radius of 19–25 m, and a constant width of 7–8 m. The track must be a loop consisting of two curves connected by two parallel straight lines with gradual transitions between the curves and straights [4]. Non-Olympic grade velodromes can vary in lap lengths and turn radii, as specified in the UCI regulations. Many of the design considerations for an Olympic-grade velodrome are up to the track designer, allowing various track profiles.

The design of velodromes is commercially sensitive information, and the exact track shape is rarely released publicly. This leads to different research groups creating models of the track geometry based on various assumptions. Early work by Martin et al. [7] assumed the velodrome was a circle with constant turn radius and banking. Other authors have assumed the track to be two straights with two semi-circular [6, 8, 10, 11], or two semi-elliptical bends [44]. Lukes et al. [9] expanded on this model by creating a track with two straights and two circular-arc bends with four transition segments of linearly increasing turn radius between the bends and straights. The most detailed model to date is described in a preprint by Bos et al. [45], who defined a velodrome with two straights, two circular-arc bends and four transition segments with linearly increasing curvature. Fitton and Symons [12] surveyed one track with a theodolite and used unspecified information from the track designers to model a second track.

The construction of accurate velodrome geometry is required for periods where the cyclist will follow the datum line as well as for times when they will deliberately deviate from it. For example, team pursuit riders will move from the front to the rear of the team line by deviating wide up the banking, often when in the bends. In events such as the qualification time trial, cyclists will ride near the top of the track before descending to sprint around the final 200 m of the lap. As shown by Benham et al. [44], this descent is of critical importance and the shape of the velodrome bend can influence trajectory choices. Riders will take advantage of the bend and banking to convert potential energy into kinetic energy in the most efficient manner possible.

In this work, the effects of different velodrome designs on mathematical models of track cycling are investigated, with an emphasis on transition curve types. A velodrome datum line is constructed as a level, doubly symmetric piecewise function consisting of straights, circular-arc bends and transition curves. The model, shown in Figure 4.1, can be adapted to any real velodrome

using only two measured dimensions.

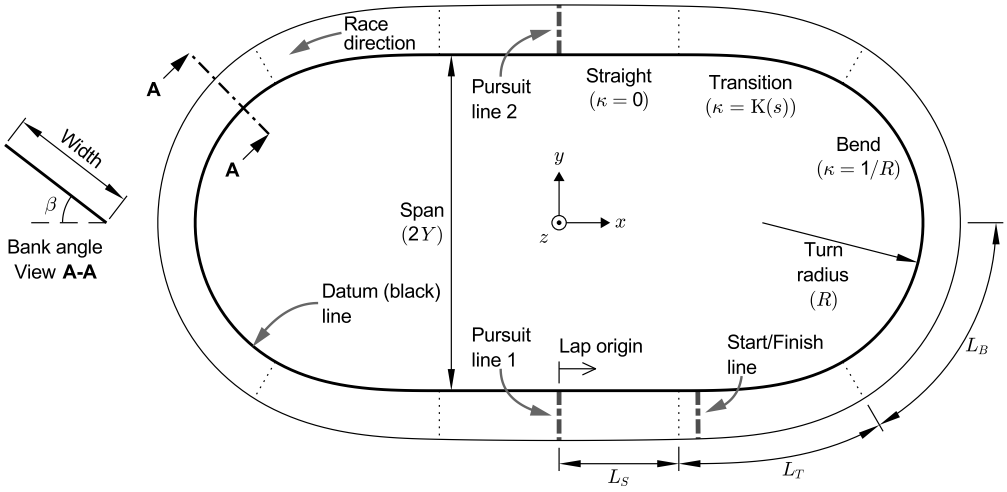


Figure 4.1 Plan view of a velodrome with required definitions.

When constructing track models for the analysis of bicycle motion, an important property to consider is the geometric continuity between the straights, transition curves and bends. This is a measure of how smooth the complete curve is, with defined levels of smoothness denoted by G^k, indicating that the first k derivative vectors are continuous in direction, but not necessarily in magnitude [143]. This necessitates that for a G^1 curve the piecewise connections join at the same position and tangent angle, a G^2 curve also has the same curvature at all connections, and a G^3 curve also has a continuous derivative of curvature. Higher levels of geometric continuity allow further derivatives of motion to be found, i.e., to calculate acceleration, a minimum of G^2 is required, and to calculate jerk, G^3 is required. For modelling of cycling, a G^2 model will prevent sudden jumps in V_{CG} and ϕ calculations, and G^3 allows calculation of a continuous acceleration or roll rate.

The standard method for constructing transition curves is to use a 1^{st} order clothoid where the curvature increases linearly with the arc length. First order clothoids have been used to design transitions for roads, railways, and amusement park rides [144, 145]. The case for connecting a straight line to a circular arc has been solved by Meek and Walton [146], but this, and the velodrome model developed by Bos et al. [45], use the standard clothoid. The generalised method developed here has two options, one for a G^2 continuous n^{th} order clothoid where the curvature is proportional to the arc length raised to the power of n, and a second G^3 option that has a sinusoidal increase in curvature along the arc length. This model uses the lap length, track span and mid-bend turn radius as inputs, contrasting with the model by Bos et al. [45],

which uses the straight, bend and transition lengths as inputs.

4.2 Methods

4.2.1 Transition curve properties

This section outlines the creation of a transition curve (x_T, y_T) connecting a straight line to a circular arc.The two parameters defining the curve are the circular arc radius (R) and the vertical distance from the straight line to the arc centre (Y), as defined in Figure 4.2. The tangential angle (ψ) is the angle between the tangent to the curve and the x-axis, and (x_{Bc}, y_{Bc}) is the bend centre.

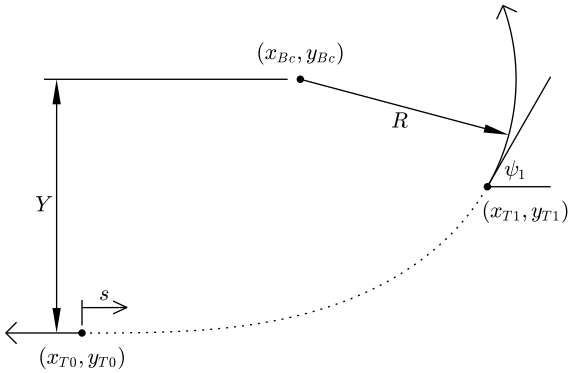


Figure 4.2 Transition curve definitions for connecting a straight line to a circular arc with defining parameters Y and R.

As detailed by Nutbourne et al. [147], with an initial angle of $\psi = 0$ and an origin at (x_{T0}, y_{T0}), the parametric equation of a curve can be defined by its curvature function (K) with

$$\begin{pmatrix} x_T(\tau) \\ y_T(\tau) \end{pmatrix} = \begin{pmatrix} a \int_0^\tau \cos\left(\int_0^u K(v)\,\mathrm{d}v \right) \mathrm{d}u \\ a \int_0^\tau \sin\left(\int_0^u K(v)\,\mathrm{d}v \right) \mathrm{d}u \end{pmatrix}. \tag{4.1}$$

Here, a is a scaling factor to be determined, τ is the equation parameter ranging from 0 to τ_1, and K is a chosen function of curvature. The primary properties of the curve can be found from the partial and complete first and second derivatives of Equation (4.1). The arc length $(\mathrm{d}s)$, tangential angle (ψ), curvature (κ), and the rate of change of the curvature with respect to arc length (κ') are

$$\mathrm{d}s = a\,\mathrm{d}\tau, \tag{4.2}$$

$$\psi(\tau) = \int_0^{\tau} K(v)\,\mathrm{d}v, \tag{4.3}$$

$$\kappa(\tau) = \frac{K(\tau)}{a}, \tag{4.4}$$

$$\kappa(\tau) = \frac{K'(\tau)}{a^2}, \tag{4.5}$$

respectively. The centre of the circle of curvature is then:

$$\begin{pmatrix} x_{Tc}(\tau) \\ y_{Tc}(\tau) \end{pmatrix} = \begin{pmatrix} x_T(\tau) - \dfrac{1}{\kappa(\tau)}\sin(\psi(\tau)) \\ y_T(\tau) + \dfrac{1}{\kappa(\tau)}\cos(\psi(\tau)) \end{pmatrix}. \tag{4.6}$$

4.2.2 Connecting a straight line to a circular arc

With these definitions and an appropriate curvature function, it is possible to match the transition curve end points, tangent angles, and curvatures to the circular bend with G^2 (or greater) continuity. Matching to the straights is achieved when $\tau = 0$, at which point at least the first two derivatives are equal in direction. To connect with the circular arc at $\tau = \tau_1$, the curvatures are equated with

$$\frac{1}{R} = \frac{K(\tau_1)}{a}, \tag{4.7}$$

which gives

$$a = RK(\tau_1). \tag{4.8}$$

To match the tangent angles, the centre of the circular arc must be coincident with the centre of curvature at the transition end point. Substituting Equations (4.1), (4.3), (4.4) and (4.8) into Equation (4.6) gives

$$\begin{pmatrix} x_{Bc} \\ y_{Bc} \end{pmatrix} = \begin{pmatrix} RK(\tau_1)\displaystyle\int_0^{\tau_1} \cos\left(\int_0^u K(v)\,\mathrm{d}v\right)\mathrm{d}u - R\sin\left(\int_0^{\tau_1} K(v)\,\mathrm{d}v\right) \\ RK(\tau_1)\displaystyle\int_0^{\tau_1} \sin\left(\int_0^u K(v)\,\mathrm{d}v\right)\mathrm{d}u + R\cos\left(\int_0^{\tau_1} K(v)\,\mathrm{d}v\right) \end{pmatrix}. \tag{4.9}$$

It can be observed that this is a monotonically increasing function for $\tau > 0$ and so τ_1 can be numerically solved for by setting $y_{BC} = Y$. Solving for τ_1 is done with the Newton-Raphson method and expanding Equation (4.9) as a first-degree Taylor polynomial for the iteration start point. Once τ_1 has been obtained, the transition length (L_T) can be found with

$$L_T = \tau_1 RK(\tau_1) \tag{4.10}$$

4.2.3 Fitting to a velodrome track

With the transition curve now fully defined, the remaining track parameters can be determined. The lengths of the circular bend (L_B) and straight (L_S) are found with

$$L_B = \left(\frac{\pi}{2} - \psi_1\right)R, \tag{4.11}$$

$$L_S = \frac{L_L}{4} - L_T - L_B. \tag{4.12}$$

respectively, where L_L is the lap length. Setting the origin to the centre of the velodrome, the coordinates of the straight are

$$\begin{pmatrix} x_S(\tau) \\ y_S(\tau) \end{pmatrix} = \begin{pmatrix} \tau \\ -Y \end{pmatrix}, \quad 0 \le \tau \le L_S, \tag{4.13}$$

and the coordinates of the circular bend are

$$\begin{pmatrix} x_B(\tau) \\ y_B(\tau) \end{pmatrix} = \begin{pmatrix} L_S + x_{Bc} + R\cos(\tau) \\ R\sin(\tau) \end{pmatrix}, \quad \psi_1 - \frac{\pi}{2} \le \tau \le 0. \tag{4.14}$$

The coordinates of the transition curve are linearly translated by $(L_S, -Y)$ so that Equations (4.1), (4.13) and (4.14) create a continuous curve along one quarter of the velodrome. This curve is mirrored twice about the long and short axes to create a complete track, producing a curvilinear coordinate system of lap position with its origin at pursuit line 1 in the middle of a straight, as defined in Figure 4.1.

Both Y and R must be less than $L_L/(2\pi)$ which is the limiting case for a circular track, and there are three further limitations. Firstly, preventing an inflection in the transition curve requires $Y > R$ and $\tau_1 > 0$. Secondly, for a circular bend to exist, $\psi_1 < \pi/2$ giving

$$\int_0^{\tau_1} K(v)\,\mathrm{d}v < \frac{\pi}{2}. \tag{4.15}$$

Thirdly, $L_S > 0$ for a straight to exist, which leads to

$$\tau_1 K(\tau_1) - \int_0^{\tau} K(v)\,\mathrm{d}v < \frac{L_L - 2\pi R}{4R}. \tag{4.16}$$

4.2.4 Curvature profiles

Two curvature profiles, which have been designed without scaling so that $\tau_1 = L_T$ and $a = 1$ (following Equations (4.8) and (4.10)), are provided here. The first is a power function given by

$$K(\tau) = \frac{\tau^n}{RL_T^n}, \tag{4.17}$$

where n is a chosen exponent. Equation (4.17) provides G^2 continuity and when $n = 1$ it reduces to the standard clothoid transition curve with a linear increase in curvature along the transition. The second function is a half sine wave provided by

$$K(\tau) = \frac{1}{2R}\left(\sin\left(\frac{\pi}{L_T}\tau - \frac{\pi}{2}\right) + 1\right), \tag{4.18}$$

and is a G^3 curve with a continuous derivative of curvature. Equation (4.18) does not fit the measured track data quite as well as Equation (4.17), but it more closely represents the path taken by a cyclist on the track. It is possible to develop this further with a G^4 curve constructed from a quintic polynomial curvature function (or even higher continuity), but this provides diminishing returns and higher orders of continuity beyond G^3 are not generally required.

The ranges of inputs Y and R (normalised by L_L) are provided by the shaded areas in Figure 4.3 for four curvature profiles. For smaller values of Y and R, the track has longer straights and sharper corners (long and narrow), whilst for larger values the track is more circular (short and wide). As Y/R approaches 1, the transition length approaches 0 m, whilst at the point where Equations (4.15) and (4.16) are equal, the track is entirely composed of transition curves.

4.2.5 Banking

Observations of measured velodromes show that the banking around each bend is composed of four different sections, namely the entry-bottom, entry-top, exit-top, and exit-bottom. The complete velodrome is rotationally symmetric about its centre point such that the two bends are identical. Each section is unique to each velodrome [137] and would require specific modelling to fit measured data and join with acceptable continuity. As such we have not created an accurate analytic banking model as the number of controlling degrees of freedom would be prohibitive and unlikely to be easily generalised. However, as a first approximation, an equation for a symmetrical bank angle versus lap position (s) from the minimum ($\beta_{\min}$) and maximum ($\beta_{\max}$) bank angles is

$$\beta(s) = \frac{\beta_{\max} - \beta_{\min}}{2}\sin\left(\frac{4\pi}{L_L}s - \frac{\pi}{2}\right) + \frac{\beta_{\max} + \beta_{\min}}{2}. \tag{4.19}$$

Equation (4.19) is useful if only basic banking data is available: the recommended method for determining the bank shape is to survey the track with an inclinometer or a theodolite and then use a fitting function to smooth

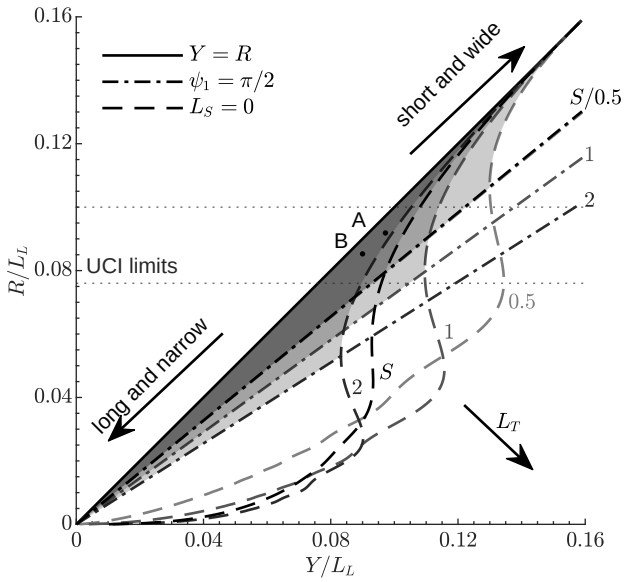


Figure 4.3 Parameter space of the model where the shaded area indicates the limits of normalised inputs Y and R with four different curvature profiles: Equation (4.17) with $n = 0.5$, 1, 2, and Equation (4.18) (S). The dashed-dotted lines indicate limits due to Equation (4.15), whilst the dashed lines indicate limits due to Equation (4.16). The UCI limits for 250 m velodrome design are indicated by the dotted lines. Points A and B represent the values for the two measured velodromes.

the measured results and fit them to the datum line data. As the track width is a constant and easily measured value, a complete three-dimensional model of the track surface can then be constructed.

4.2.6 Bicycle dynamics

To determine the influence of transition design, the roll angle, roll rate, wheel speed, wheel acceleration, and power output of a theoretical cyclist are calculated. This model assumes the cyclist is a point mass at a distance h_{CG} from the velodrome surface and that the roll acceleration is negligible. Figure 4.4 outlines the forces acting on a cyclist in a plane perpendicular to their direction of motion. Here F_C is the centrifugal force, F_W is the weight force, F_N is the normal force and F_f is the lateral frictional force.

The equation for calculating roll angle on a level turn has been independently derived in a variety of forms in several studies [10–12, 142] and in one form is

$$\tan\phi = \frac{\kappa V_W^2}{g}\left(1 - h_{CG}\kappa\sin\phi\right), \tag{4.20}$$

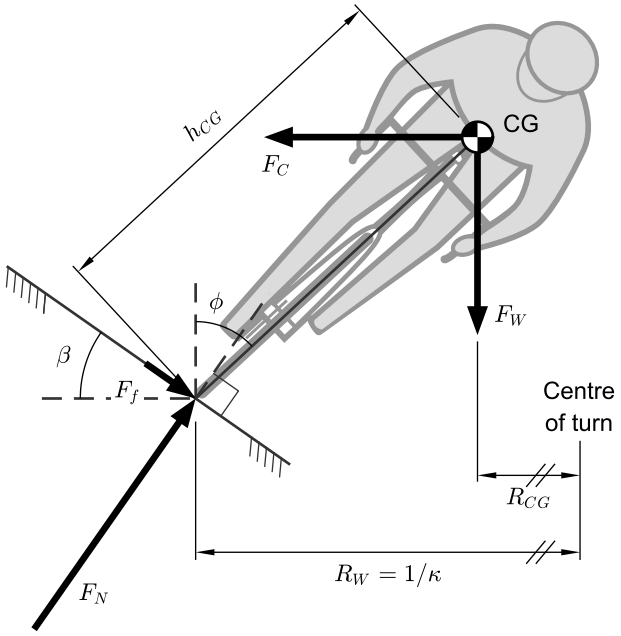


Figure 4.4 Free-body diagram of a bicycle on a level banked corner.

where h_{CG} is the height of the centre of gravity of the bicycle/rider and g is the gravitational acceleration. The velocity of the centre of gravity can then be calculated:

$$V_{CG} = V_W \left(1 - h_{CG}\kappa \sin\phi\right). \tag{4.21}$$

Equations (4.20) and (4.21) have been slightly modified from the reference material so that the turn curvature is used rather than the turn radius. This modification was done to simplify calculations as the curvature tends to zero in the straights whilst the turn radius tends to infinity. The roll rate ($\dot{\phi}$) can be found by differentiating Equation (4.20) with respect to time with

$$\dot{\phi} = g V_W \left(\frac{\left(\kappa' V_W^2 + 2\kappa a_W\right)\left(1 - h_{CG}\kappa \sin\phi\right) - h_{CG}\kappa\kappa' V_W^2 \sin\phi}{g^2 + \kappa^2 V_W^2 \left(V_W^2 \left(1 - h_{CG}\kappa \sin\phi\right)^2 + g h_{CG} \cos\phi\right)} \right), \tag{4.22}$$

where a_W is the acceleration of the wheels. The acceleration of the centre of gravity (a_{CG}) can then be determined by differentiating Equation (4.21) with respect to time:

$$a_{CG} = a_W \left(1 - h_{CG}\kappa \sin\phi\right) - h_{CG} V_W \left(\kappa' V_W \sin\phi + \kappa\dot{\phi} \cos\phi\right). \tag{4.23}$$

The quasi-steady-state approximation used to derive these equations assumes that the roll acceleration is approximately zero at each time step. Therefore,

Equations (4.22) and (4.23) are linear numerical derivatives of the quasi-steady-state roll and velocity, similar to previous models [12], rather than a complete unsteady analysis. The required power demand (P) can be modelled by [9, 13]:

$$P = \frac{1}{\eta}\left(\underbrace{\frac{1}{2}\rho C_D A V_A^2 V_{CG}}_{\text{Aerodynamic drag}} + \underbrace{mg\frac{\cos(\phi-\beta)}{\cos\phi}C_{RR}(1+|\phi-\beta|\mu_s)V_W}_{\text{Rolling resistance}}\right). \tag{4.24}$$

The rolling resistance has the term $\cos(\phi-\beta)/\cos\phi$ to account for the increased normal force due to the centrifugal force and bank angle. The use of a scrubbing resistance value (μ_s) is based on the work of Lukes et al. [9], and the velocity of air (V_A) was assumed to be equal and opposite to the velocity of the centre of gravity. Equation (4.24) is a simplified power model that does not account for bearing resistance, steering angles, or changes in potential and kinetic energy, but it encompasses the predominant resistive forces for steady riding. Input values and definitions for Equations (4.20) to (4.24) are shown in Table 4.1.

Table 4.1 Cyclist model input variables.

Variable	Notation	Value
Aerodynamic drag area	$C_D A$	$0.2\,\mathrm{m}^2$
Coefficient of rolling resistance	C_{RR}	0.002
Coefficient of scrubbing resistance	μ_s	$0.4125\,\mathrm{rad}^{-1}$
Drivetrain efficiency	η	0.98
Air density	ρ	$1.2\,\mathrm{kg/m}^3$
Height of the centre of mass	h_{CG}	1 m
Total mass	m	75 kg
Gravitational acceleration	g	$9.81\,\mathrm{m/s}^2$
Minimum bank angle	$\beta_{\min}$	13°
Maximum bank angle	$\beta_{\max}$	43°

4.3 Results

The model was implemented in Matlab r2019b (MathWorks, USA) and compared with theodolite surveys of two Olympic-grade velodromes, designed by different architects. These two velodromes were surveyed by the Australian Institute of Sport, who provided the authors with 100 three-dimensional data points approximately every 2.5 m along the datum line.

Typical theodolite accuracy has been shown to be in the order of 1:4000 for distances of 100 m, with increasing error with distance [148]. This gives an estimated theodolite accuracy of ±0.0125 m. The measurements showed that both velodromes were almost level, with a maximum elevation change of 10 mm between the centres of the straight and bend. Both velodromes have L_L = 250 m, Y was measured with the theodolite data, and the values of R and n were calculated using orthogonal regression [149]. A measure of the goodness of fit of the model was calculated by the Root Mean Square error (RMS), based on the shortest orthogonal distance from each measured point to the model. The model takes <0.4 s to compute on a desktop computer (Intel i7-6700 at 3.40 GHz).

The results for the two velodromes are displayed in Table 4.2 and Figure 4.5. Equations (4.17) and (4.18) both show a good agreement with a mean minimum RMS of 0.0398 m. For comparison, simpler G^1 models constructed from two straights and two 180° semi-circles were also fitted. These simpler models have $Y = R$, with no transition curves and are identical to those used elsewhere [6, 8, 10, 11].

Table 4.2 Numerical results from fitting different models to the measured velodrome data.

Velo-drome	Transition profile	Cont-inuity	L_L [m]	Y [m]	R [m]	n	RMS [m]	L_T [m]	L_T [% L_L]
A	Power (Eq. 4.17)	G^2	250	24.3	22.965	0.5	0.0308	26.6	42
	Power (Eq. 4.17)	G^2			23.195	1.0	0.0582	24.9	40
	Sinusoidal (Eq. 4.18)	G^3			23.189	-	0.0618	33.2	53
	No transitions	G^1			-	-	0.3230	0	0
B	Power (Eq. 4.17)	G^2	250	22.5	21.317	0.5	0.0488	24.1	39
	Power (Eq. 4.17)	G^2			21.509	1.0	0.0602	22.7	36
	Sinusoidal (Eq. 4.18)	G^3			21.501	-	0.0613	30.3	48
	No transitions	G^1			-	-	0.2807	0	0

Varying the transition curve function (K) has only a minor influence on the exact 2D coordinates of the transition curve, but it can produce a larger change in the curvature and rate of change of curvature with all other factors held constant (Figure 4.6). When using Equation (4.17) with $n = 1$, the curvature is a linear function with a constant rate of change of curvature. For $n > 1$, there is a smoother increase in the curvature and for $n < 1$ there is an infinite derivative of curvature at the start of the transition, which then decreases towards the bends. For the sinusoidal profile (Equation (4.18)), there is an increasing rate of curvature until the middle of the transition when the rate

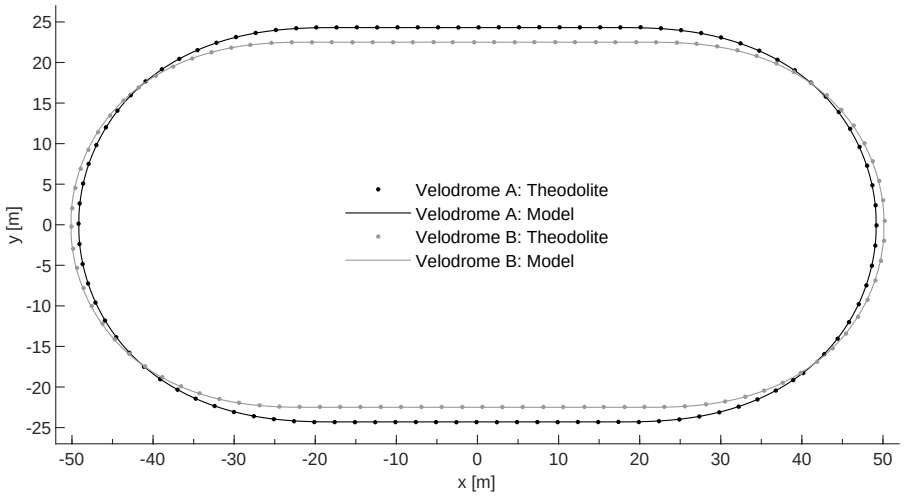


Figure 4.5 Comparing the model with two measured velodromes. Velodrome A: $Y = 24.3\,\text{m}$, $R = 22.965\,\text{m}$, $n = 0.5$. Velodrome B: $Y = 22.5\,\text{m}$, $R = 21.317\,\text{m}$, $n = 0.5$.

of change reverses.

The bank angle variation around a velodrome lap is shown in Figure 4.7 where the differences between the two tracks and the symmetric model are clearly evident. Figure 4.7 demonstrates how the symmetrical model is only an approximation of a real velodrome, and that detailed measurements are required for an accurate model. A feature of note is the higher bank angles on the bend exit compared with the bend entry, which can help to increase the cyclist's speed when exiting the corner. In addition, it can be seen that the banking for velodrome B increases to a sharp maximum in the middle of the bends, whilst the banking for velodrome A is near its maximum value for a greater distance through the bends, demonstrating the variety of possible banking profiles across different velodromes. Observed bank angle data from Benham et al. [44] follows a similar profile to that from Velodrome A.

Figure 4.8 shows the calculated results of the motion of a theoretical cyclist with a constant V_{CG} along three track geometries with different transition curves. These calculations model a cyclist following the datum line exactly. The assumption of a constant V_{CG} is valid for a pursuit event where the athletes typically ride smoothly at a consistent pace and where the majority of the rider/bicycle mass lies close to the centre of gravity. The three track models comprise of: a simple model of two straights and two 180° bends, Equation (4.17) with $n = 1$, and Equation (4.18). The simple model has $Y = R = 23\,\text{m}$, and the two transition models have $Y = 23\,\text{m}$ and $R = 22\,\text{m}$. All tracks are 250 m long and have a symmetrical bank angle. Results were produced

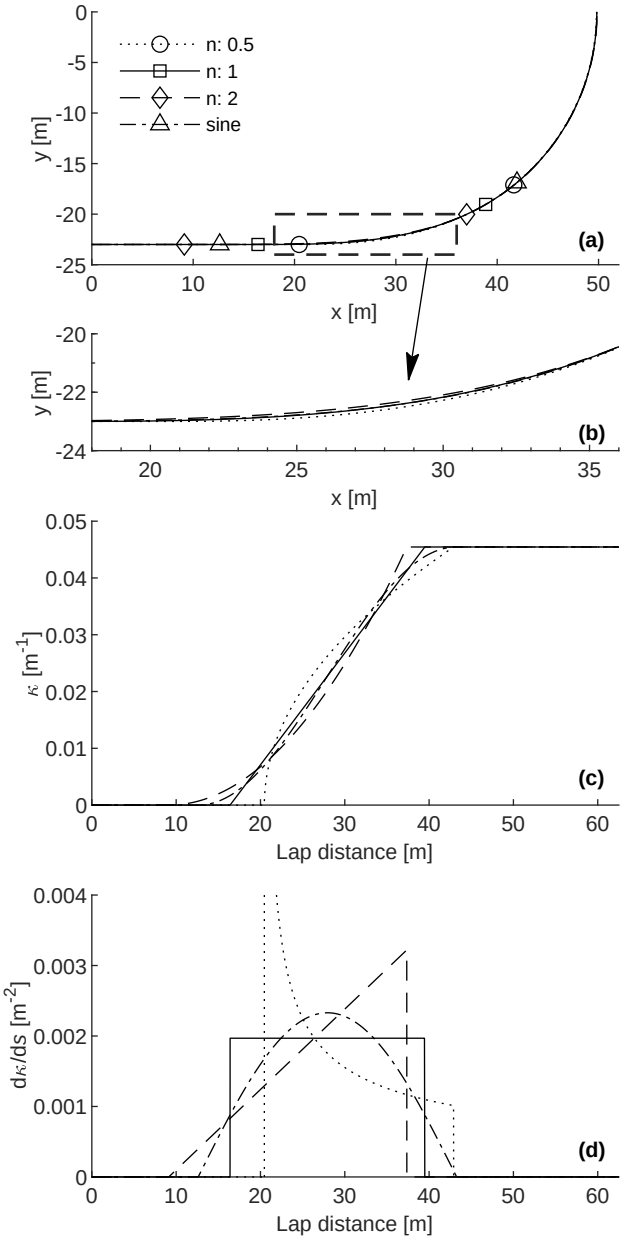


Figure 4.6 The effect of four different curvature profiles along one quarter of the track with $L_L = 250\,\text{m}$, $Y = 23\,\text{m}$, $R = 22\,\text{m}$, on the **(a)** (x,y) coordinates, **(b)** detailed coordinate view, **(c)** curvature, and **(d)** derivative of curvature. The end points of the transition curve are marked in sub-plot **(a)**.

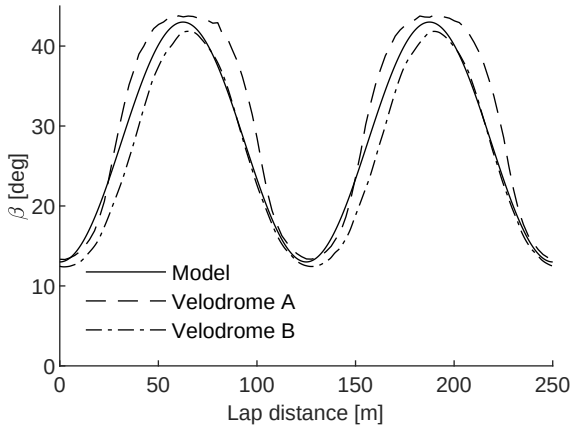


Figure 4.7 The bank angle of the two measured velodromes and a symmetric model with $\beta_{\min} = 13°$ and $\beta_{\max} = 43°$.

with Equations (4.20) to (4.24) with $V_{CG} = 16$ m/s, $a_{CG} = 0$ m/s, and the values from Table 4.1.

The effect of the continuous curvature can be seen in the wheel speed (Figure 4.8a) and the quasi-steady-state roll angle (Figure 4.8b), where there are continuous changes in the speed and roll throughout the lap for the two transition models. The different levels of geometric continuity can be observed in both the acceleration (Figure 4.8c) and roll rate (Figure 4.8d) plots. Here the simple model is G^1 continuous and so both a_W and $\dot{\phi}$ are impulse functions producing instantaneous changes in V_W and ϕ, respectively. The power model is G^2, so there are step changes in a_W and $\dot{\phi}$, while the sinusoidal model is G^3, which gives continuous changes in a_W and $\dot{\phi}$ throughout the lap. The increase in required power during the bends is predominately due to the increased normal force from the centrifugal force, hence increased rolling resistance, along with a smaller contribution due to the higher wheel speed. Finally, different velodrome models produce different lap times, which are displayed in the figure legend.

4.4 Discussion

Previous velodrome models with G^1 continuity had a step change in curvature which leads to a step change in the calculated V_{CG}, observable in the speed traces of previous studies [6, 10, 11]. By using a continuous curvature variation along a lap, the calculated V_{CG} is also a continuous function, leading to more

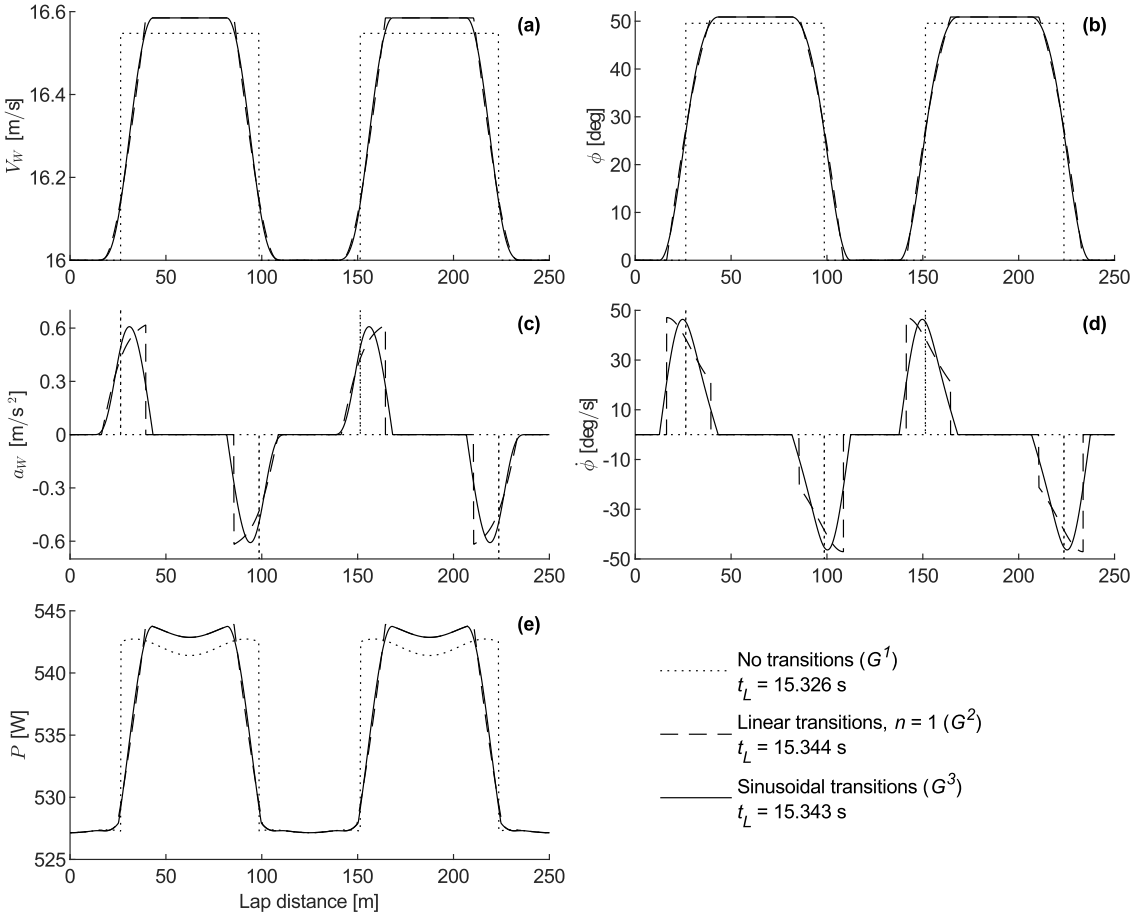


Figure 4.8 Three different transition curve options and the influence of a constant V_{CG} = 16 m/s on the **(a)** wheel speed, **(b)** roll angle, **(c)** wheel acceleration, **(d)** roll rate, and **(e)** power. Lap time is denoted by t_L in the figure legend.

accurate results. Using a G^2 or G^3 track model also provides the ability to calculate $\dot{\phi}$ and a_{CG}, which can increase the accuracy of bicycle dynamics models. In contrast, G^1 models have an impulse function for their acceleration and roll rate, with a sudden change four times a lap and zero elsewhere.

As shown in Table 4.2, in Figure 4.6, and illustrated by the relative size of the shaded areas in Figure 4.3, increasing levels of geometric continuity will increase the required transition curve length. The transition curve length can vary substantially across curvature profiles, from 36–40 % to 48–53 % of the total lap length for Equation (4.17) with $n = 1$ and Equation (4.18) respectively. Higher levels of geometric continuity will increase the transition length. Different curvature profiles can also influence results with differing

values for V_{CG} and ϕ. There can be a trade-off between good spatial fit (low continuity for matching a built velodrome) and a good physical fit (high continuity for matching a cyclist's path). If this model is used to calculate the motion of cyclists on a velodrome surface (such as [44]) then a spatial fit can be prioritised. However, if it is used to directly model the path of a cyclist (such as [6–12, 45]) then higher continuity is required. Care is required by the model user in determining the chosen curvature function.

A fundamental assumption used in Figure 4.8 and by others, is that the cyclist will follow the datum line exactly. The accuracy of this assumption generally degrades when riding faster where a cyclist will ride wide in the straights and close in the bends to produce a more circular trajectory. Doing so extends the transition between the bends and the straights, reducing the maximum roll rate and providing a more stable ride. However, this reduction in roll rate comes with an increase in the ridden distance, increasing the lap time. To replicate this altered trajectory, an artificial cyclist path could be constructed with an identical circular arc bend, a wider track span and a longer lap length. This can be achieved by keeping the sum of L_S and x_{Bc} constant and R constant while increasing Y and L_L.

The improved velodrome model developed in this work is dependent on a chosen curvature function and three measurable variables: L_L, R, and Y. The lap length L_L is always publicly provided for any track, the bend apex turn radius R can be determined with a tape measure and the method outlined in Section 4.6, and the track half-span Y can be found by measuring the lateral distance across the track between the two straights, then halving the result. As such, this model can be fitted to either a detailed theodolite survey of a track or simpler tape measure measurements. Using a theodolite survey provides the ability to measure the error between the model and measurements, but tape measure measurements are more practical to conduct. A Matlab function is provided in Section 4.6 for others to use this model in practice.

The primary limitation of this model is the assumption of a level velodrome with no change in height along the datum line. Measurements of two velodromes showed that there was only a slight change in elevation of the datum line, which was deemed small enough to assume a level plane; however, different velodromes may have a non-negligible change in elevation [12]. A further limitation of this model is the assumption of a single, common transition curve between the straights and the bends. Instead, the transition could be constructed from two or more connected curves or have different transitions in the bend exits to the entries. With detailed knowledge of a particular velodrome design, such a curve could be constructed by extending this model. However, this would add an extra degree of freedom, whereas

a primary feature of this model is its ease of use with only two required measurements and the lap length.

The work presented here has been conducted for track-cycling, but it is related to other oval racing events. Similar work has been completed for greyhound racing by [150], who developed different clothoid transition curves with particular consideration given to minimising the jerk for injury prevention. Greyhounds compete at similar speeds to track cycling, but their tracks have smaller turn curvatures ($0.016\,\mathrm{m}^{-1}$ to $0.02\,\mathrm{m}^{-1}$) and smaller bank angles (2.5° to 4.5°) [151]. These low bank angles create larger camber angles (the angle between the roll angle and the normal to the track surface) for greyhounds than for cyclists. Speed skating and outdoor running tracks are generally two straights and two 180° circular bends with no transition curves. Although it is permissible for a running track to have a double-curve bend, this uses two circular arcs joined to form a 180° bend rather than a true transition curve bend [152]. Motorsport tracks can be designed with clothoid transition bends; however, only a few existing oval tracks have two identical bends. Rather, motorsport tracks are generally tri-ovals or have further corners and so this model is only indirectly applicable.

4.5 Conclusion

This study details the effect of transition design on a cyclist's speed, acceleration, roll angle, roll rate, and power, and features a novel method of replicating velodrome datum line geometry. The developed model consists of straights, circular arc bends and transition curves with continuous curvature along the lap. The model requires just two measurements of the track dimensions, plus the track length, to specify the geometry. Comparison with detailed measurements of two constructed velodromes of 250 m lap length indicates a good fit with a mean minimum RMS error of 0.0398 m. Different transition curve options are compared, demonstrating similar wheel speed and roll angles for different transition curves, and greater differences in the acceleration and roll rate, for which calculations are only possible when using a transition curve. This method has the potential to improve the accuracy of existing track cycling analytic models and simplify the process of measuring and modelling the track geometry. A detailed survey of the bank angle around a lap can also be performed to include accurate bank angle measurements in the model.

4.6 Supplementary material

Presented here is a method of finding the radius of a circular arc from a chord length and an arc length. The arc length (L_a) is provided by the track as it is an official requirement to have markers every 5 m along a velodrome [4], and the chord length (L_c) between any two markers can be measured with a tape measure. From Figure 4.9, the half bend angle (δ) can be found with

$$\sin\delta = \frac{L_c}{L_a}\delta. \tag{4.25}$$

This is a transcendental equation without a simple solution, but it can be solved for δ in few iterations. The turn radius is then found with

$$R = \frac{L_a}{2\delta}. \tag{4.26}$$

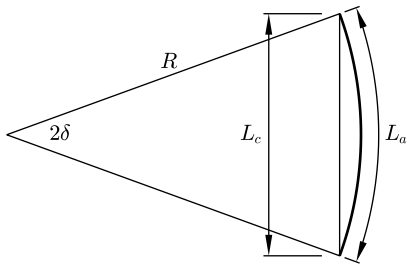


Figure 4.9 Measuring a circular radius from arc length and chord length.

Code availability

The Matlab function to create the velodrome geometry is supplied as supplementary data with the journal publication and is also available at: https://github.com/sjfitz/VelodromeModel.

Table 4.3 Chapter 4 nomenclature.

Notation	Description
$'$	(prime) Derivative with respect to lap distance
$\cdot$	(over-dot) Derivative with respect to time
Y	Track half width [m]
R	Track mid-bend radius [m]
κ	Curvature [m^{-1}]
ψ	Curve tangential angle [rad]
a	Scaling factor
τ	Curve parameter [m]
K	Transition curve curvature profile [m^{-1}]
(x_T, y_T)	Coordinates of the transition curve [m, m]
(x_B, y_B)	Coordinates of the bend [m, m]
(x_S, y_S)	Coordinates of the straight [m, m]
(x_{Tc}, y_{Tc})	Coordinates of the transition curve centre of curvature [m, m]
(x_{Bc}, y_{Bc})	Coordinates of the bend centre of curvature [m, m]
L_L	Length of the lap [m]
L_T	Length of the transition curve [m]
L_B	Length of the bend [m]
L_S	Length of the straight [m]
β	Track bank angle [rad]
V_W	Velocity of the wheels [m/s]
V_{CG}	Velocity of the centre of gravity [m/s]
V_A	Velocity of the air relative to the cyclist [m/s]
a_W	Acceleration of the wheels [m/s^2]
a_{CG}	Acceleration of the centre of gravity [m/s^2]
ϕ	Roll angle [rad]
$C_D A$	Aerodynamic drag area [m^2]
C_{RR}	Coefficient of rolling resistance
μ_s	Coefficient of scrubbing resistance [1/rad]
η	Drivetrain efficiency
ρ	Air density [kg/m^3]
h_{CG}	Height of the centre of gravity [m]
m	Combined cyclist/bicycle mass [kg]
g	Gravitational acceleration [m/s^2]

— Chapter 5 —

The dynamics and aerodynamics of a single rider

This chapter outlines experimental measurements of the aerodynamic environment experienced inside a velodrome. Here the work of Chapter 4 is used to facilitate theoretical calculations of roll and steering angles across a lap, and these are compared to experimental measurements at a variety of bicycle velocities. Measurements of the relative airflow are also taken and used to measure the incident turbulence levels for a solo rider and with other riders on the track.

Several mathematical models of track cycling will use similar calculations to those presented in this chapter, but there has been a paucity of work comparing the theoretical calculations to experimental work. This chapter aims to address this gap. Measurements of the steering angle input are undertaken to understand the flow around the front wheel so that the results from Chapters 3 and 6 can be understood in context.

Note that this chapter includes the methods section at the end of the chapter, rather than before the results as is standard for the other research chapters in this thesis. This was done to comply with publication guidelines for the journal to which this work has been submitted.

This chapter has been submitted for publication as an article in *Scientific Reports* and has been reformatted for this thesis. It has been submitted as:

Fitzgerald, S., Kelso, R., Grimshaw, P., and Warr, A. (2021) 'Measurements from an instrumented bicycle in a velodrome' Submitted to *Scientific Reports* (Nature Research).

Statement of Authorship

Title of Paper	Measurements of roll, steering, and the far-field wake in track cycling
Publication Status	☐ Published ☐ Accepted for Publication ☑ Submitted for Publication ☐ Unpublished and Unsubmitted work written in manuscript style
Publication Details	Fitzgerald, S., Kelso, R., Grimshaw, P., Warr, A. (2021). 'Measurements of roll, steering, and the far-field wake in track cycling', Submitted to *Scientific Reports.*

Principal Author

Name of Principal Author (Candidate)	Shaun Fitzgerald		
Contribution to the Paper	Developed the experimental equipment for the primary bicycle. Conducted the experimental testing and completed all data analysis. Reviewed the literature to collate and implement the bicycle motion calculations. Implemented turbulence and derived velocity ratio calculations. Prepared the manuscript and generated all figures. Acted as corresponding author.		
Overall percentage (%)	80		
Certification:	This paper reports on original research I conducted during the period of my Higher Degree by Research candidature and is not subject to any obligations or contractual agreements with a third party that would constrain its inclusion in this thesis. I am the primary author of this paper.		
Signature		Date	12/11/2021

Co-Author Contributions

By signing the Statement of Authorship, each author certifies that:

i. the candidate's stated contribution to the publication is accurate (as detailed above);

ii. permission is granted for the candidate in include the publication in the thesis; and

iii. the sum of all co-author contributions is equal to 100% less the candidate's stated contribution.

Name of Co-Author	Richard Kelso		
Contribution to the Paper	Guided research direction, supervised work development and interpretation, helped generate ideas and concepts, and edited the manuscript.		
Signature		Date	15/11/2021

Name of Co-Author	Paul Grimshaw		
Contribution to the Paper	Guided research direction, supervised work development and interpretation, helped generate ideas and concepts, and edited the manuscript.		
Signature		Date	15/11/21

Name of Co-Author	Andy Warr		
Contribution to the Paper	Guided research direction, supervised work development and interpretation, helped generate ideas and concepts, and edited the manuscript.		
Signature		Date	16/11/2021

Measurements of roll, steering and the far-field wake in track cycling

S. Fitzgerald, R. Kelso, P. Grimshaw, A. Warr

Abstract

A series of measurements taken with two instrumented track bicycles in a velodrome are presented. The bicycle wheel speed, cadence, roll angle, steering angle, power, and airspeed are recorded. Theoretical calculations of roll and steering angles are presented and show good agreement with experimentally-measured values. The accuracy of the roll angle calculations is dependent on the fidelity of the modelled cyclist path and decreases for higher riding speeds. Experimental measurements of the steering angle show a reasonable agreement to theoretical calculations with reduced steering angles on the bends at higher speeds. There is also seen an increasing steering angle oscillation within each pedal cycle with increasing bicycle velocity. Changes in steering angle can influence a cyclist's rolling resistance and the aerodynamic flow around the bicycle's front end. Observations are made of changes in the flow field ahead of the bicycle due to the presence of other riders on the track, showing an effective tailwind of up to 0.7 m/s, which can reduce a cyclist's aerodynamic drag. Data presented in this paper can help to provide a validation of values used in track cycling analytic models.

5.1 Introduction

Track cycling has been the subject of many mathematical models developed to predict performance or calculate a rider's aerodynamic drag [6, 8, 9, 11, 12]. These models usually measure the wheel speed and power output and then, depending on the model's complexity, calculate various other parameters to estimate either lap time or aerodynamic drag. A common feature of cycling mathematical models, primarily for track cycling, is the difference in velocity between the wheels (V_W) and the Centre of Gravity (CG) (V_{CG}). This difference in velocity arises from the cyclist rolling (leaning) in the bends, with roll angles often exceeding 50° for track cycling, and so the CG travels a shorter distance than the wheels, leading to a lower V_{CG}. As such, an accurate calculation of V_{CG} requires measurement of the wheel speed and bicycle roll angle (ϕ). Whilst the former can be measured with accuracy and ease, the latter can be more challenging to determine.

Studies comparing an experimentally-measured roll angle and a calculated roll angle have been completed by others but, to the best of the authors' knowledge, not in a velodrome. Sanjurjo et al. [153] combined the wheel speed and a 3-axis accelerometer with a custom dynamical model to measure the roll angle of a bicycle through standard riding manoeuvres. Sakai et al. [154] measured the roll angle for downhill cycling with an Inertial Measurement Unit (IMU) and compared it to a model of a point mass undergoing uniform circular motion. However, both of these studies were designed for general cycling, rather than track cycling where the roll angles are much greater, the track is banked, there is a non-zero roll rate during bend transitions (which account for approximately half of the total lap), and the bicycle often follows a standard, well-defined curve. Work has also been completed for motorcycle roll angles [155], however there can be large differences between the steering and roll angles for a motorcycle compared to a track cyclist due to the greater vehicle mass, wider tyres, and higher likelihood of the motorcycle rider displacing their centre of gravity away from the centreline of the motorcycle compared to a track cyclist.

There have been minimal efforts to measure the steering input for track cycling, which could differ from the requirements for road cycling. Restricting ourselves to pursuit events that largely follow the velodrome datum (black) line, a track cyclist will only provide minor adjustments to the steering angle as turning is generally achieved by rolling through the bends. A study by Kyle [37] measured the steering angle around a 250 m velodrome track, showing a mean of approximately 1° on the straights, 4° on the bends and ±2.5° with every pedal stroke. However, Kyle [37] only provides 8.5 s of data where the exact position of the velodrome bend/straights is unclear and the experimental method is not detailed. Typical track cycling models currently ignore steering angles [9–11], an exception being a forward-integration model by Fitton and Symons [12] which uses calculations involving the track bank angle and bicycle geometry to calculate a quasi-steady-state steering angle. The steering input over a lap is not presented by Fitton and Symons [12], with only the bend apex steering input provided over a range of speeds.

When cycling outdoors, an individual or group of cyclists create a low speed, turbulent wake behind themselves that dissipates naturally into the atmosphere [91, 156]. The longitudinal distance and lateral offset behind a cyclist at which the wake becomes negligible due to natural mixing, spreading, and dissipation is largely unknown. Research has been conducted at up to 6.9 m downstream of a single cyclist for the four cardinal crank angle positions, demonstrating a lateral shifting of the wake due to asymmetry of the cyclist [156]. Union Cycliste Internationale (UCI) road time trial regulations specify a

region 2 m wide and 25 m long that must be avoided to prevent drafting effects [157]. However, work by Blocken et al. [22] has shown that there can be a 7 % drag reduction when a cyclist is 50 m behind a motorcycle, demonstrating that the wake remains for a long distance. A cyclist would provide a smaller, but somewhat similar wake to a motorcycle. The presence of increased turbulence behind other riders in a velodrome has been previously measured in a team pursuit event, with a turbulence intensity of 16.1 % measured when drafting directly behind another cyclist compared to 1.5 % for a solo rider [142]. It has also been recently proposed that research should be conducted into the measurement and influence of turbulence on cycling aerodynamics [158].

When competing inside a velodrome, the average effective distance between two opposing pursuit teams/individuals is half the lap length, generally 125 m; much further than the previously-described longest measured drafting distance of 50 m. As there is no external wind and the cyclists travel around the same path, the wake may not have enough time to dissipate before the next riders arrive, and so there can be a build-up of slow-moving, turbulent airflow that is entrained by the movement of the cyclists. The size of this wake is likely to be dependent on the number of cyclists, their speed, position on the track, and the length of the race. The smallest wake would occur in a qualification time trial where there is only a single rider on the track for a maximum of three laps. In contrast, the largest wake would occur during a bunch race where there can be up to 24 riders for up to 200 laps of a 250 m track [4]. In this scenario, the wake of each individual cyclist would merge to create a swirling flow along the track, reducing the effective head-wind and hence aerodynamic drag. The cyclists on a velodrome are not usually packed as close as in a road peloton, but this swirling flow could be compared to the inside of a peloton where the aerodynamic drag of a sheltered cyclist has been shown to be 5–10 % of their isolated drag [32]. Work on speed skating has shown that skaters in an indoor skating oval can create a wind flow of 5–6 km/h along with increased mechanical turbulence [70]. This swirling tailwind flow has been mentioned before in the cycling literature [12, 38], but there has been no work completed in quantifying it as far as the authors are aware.

5.2 Results

Testing was completed with an instrumented bicycle that recorded the airflow anterior to the head tube, the wheel speed, (pedalling) cadence, power, crank angle and steering angle [159]. A second bicycle measured wheel speed, cadence, power, and roll angle. The bicycle-fixed coordinate system has the

x-axis directed to the bicycle's rear, the y-axis to the bicycle's right, and the z-axis upwards. This orientation has a positive roll angle (ϕ) when the cyclist is leaning left and a positive steering angle (δ) when the cyclist is steering left. The crank angle (ζ) is defined as zero with the cranks horizontal and the right crank forwards. A diagram of the coordinate orientations are shown in Figure 5.7b. For this work, the bicycle with the aerodynamic and steering sensors will be defined as the primary bicycle, and the bicycle with the roll sensor defined as the standard bicycle. Two elite cyclists rode the two separate bicycles for all tests and were paced by their coach to maintain a consistent, self-selected lap time. Full details of the setup are provided in Section 5.5.1.

5.2.1 Theoretical calculations

The measured results were compared to standard theoretical calculations of roll and steering used in previous track cycling models. To do so, a custom geometric model of the 250 m velodrome datum line was defined with reference to theodolite measurements of the physical line. This track model consists of two straight segments, two circular arcs in the middle of the bends, and four transition curves connecting the straights and the bends. The transition curves were designed with the curvature increasing from zero in the straights to $0.0465\,\mathrm{m}^{-1}$ in the circular bends by following a half sine wave trough-to-peak path [160]. All theoretical calculations assume that the cyclist follows the datum line exactly and all laps start at the pursuit line in the middle of the home straight and are left-turning.

By assuming the cyclist/bicycle system is a point mass and equating moments about the tyre/track contact point, the roll angle can be calculated from the wheel speed and track geometry with [10, 11, 160]:

$$\tan\phi = \frac{\kappa V_W^2}{g}\left(1 - h_{CG}\kappa\sin\phi\right), \tag{5.1}$$

Here κ is the turn curvature, defined as the inverse of the turn radius, h_{CG} is the height of the centre of gravity of the bicycle/rider, and g is the acceleration due to gravity. This is a transcendental equation that requires iteration to solve, but it converges on its true result in few iterations. Once the roll angle is found, V_{CG} can be calculated with:

$$V_{CG} = V_W\left(1 - h_{CG}\kappa\sin\phi\right). \tag{5.2}$$

Theoretical steering input calculations were undertaken following the method outlined by Fitton and Symons [12] with wheel cornering and camber stiffness coefficients obtained from Doria and Roa [161].

5.2.2 Changes over a lap

The roll angle results from the standard bicycle are shown in Figure 5.1 alongside calculated roll angles from Equation (5.1). There can be seen a continuous change in the measured roll angle from the straights to the bends along with some small variations in the middle of the bends. The calculated roll increases at a steep rate during the transition zone, following the increase in track curvature during the bend transition, then remains constant through the primary curve of the bend. The lap-averaged root mean square (RMS) error between the measured and calculated results is 2.1°. The most significant discrepancy between the calculated and measured results occurs at the start and end of the track transitions and is likely due to the uncertainty of the modelled cyclist's path. A cyclist will not follow the datum line exactly, rather they can ride outside the datum line, higher up the bank on the straights, and then close to the datum line in the bends, creating a discrepancy between the actual turn radius of the wheels and the expected turn radius based on the datum line. This is done so that the cyclist can better control their change in roll from the straights to the transitions and onto the bends, lessening the maximum roll rate by increasing roll early and decreasing roll later. This pattern could also be due to the rider maintaining a constant height across a lap as the datum line increases slightly in elevation in the bends. In addition to the influence of lap position, there is also a secondary variation in roll due to the roll of the bicycle within each pedal cycle [162].

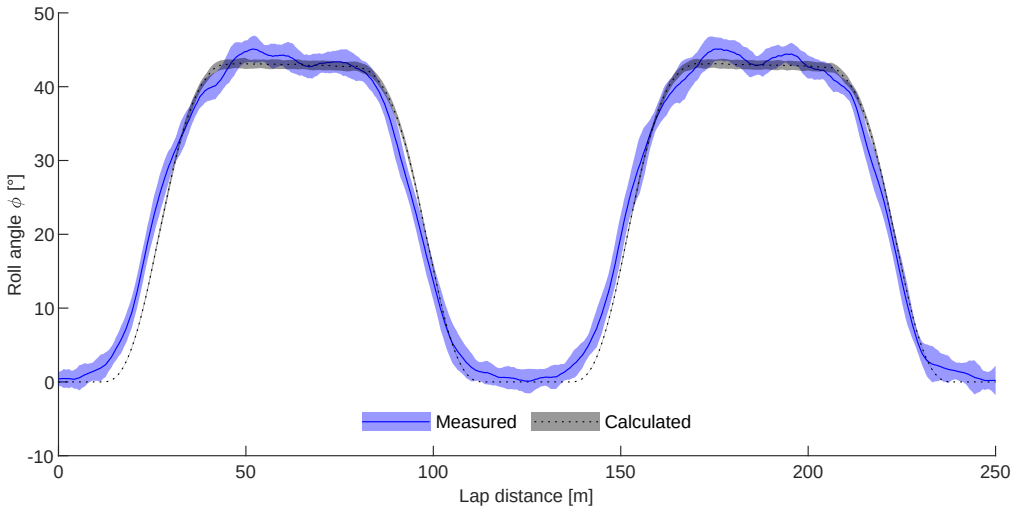


Figure 5.1 Measured and calculated roll angle averaged over 17 laps with a mean wheel speed of 14.0 m/s. The shaded area indicates ±1 standard deviation.

A test was conducted by riding the standard bicycle behind a derny (motorised pacing bicycle) for two laps at a constant speed and then accelerating to a higher speed for further laps. The use of a derny facilitated steady speed pacing and allowed higher velocities than was achievable by a solo rider. The results for the roll angle across various speeds are shown in Figure 5.2. At low speeds, the cyclist can follow the datum line closely and so the calculated curve closely matches the experimental results, whilst at higher speeds the rider was observed to travel wider on the straights and closer to the datum line in the middle of the bend. This is confirmed by tracking the wheel distance travelled over each lap, which increases from 252.0 m at 10 m/s to 253.8 m at 19 m/s, as well as the increasing lap-based RMS error between the measured and calculated roll angles, shown in brackets on the right of Figure 5.2. The combination of increasing wheel distance travelled, increasing RMS error, and increasing discrepancy between the measured and calculated values of roll angle around the change between the straights and transitions indicates a more circular trajectory at higher speeds.

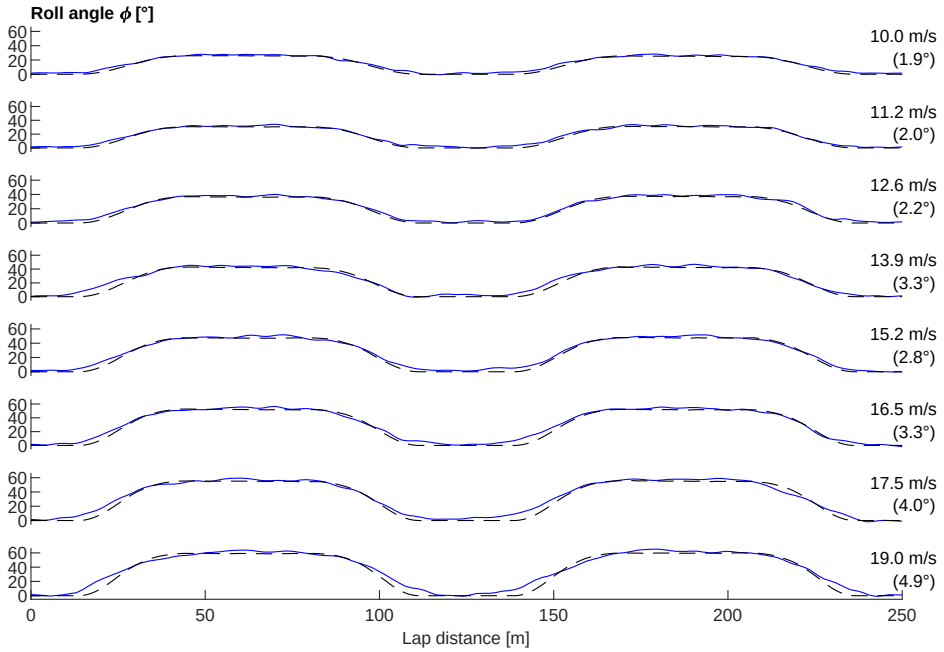


Figure 5.2 Measured (solid blue lines) and calculated (dashed black lines) roll angle for a range of wheel speeds. Shown on the right is the mean wheel speed and RMS error between the measured and calculated roll angles. Data is averaged over two laps for each speed.

The measured wheel speed (V_W), calculated centre of gravity speed (V_{CG}, Equation (5.2)), and measured airspeed (V_A), averaged over seven laps, are

shown in Figure 5.3. On a small scale there is a random fluctuation due to inter-lap variations, but on a larger scale some clear patterns emerge. There is a distinctive increase in V_W in the bends whilst V_{CG} remains relatively constant throughout each lap. This shows that the rider attempted to maintain a constant V_{CG} in order to maintain a constant lap time, and to accommodate this they increased their cadence in the bends and decreased it in the straights. The increasing cadence corresponds to a drop in their power output early in the bends that then steadily increases as they exit towards the straights. The velocity of the air is always less than V_{CG}, primarily due to the upstream effect of the cyclist and bicycle slowing down the air at the measurement probe tip [32, 142].

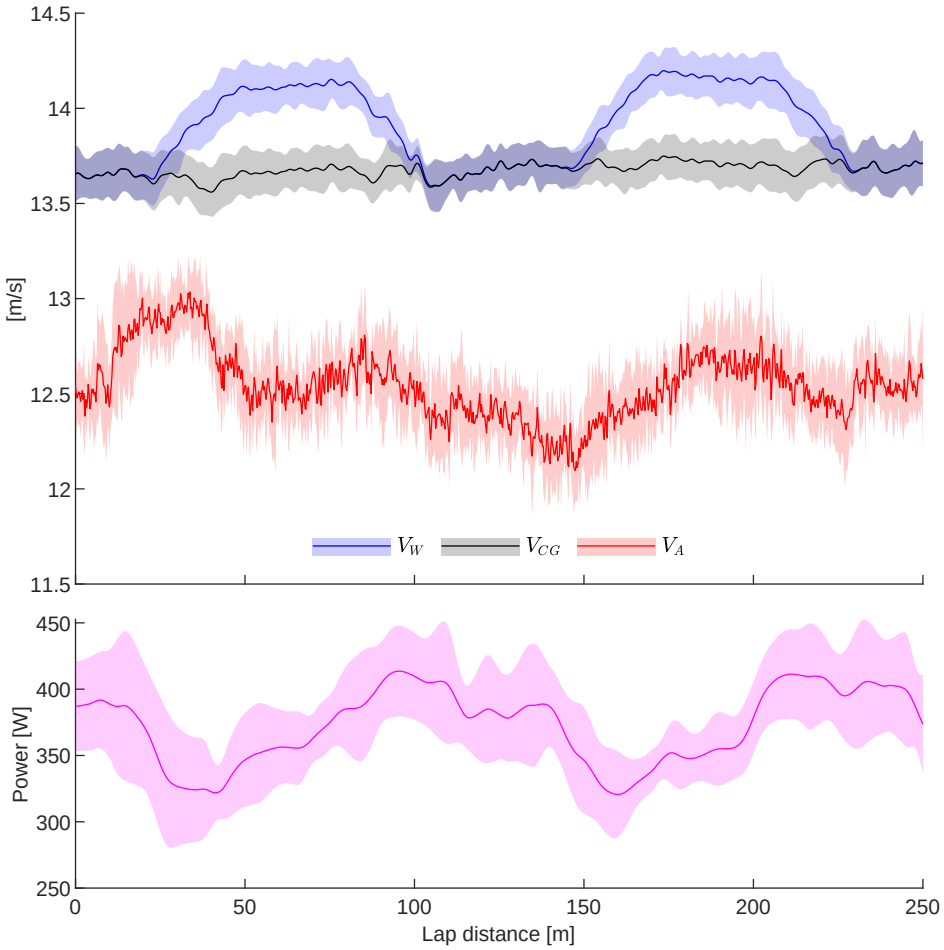


Figure 5.3 Measured wheel speed, calculated centre of gravity speed, measured air speed, and measured power averaged over seven laps with a mean wheel speed of 13.9 m/s. The shaded area indicates ±1 standard deviation.

The measured and calculated steering input angle over a single lap is shown in Figure 5.4, displaying a distinctive variation with position on the track. There is a good agreement between the experimental and calculated steering angle values apart from scatter due to the cadence-frequency roll, steering of the cyclist during each pedal cycle, and general random variation. There is a steady increase during the bend transition, leading to an approximately-constant steering angle throughout the bend. The twin peaks observed in the calculated steering angle are due to the constant turn radius but varying bank angle causing a change in the steering angle. The higher first peak is due to the shallower bank angle on the bend entry compared to the bend exit. This minor change in the steering angle in not seen in the experimentally-measured values as it is within the variations due to other factors not accounted for in the calculations.

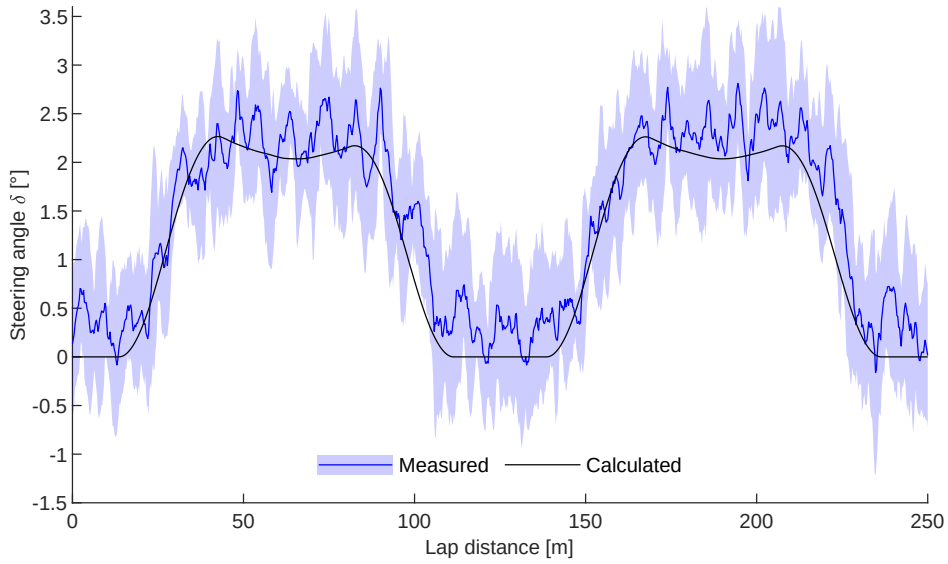


Figure 5.4 Measured and calculated steering input angle averaged over seven laps with a mean wheel speed of 13.9 m/s. The shaded area indicates ±1 standard deviation.

The magnitude of the required steering angle in the bends is dependent on the cyclist's speed, as shown in Figure 5.5 for the bicycle ridden at a series of controlled speeds behind a derny. The measured steering angle along the straights was consistent for all speeds; however, it steadily decreased during the bends with increasing speeds. This differs from the results for steering by Fitton and Symons [12] who calculated an increase in steering angle with

speed until the speed at which the cyclist will roll perpendicular to the bank, after which the steering angle would decrease. This theoretical speed for the present velodrome is 14 m/s at the bend apex. Furthermore, the measured steering angle values were generally greater than the calculated values for low speeds but less than the calculated values for high speeds.

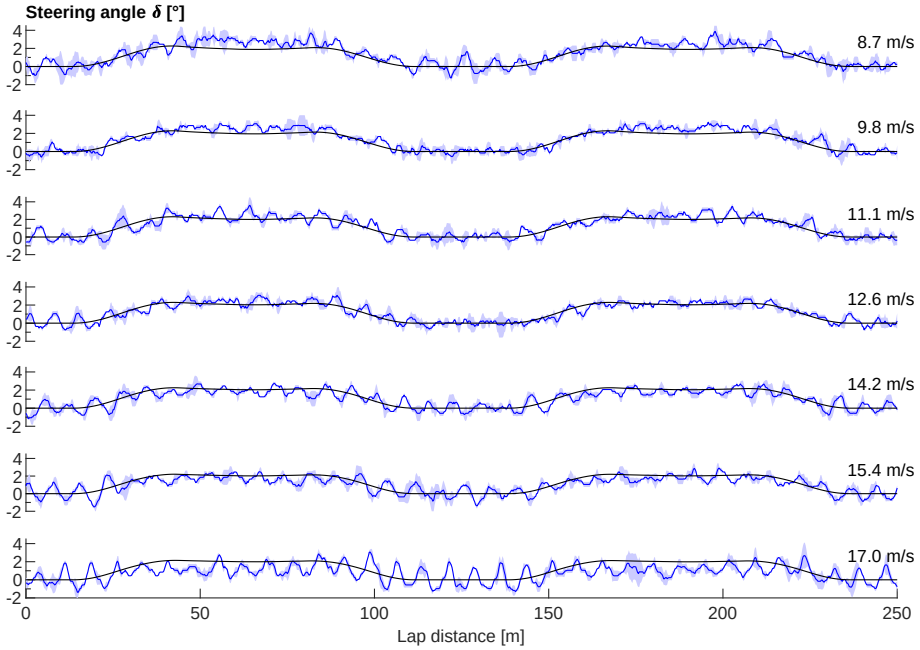


Figure 5.5 Measured (blue) and calculated (black) steering input angle for a range of wheel speeds. Averaged over two laps for each speed.

5.2.3 Changes over a crank cycle

There is a cyclic fluctuation in the steering angle within each pedal cycle, where the rider is found to oscillate the front wheel side to side. The magnitude of this steering angle fluctuation increases with the cyclist's speed, as shown in Figure 5.6. This figure's data has had the mean value of each pedal cycle subtracted to isolate it from the effects of lap position. The results show that there is minimal fluctuation in steering input within a crank cycle at low speeds, whilst at higher speeds there is an increasing oscillation with a maximum value at approximately 160° to 170°. This indicates that the cyclist will turn the front wheel and handlebars in the direction of the leg currently producing the power stroke. The steering angle is seen to oscillate ±1.5° through each pedal stroke at 17 m/s, less than the ±2.5° observed by Kyle [37] who did not mention at what speed it was recorded. This oscillation

can be expected to increase the tyre rolling resistance by creating increased tyre scrubbing, and also change the yaw angle of the airflow incident on the front wheel, thereby influencing the direction of flow and turbulence over the wheel and rest of the bicycle.

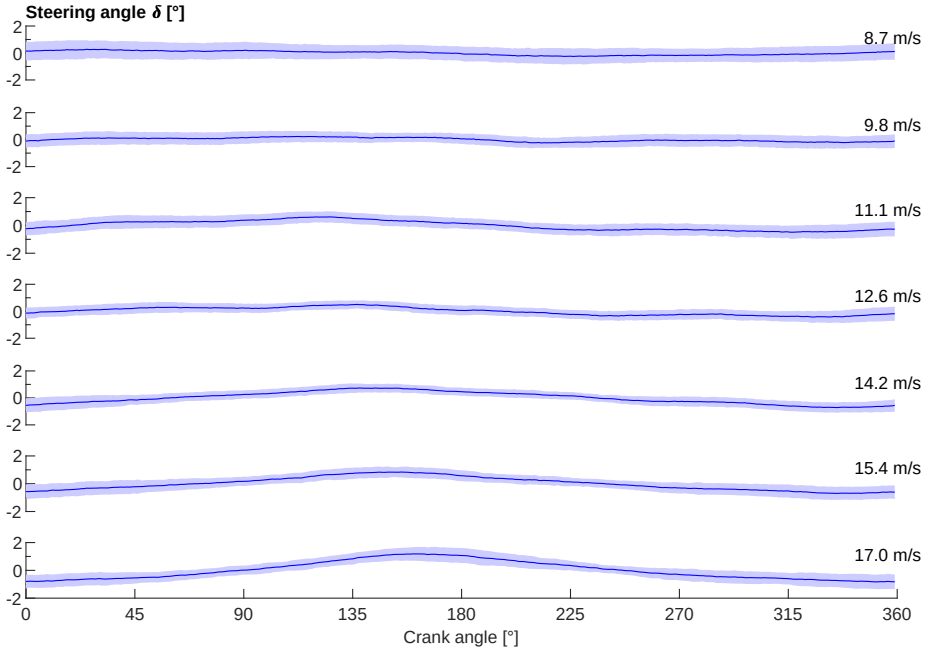


Figure 5.6 Measured steering angle over each crank cycle for a range of wheel speeds. The shaded area indicates ±1 standard deviation. Averaged over two laps for each speed.

5.2.4 Turbulence and wakes

A specific test was conducted during a training session warm-up where there was a group of 15 cyclists riding in a bunch around the velodrome and the primary bicycle was ridden approximately half a lap behind. A second test was conducted with just the primary bicycle ridden solo around the empty track after the velodrome airflow had been allowed to settle for 15 minutes. These two tests were intended to determine if there was any buildup in the wake of a cyclist that circulates the velodrome, and to measure changes in turbulence.

A key measure of the air flow relative to the bicycle/rider is the normalised airspeed, $K = V_A / V_W$, which measures the ratio between the airspeed and the wheel speed and can be used to indicate a tail or head wind. Another measure is the turbulence intensity, which was calculated in the three

orthogonal directions as well as the total component. Intensity calculations were performed with Reynolds decomposition [139] based on fluctuations above the velocity signal filtered with a Savitzky-Golay filter with a window size equal to the mean cadence period, as detailed in Fitzgerald et al. [142] Integral length scales of turbulence over each lap were also calculated based on velocity fluctuations in the three orthogonal directions following Emes et al. [163]. Results were averaged over 6 laps for both the empty-track and warm-up tests and are shown in Table 5.1.

Table 5.1 Comparison of velocity and turbulence measurements for the empty track test (1 cyclist) and the warm-up test (16 total cyclists on the track), averaged over 6 laps for each test at 13.8 m/s.

		Empty track	Warm-up test
K		0.902	0.851
I_{uvw}	[%]	1.06	2.61
I_{uu}	[%]	1.28	2.60
I_{vv}	[%]	1.00	2.81
I_{ww}	[m]	0.87	2.41
L_u^x	[m]	8.26	6.18
L_v^x	[m]	11.05	6.73
L_w^x	[m]	6.97	1.29

The values for the normalised airspeed are <1 for both tests due to the upstream deceleration of the airflow ahead of the rider and bicycle [32, 142] and the bends reducing the airspeed relative to the wheel speed. Between the warm-up and empty track tests there is a velocity ratio reduction of 0.05 at 13.8 m/s, representing an effective tail-wind of 0.7 m/s. This tailwind is likely to be in the form of a swirling flow that follows the riders around the track and builds up over the course of several laps due to entrainment of the wake. The air speed of 0.7 m/s is a low absolute value, just above the minimum observable speed for a standard hand-held wind anemometer [164], and so is unlikely to be clearly observed by typical track-side stationary measurement.

Considering just the power required to overcome aerodynamic drag (ignoring all other energy losses such as rolling resistance), the relative speed increase achieved with a velocity ratio of K is given by

$$\frac{V(K)}{V(K=1)} = K^{-2/3}. \tag{5.3}$$

So, for a tailwind equal to 5 % of their speed ($K = 0.95$), a cyclist can increase their speed by approximately 3.5 % with the same power output. This simple

equation is a best-case scenario, but it provides a helpful indication that becomes more accurate at higher speeds.

In addition to the change in airspeed, there is also an increase in the turbulence when riding in the wake of a series of riders. When riding half a lap behind the other cyclists, the turbulence intensity of the streamwise flow component approximately doubles, whereas the spanwise and vertical components triple relative to their empty track values which indicates further mixing of the flow in all directions. The ratios I_{uu}/I_{vv}, I_{uu}/I_{ww}, and I_{vv}/I_{ww} also converge closer to 1, as the flow becomes more 'normalised' to isotropic turbulence. Furthermore, the integral length scale of the streamwise component is reduced by 25 %, spanwise component by 39 %, and vertical component by 81 % relative to empty track values. This demonstrates that the turbulence decays more rapidly, caused by the break-up of larger turbulent eddies. When riding solo the larger turbulent eddies take longer to decay, and so larger length scales are recorded.

5.3 Discussion

There is a good agreement between the measured and calculated roll angle for an isolated cyclist. This is desirable as it demonstrates that with just a measure of wheel speed and an accurate model of the velodrome track geometry, the roll angle can be determined for an individual pursuit with a lap-averaged RMS error range of 1.9° to 4.9°. Several models used to predict lap times or calculate aerodynamic drag require this calculation [7, 9–12] but little work has been done verifying this intermediate result. The accuracy of the roll angle calculations is highly dependent on the accuracy of the modelled bicycle turn curvature and it decreases with higher speeds as the cyclist will tend to deviate further from the velodrome datum line and ride wider in the straights. Using an adjustable track geometry model [160], it would be possible to replicate this deviation by creating an artificial cyclist path with a wider track span, an increased lap length, and an identical circular arc bend. This keeps the bend apex in the same position but shortens the straights and extends the bend transition length to simulate a cyclist riding wide along the straights.

The calculated velocity of the centre of gravity was shown to be relatively constant throughout the lap when the cyclist was instructed to maintain a constant lap time. This is in contrast to the wheel speed which showed a substantial increase in the bends, and the power which decreased at the start of the bends before steadily increasing as the cyclist exited the bends. This variation in power has been previously observed by Craig and Norton [46]

who specify a minimum power output at the point of highest velocity in the bends for a 4000 m individual pursuit. The reason for this power decrease in a bend is unclear from a simple overview of the typical track cycling power demand model [9–12]. The aerodynamic drag should remain relatively constant through a bend as V_A can be reasonably approximated as V_{CG}, with a minor variation from the influence of cornering flow [142]. In contrast, the power demand from rolling resistance is likely to increase due to the increased wheel speed and centrifugal force. The decrease in power is thus likely to be due to changes in kinetic and potential energy from the motion of the centre of gravity through the transitions. When leaning into a bend, there is a decrease in potential energy which is transformed into forward motion, increasing the wheel speed and decreasing the power demand. The acceleration of the CG would then be reversed when exiting the bends. Fitton and Symons [12] include this change in potential energy in their mathematical model as both a positive and negative influence on power.

This work presents measured and calculated steering angles around a velodrome track, showing a steering angle of approximately 2° in the bends and up to a ±1.5° oscillation within each pedal cycle. These observations are important as a track cyclist experiences increased scrubbing resistance when the front wheel is turned away from the direction of travel [9, 37]. The change in steering angle can also influence the airflow around the front of the bicycle, inducing a further airflow yaw angle and changing the aerodynamic profile of the bicycle front [159].

The increased tailwind observed with other riders on the track is a feature that has been commented on in prior work, but to date only anecdotal evidence has been supplied. Fitton et al. [95] measured an un-specified speed of airflow tangential to the direction of motion of a team pursuit squad. Spoelstra et al. [25] describe a "systematic tailwind" from the motion of a single cyclist in a closed hall. D'Auteuil et al. [70] describe this flow entrainment on speed skating ovals where airspeeds up to 1.6 m/s were postulated. This artificial tailwind can reduce the aerodynamic drag experienced by a cyclist; as an example, the earlier suggested speed increase of 3.5 % results in an 8.4 s time advantage over a 4 minute race. However, if they remain half a lap apart, this tailwind is likely to impact all competitors on the track equally.

The increasing turbulence observed when behind a group of riders, even when they are 125 m ahead of a cyclist, is an important result as the majority of cycling aerodynamic research is conducted using low-turbulence wind tunnels or computational fluid dynamics models [38, 142, 156, 158]. Turbulence properties can change the characteristics of the flow around a rider, particularly the initiation of laminar-to-turbulent transition in the boundary

layer, which dictates the occurrence of the drag crisis [33, 60, 165]. It has been previously shown for speed skating, which operates in a very similar Reynolds number range to track cycling, that replicating on-track turbulence in a wind tunnel can induce the drag crisis at a lower wind speed compared to low-turbulence results [70]. Further work on large commercial vehicles has also shown the importance of replicating the real-world turbulence for aerodynamic research [65, 66]. This has an implication for cycling research as the primary method for drag reduction of the rider is through the use of artificial roughness to induce the drag crisis [23, 38]. If there is an increased level of atmospheric turbulence, then the drag crisis could be naturally induced on bluff body components and the addition of artificial roughness will increase the skin friction without any corresponding reduction in the pressure drag, increasing the total drag rather than reducing it. Detailed investigations into the effects of freestream turbulence on cycling should be an area for future research.

5.4 Conclusion

This paper outlines a series of measurements from an instrumented track bicycle in a velodrome. The roll angle is measured and compared to theoretical calculations, showing good agreement when the cyclist follows the track datum line. Measurements of the steering angle show reasonable agreement with calculated values and show an approximately 2° turn in the bends as well as an increasing oscillation over the pedal cycle with increasing speeds. There is a change in the airflow when other riders are present, creating a swirling flow around the track, reducing the apparent headwind and increasing the freestream turbulence experienced by an isolated cyclist. This swirling and turbulent flow could have an impact on potential drag reductions for track cycling.

5.5 Methods

5.5.1 Instrumented bicycles

Testing was completed with the primary bicycle (55 cm Top Tube, 52 cm Seat Tube, Hillbrick Pista, Australia) shown in Figure 5.7a. Two 4-hole pressure probes (Cobra, TFI, Australia), with the first located anterior to the head-tube and the second between the rider's legs, provides 3 components of velocity at a 2500 Hz sampling rate. Data from the middle probe (#2 in Figure 5.7a) is not presented here and can be found in Fitzgerald et al. [159]. Magnetic

reed switches on the rear wheel and the cranks provide wheel speed and pedalling cadence, respectively. An optical switch measures the crank angle with a measurement tolerance of $360°/53 = 6.8°$ using the method detailed in Fitzgerald et al. [159]. A push-button placed on the handlebars is used for the rider to signal particular events and for time synchronisation between different Data Acquisition Systems (DAQ). A non-contact rotating analogue rotary position sensor is mounted to the top of the steering axis and records the steering angle with a 0.4° resolution at a 500 Hz sampling frequency. Two beacon transmitters placed at either pursuit line in the middle of the straights were detected by a receiver mounted on the bicycle, providing accurate times of every half-lap. A crank-based power meter recorded the rider's input power and cadence (Schoberer Rad Meßtechnik (SRM), Germany). The aerodynamic data, wheel speed, cadence, crank angle, and push button signals were recorded by one DAQ, (TFI, Australia), whilst the steering angle, beacon receiver, cadence, and push button signals were recorded by a second DAQ (Pi Research, United Kingdom), and the power and cadence by a third (SRM PowerControl V). The same signal from the cadence sensor and push button was recorded by all DAQs for common-time synchronisation.



(a) **(b)**

Figure 5.7 (a) Primary bicycle used for testing and **(b)** bicycle coordinate system.

A second track bicycle (54 cm Cervélo T4, Canada), known as the standard bicycle, had a 9-axis Inertial Measurement Unit (IMU), including a 3D accelerometer, 3D gyroscope and 3D magnetometer, firmly mounted posterior to the seat tube. The IMU sensor outputs were fused with a

commercial Kalman filtering system (Xsens Kalman Filter) to calculate 3D orientation measurements. This bicycle had a crank-based SRM power meter, cadence sensor and a five-magnet wheel speed sensor for improved speed resolution. Lap timing was recorded with a beacon receiver which detected the transmitters placed at both pursuit lines. All data was simultaneously logged with a single custom-built DAQ system. The standard bicycle does not have the bulky pannier rack or probe holders and so doesn't have the capacity to record the aerodynamic data, crank angle, or steering angle. However, this DAQ system is small and lightweight and so has a negligible influence on the aerodynamics or mass distribution of the bicycle, permitting it to be ridden in a 'race ready' state. This enabled testing of the roll angle at higher speeds.

The pressure probe has a manufacturer-specified accuracy of ±0.3 m/s and ±1° in yaw and pitch for speeds of 2–30 m/s in a ±45° cone, with a frequency response of 600 Hz and 16 bit digital resolution. The probe was aligned to the bicycle frame at the velodrome track with a custom-built alignment fan with an estimated alignment error of ±0.5° in yaw and pitch angles. The IMU has an angular resolution of 0.05°, dynamic accuracy of 2°, and a 100 Hz sampling rate. The power meter has 8 strain gauges with an accuracy of ±0.5 %.

The bicycles were ridden by two elite male cyclists who provided informed consent before participating. All experimental methods were performed according to relevant guidelines and regulations, and the procedures were approved by the University of Adelaide Human Research Ethics Committee (H-2019-018). The rider's lap times were paced by their coach with instructions to maintain a speed that provided as consistent a lap time as possible. The cyclist maintained a time-trial position on the bicycles and no instructions on how to ride were provided. Testing behind the derny involved two laps at a consistent speed interspaced with an accelerating lap to achieve the next consistent speed.

5.5.2 Velodrome

Testing was conducted at the Adelaide SuperDrome with a 250 m lap length as defined by the black datum line marked on the track surface. The track geometry was measured by a theodolite survey, providing detailed 3D coordinates of the velodrome surface. A custom mathematical model with an apex turn radius of 21.5 m and track span of 45 m was fitted to the measured geometric data, with the method fully detailed in Fitzgerald et al. [160]. This model has G^3 geometric continuity across the lap, providing continuous acceleration and roll rate. There is no change in elevation of the modelled datum line. Measurements of the bank angle were taken from the theodolite

data and checked with an inclinometer.

5.5.3 Errors and limitations

One of the errors in this testing is that the rider does not always exactly follow the datum line; rather they will generally ride high in the straights and then come in close around the bends. There is also a certain level of variability in the bicycle path which can serve to increase the ridden distance compared to the official lap distance. The extent of this discrepancy can be estimated by calculating the ridden distance around the track from the wheel speed sensor, and it was found that the rider rode an extra 2.8 ± 0.67 m (mean ± standard deviation) each lap. This will impact the true turn radius at each position around the velodrome, influencing theoretical calculations of ϕ, V_{CG}, and δ. The magnitude of this error is influenced by the skill and experience of the cyclist, with professional athletes trained to ride with a steady pace and little deviation from the datum line.

The cyclist and bicycle are modelled as a combined point mass at the centre of gravity in the symmetry plane, ignoring the influence of any features such as bicycle geometry, gyroscopic effects, movement of the cyclist/bicycle due to pedalling, or general movement of the cyclist. The calculations assume that the steering input is small and thus does not influence calculations of roll [12]. In addition, lateral aerodynamic forces due to curved aerodynamic flow and turning of the front wheel are not considered, which could have an impact on both roll and steering angles. The results presented are for a steady-state lap where large accelerations, such as occur in sprinting, do not have an influence.

The largest limitation of this study is the use of a single cyclist for each bicycle rather than testing a variety of riders. Different cyclists may have different styles of riding and follow different paths around the velodrome, which could influence roll angles, power output, and steering angles. This was a pilot study to observe the major effects, and future work could involve the testing of a variety of cyclists to achieve a more representative observation of the general professional cycling population. Additionally, this experiment has been conducted at only one velodrome, and different velodromes have different geometries, so these results may not be representative of all velodromes. However, the overall geometries of most 250 m velodromes are very similar, having small differences between straight lengths and bend radii, with the largest differences being with banking styles [160]. With an accurate model of the track geometry for a particular velodrome, the overall results presented here could be replicated at any velodrome.

— Chapter 6 —

The influence of wheels and cadence

To further understand the results from Chapter 3, this chapter details a wind tunnel study of the flow observed in front of the bicycle and between the rider's legs using 3-component velocity probes. It is shown that the front wheel has a large influence on the flow observed by the front probe, particularly when the bicycle is at a geometric yaw angle to the flow. This helps to explain the large aerodynamic yaw measured on a velodrome bend in Chapter 3. The combination of the curved airflow and the front wheel steering angle can produce a large induced aerodynamic yaw, as measured by the probe.

Additionally, further testing with a second aerodynamic probe located between the rider's legs is completed to observe the flow around the middle of the bicycle frame. Three different experimental methods (potential flow calculations, wind tunnel tests with a mannequin and velodrome tests with a live rider) all show a periodic variation in the flow with the pedalling cadence. The results can be used for frame design around the rear half of the bicycle and skinsuit/sock optimisation.

This chapter has been published in the *Journal of Wind Engineering and Industrial Aerodynamics* and has been reformatted for this thesis. The as-published article is available at:

Fitzgerald, S., Kelso, R., Grimshaw, P., and Warr, A. (2020) 'Observations of the flow experienced by a track cyclist using velodrome, wind tunnel, and potential flow investigations with an instrumented bicycle' *Journal of Wind Engineering and Industrial Aerodynamics*, 206, 104374, DOI: 10.1016/j.jweia.2020.104374.

Statement of Authorship

Title of Paper	Observations of the flow experienced by a track cyclist using velodrome, wind tunnel, and potential flow investigations with an instrumented bicycle
Publication Status	☑ Published ☐ Accepted for Publication ☐ Submitted for Publication ☐ Unpublished and Unsubmitted work written in manuscript style
Publication Details	Fitzgerald, S., Kelso, R., Grimshaw, P., Warr, A. (2020). 'Observations of the flow experienced by a track cyclist using velodrome, wind tunnel, and potential flow investigations with an instrumented bicycle' *Journal of Wind Engineering and Industrial Aerodynamics,* 206, 104374, DOI: 10.1016/j.jweia.2020.104374.

Principal Author

Name of Principal Author (Candidate)	Shaun Fitzgerald		
Contribution to the Paper	Co-designed research concept. Developed the experimental equipment for the bicycle. Performed experiments and analysed all data. Conceptualised and developed the potential flow model. Prepared the manuscript and generated all figures. Acted as corresponding author.		
Overall percentage (%)	80		
Certification:	This paper reports on original research I conducted during the period of my Higher Degree by Research candidature and is not subject to any obligations or contractual agreements with a third party that would constrain its inclusion in this thesis. I am the primary author of this paper.		
Signature		Date	12/11/2021

Co-Author Contributions

By signing the Statement of Authorship, each author certifies that:

i. the candidate's stated contribution to the publication is accurate (as detailed above);

ii. permission is granted for the candidate in include the publication in the thesis; and

iii. the sum of all co-author contributions is equal to 100% less the candidate's stated contribution.

Name of Co-Author	Richard Kelso		
Contribution to the Paper	Co-designed research concept. Guided research direction, supervised work development and interpretation, helped generate ideas and concepts, and edited the manuscript.		
Signature		Date	15/11/2021

Name of Co-Author	Paul Grimshaw		
Contribution to the Paper	Guided research direction, supervised work development and interpretation, helped generate ideas and concepts, and edited the manuscript.		
Signature		Date	15/11/21

Name of Co-Author	Andy Warr		
Contribution to the Paper	Guided research direction, supervised work development and interpretation, helped generate ideas and concepts, and edited the manuscript.		
Signature		Date	16/11/21

Observations of the flow experienced by a track cyclist using velodrome, wind tunnel, and potential flow investigations with an instrumented bicycle

S. Fitzgerald, R. Kelso, P. Grimshaw, A. Warr

Abstract

A wind tunnel investigation into the effects of yaw on a track bicycle, ridden by an anatomically-accurate pedalling mannequin, is completed and the results are compared with on-track velodrome data. The results show that there is an amplification effect with a minor bicycle geometric yaw creating a major aerodynamic yaw anterior to the bicycle. The magnitude of this aerodynamic yaw angle amplification increases with increasing front wheel rim depth, with a disc wheel producing the most pronounced effect. A second study into the effects of pedalling legs is also completed with the pedalling mannequin. A 2D potential flow model of the leg movement is created and compared to both wind tunnel data with a pedalling mannequin and velodrome data with a cyclist. The results show a reasonable agreement between the model and both the wind tunnel and velodrome data. There is a large variation in the airflow compared to the freestream that is due to the motion of the legs with a minor difference due to the effect of cadence. The data presented here is useful for bicycle design because it demonstrates and quantifies the aerodynamic influence across different parts of the bicycle.

6.1 Introduction

The aerodynamics of cycling is an area of intense research with multiple groups working on differing aspects [38]. As aerodynamic drag is the dominant resistive force for all cycling race speeds [1], there has been extensive work on quantifying the drag force and researching how it can be reduced [23]. Recently, there has also been a focus on understanding the flow field around a cyclist, particularly the wake, looking at how differing body and bicycle geometry affects the production of aerodynamic drag [33].

Substantial work has been completed on bicycle wheel aerodynamics both in the wind tunnel [166] and with Computational Fluid Dynamics (CFD) [167], with isolated wheels [168] and complete setups with a rider or mannequin model [31]. Most of these papers report the forces and moments produced

by a variety of wheel types and configurations, but there are few that report complete flow-fields in the wake of a bicycle wheel. A few exceptions are work by Godo et al. [169] and Malizia and Blocken [64], however both of these studies are completed on a single isolated wheel, without the accompanying bicycle and rider.

There have been relatively few studies on the effects of leg position and pedalling cadence on the aerodynamics of cycling. An early comprehensive study was completed by Crouch et al. [48] who measured the wake and aerodynamic drag of a stationary articulated mannequin at 15° crank angle increments. This research found a distinct variation in the wake and associated drag, dependent upon the leg position. The same group extended their study by dynamically measuring the wake of a pedalling mannequin at a series of cadences from 0 to 100 revolutions per minute (rpm) [49]. This demonstrated that the flow around a cyclist is quasi-steady up to a cadence of 100 rpm. The non-dimensionalised measure of the influence of pedalling cadence relative to the freestream velocity, known as the reduced pedalling frequency, k, is given by Equation (6.1), as introduced for cycling by Crouch et al. [48]. Here r is the crank length, f is the pedalling frequency, and U_∞ is the freestream velocity.

$$k = \frac{2\pi r f}{U_\infty} \tag{6.1}$$

Baidya et al. [81] and Chan [170] studied the wake of an isolated pedalling mannequin that consisted of the cranks and a pair of legs. The model used in Chan [170] lacks notable features such as the bicycle and a cyclist upper-body, but the author is able to provide a reasonable comparison to full-body mannequin data and the work shows that the quasi-steady conclusion of Crouch et al. [49] is largely accurate. More recently, a study was completed by Spoelstra et al. [85] who used a novel method of Particle Image Velocimetry (PIV) to measure the wake of a cyclist who rode through an enclosed tent. This provides an examination of the flow field of a cyclist outside of a controlled wind tunnel or through the use of computational methods. Griffith et al. [50] created a numerical model of a simplified, segmented cyclist with moving legs, assessing the difference between a dynamic and a static calculation. All of these studies measured the wake of either a dynamically-pedalling cyclist or a static cyclist and provide insight into the drag variation with a cyclist's pedal cycle.

The airflow experienced by a track cyclist in a velodrome has been shown to be highly variant, with particularly high yaw angles ahead of the bicycle during cornering [142]. This study demonstrated an airflow dependence on the position within a team pursuit group, location in the velodrome, and

cadence of the rider. The change in incident airflow around the bends in the velodrome was shown to match the theoretically calculated value for the pitch angle, but it greatly exceeded the calculated yaw angle. The exact cause of this amplified yaw angle is unknown and so further work has been completed to decompose the variation in airflow experienced by a track cyclist when traversing a velodrome bend. This current research is an extension of the work by Fitzgerald et al. [142] where some of the results observed are expanded and further detailed through wind tunnel experiments and a potential flow study.

6.2 Methods

6.2.1 Velodrome testing

Preliminary flow visualisation was used to observe the flow between a cyclist's legs on a standard track bicycle ridden on an indoor velodrome. The setup is shown in Figure 6.1a and consisted of a series of three wool tufts tied to a line of fishing wire between the nose of the saddle and the bicycle top tube. A video camera (120 fps, GoPro, USA) recorded the movement of the wool tufts for four laps of the velodrome with both seated and standing pedalling. Two still frames from the same pedal cycle are shown in Figure 6.1b and a video of the results is available as supplementary material online. The results indicated a wide variation in flow angles during a single pedal cycle and so further testing was undertaken using a modified version of the same instrumented bicycle used in Fitzgerald et al. [142].

The bicycle used for all further testing is a size medium (55 cm Top Tube, 52 cm Seat Tube) Hillbrick Pista (Hillbrick, Australia) with twin 700c Zipp Super-9 tubular disk wheels (Zipp, USA). Cantilevered anterior to the head tube is a four-hole pressure probe (Cobra probe, TFI, Australia), and a second probe is mounted anterior to the seat tube, between the rider's legs. Two magnetic reed switches provide wheel speed and pedalling cadence. A slotted optical switch consisting of an infra-red Light Emitting Diode (LED) and a receiving photodiode was mounted on the chain-stay so that the front chaining teeth passed between the LED and receiver. This generated a signal pulse with every passing tooth (53 in total) and, when combined with the cadence reed switch for indication of the start of each pedal cycle, this provided the crank angle over the course of each pedal cycle with a measurement tolerance of $360°/53 = 6.8°$, similar to the method used by Crouch et al. [49]. These sensors and the pressure probes were sampled at 2500 Hz and recorded simultaneously by a data acquisition system (DAQ) (TFI, Australia).

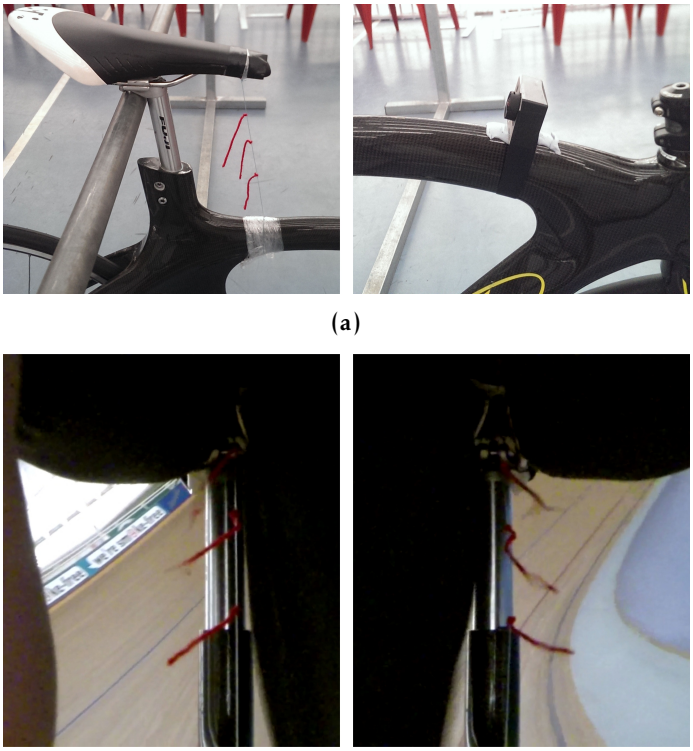


Figure 6.1 On-track flow visualisation displaying **(a)** the setup, and **(b)** two still images from the video showing the extent of the flow movement during one pedal cycle.

Testing with the instrumented bicycle was completed at the Adelaide SuperDrome by a national-level elite athlete following the procedure outlined in Fitzgerald et al. [142]. The athlete provided informed consent and testing was conducted according to the University of Adelaide Human Research Ethics Committee approval H-2019-018. Tests were conducted with the cyclist riding along the black line on an empty track in simulation of an individual pursuit race. Lap times were recorded with two on-track beacons that recorded the time that the bicycle passed either pursuit line. This provided two timing signals per lap. The data was averaged over all crank cycles over the course of 8 laps, and the results from both turn and straight track segments were combined.

The coordinate system for this work is defined by Figure 6.2 with positive yaw (δ) indicating airflow from the left of the bicycle, positive pitch (θ) indicating up-flow, and the crank angle (ζ) based on a zero position with the cranks horizontal and the right crank forwards. The crank angle was calculated from the optical switch and reed switch and the aerodynamic data

was averaged between each pair of optical switch signals. The values for each crank angle were then averaged over all crank cycles to obtain a representative value for a single complete crank cycle. The x-y-z coordinate system is defined relative to the bicycle with an origin at the centre of the bottom bracket, x directed towards the rear, y towards the right and z upwards. The three components of flow velocity are given by u; v; and w, the yaw angle is the flow angle in the transverse plane, and the pitch angle is the flow angle in the sagittal plane. For the purposes of this work, the air velocity will be defined by its vector components of two angles, namely yaw and pitch, and either its absolute or normalised magnitude. This notation is used as it provides the greatest ability to nondimensionalise the results.

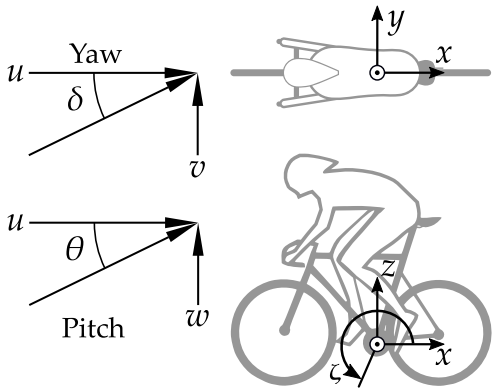


Figure 6.2 Bicycle coordinate system.

6.2.2 Wind tunnel testing

In order to further understand the velodrome data presented in Fitzgerald et al. [142], a study was completed in the University of Adelaide Thebarton wind tunnel. This is a closed-return wind tunnel with a cross section of 2.75 m × 2 m, a maximum speed of 30 m/s and turbulence intensity <0.5 %.

A pedalling mannequin has been developed at the University of Adelaide based on a 3D scan of an elite cyclist. The head of the scanned model was replaced with a generic headform on an adjustable neck and the body was internally modified and split into several components to provide movable joints before 3D printing all the parts in Polylactic Acid (PLA) plastic. The mannequin has a fixed ankle, pin joints in the hips and knees, and manually-adjustable shoulders, elbows, and neck to allow it to be placed onto any bicycle in a position representative of a pursuit cyclist. The surface of the mannequin has been sanded smooth and testing was conducted without any clothing or helmet on the mannequin for maximum repeatability. Due to structural

strength limitations of the 3D printed plastic, the pedalling cadence of the mannequin was limited to 80 rpm for continuous running. For brief periods this limit was exceeded to reach of a cadence of 100 rpm.

A wind tunnel measurement rig that mounts a bicycle on upright struts holding the front and rear axles, has also been constructed. The bicycle is mounted on a raised platform with a splitter plate to minimise the floor boundary layer thickness and each wheel is rotated by a separate electric motor and roller mounted flush with the platform surface. The speeds of the motors are independently controlled through their input voltage and monitored by hall-effect tachometers. The pedalling of the mannequin is driven by the rear roller through the fixed chain drive of the bicycle. Using separately-controlled rollers provides the ability to match the speed of the front wheel to the wind speed whilst also pedalling with a separately chosen cadence. This was required for this series of tests as the spinning front wheel has an impact on bicycle aerodynamics and this factor was able to be maintained as a constant throughout all tests. The mannequin is firmly fixed to the bicycle at the elbows and buttock and wears shoes with cleats to remain fixed in the pedals. The legs are articulated by driving the rear wheel at a constant rotational speed. The complete bicycle and mannequin setup is firmly fixed to the base through the wheel axles to prevent rocking and is shown in Figure 6.3.

The two Cobra probes were aligned by first geometrically aligning a custom-built fan with the bicycle and then aligning the probe with the flow produced by the fan. This fan was able to be situated between the down and seat tubes to align the middle probe and was used trackside at the velodrome as well as at the wind tunnel. An estimate for the alignment error of the probe is ±0.5°. The wooden block visible underneath the mannequin arms in the picture was included to achieve the required stack height to prevent the mannequin's thighs from interfering with the torso. The combined frontal area of the bicycle and mannequin was calculated by taking a frontal photo with a reference area and digitally counting pixels following the process outlined in Caddy et al. [11]. Photographs were taken with the camera lens centred to the top of the bicycle head tube at a distance of 7 m and with a 40 mm focal length in order to minimise perspective error and maximise detail. The mannequin frontal area was compared with the tunnel area and a blockage ratio of 5.9 % at 0° bicycle yaw was calculated. For the maximum geometric yaw angle of the bicycle (15°) this increases to 12 %. This is an acceptable level of blockage according to Barlow et al. [61] who detail a typical range of 1–10 % with 5 % being common. No blockage corrections were applied as they have a negligible effect on the flow angles, and the velocity magnitudes are only noticeably affected by the corrections at the largest bicycle yaw angles. Furthermore,

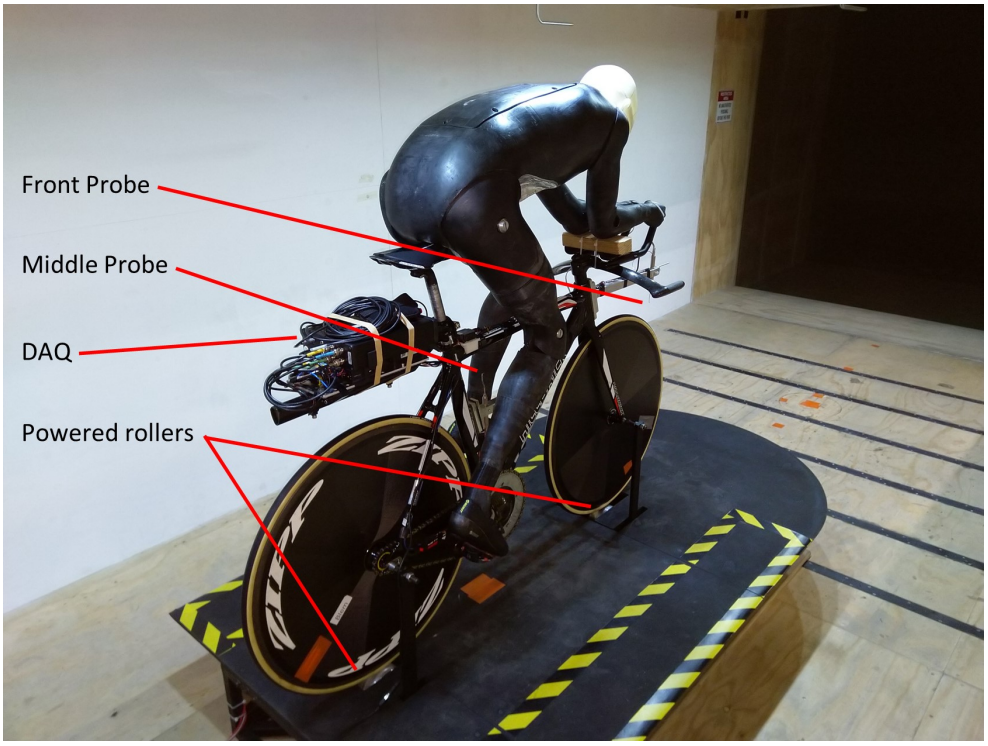


Figure 6.3 Pedalling mannequin and instrumented bicycle on the measurement rig in the wind tunnel.

as the effects of blockage differ at the two probe locations (anterior to the head tube and seat tube respectively), conventional blockage corrections were deemed unreliable.

The Cobra probes have 16 bit resolution and an accuracy of ±0.3 m/s and ±1° for the flow range of 2–30 m/s in a ±45° cone. The front Cobra probe has a frequency response of 600 Hz and the probe between the legs, which is in a more turbulent flow, has a higher frequency response of 2000 Hz. The dynamic pressure in the wind tunnel was measured simultaneously by twin Pitot-static tubes placed 350 mm either side of the tunnel centre line and recorded by two digital manometers (Extech, USA) with a resolution of 1 Pa and an accuracy of 0.3 % full scale. The temperature in the tunnel flow was recorded throughout the duration of each wind tunnel test by two Resistance Temperature Detector thermometers (Centre Technology Corp, Taiwan) with an accuracy of ±0.1 °C and resolution of 0.01 °C. A combined thermometer/barometer/hygrometer (Testo, Germany) was used to monitor the atmospheric pressure and relative humidity with an accuracy of ±3 hPa and ±2 % respectively. The air density was calculated from the temperature, pressure, and humidity measurements according to Picard et al. [39] and used to normalise all tests to a common

density.

For each wind tunnel test datapoint the flow was allowed to settle to a steady state and then data was recorded for 40 s. All tests were performed twice with the combined average and standard error of both tests calculated. Tests conducted by geometrically yawing the bicycle through a sweep angle of $-15°$ to $+15°$ were completed by starting the bicycle at $0°$ and rotating outwards for both positive and negative geometric yaw angles to reduce aerodynamic hysteresis due to the bicycle yaw direction. This also provided three separate results for the $0°$ yaw position, at the beginning, middle and end of each test, providing a check to ensure the probe calibrations had not drifted during a test.

Testing was conducted by completing all the frame-only tests in one stage and then adding the mannequin and completing all further tests without removing the mannequin from the bicycle, including changing the front wheel. This greatly increased repeatability by minimising geometric differences that could arise from slightly different placements of the mannequin on the bicycle. An estimation of the combined uncertainty of the experimental error, manufacturer instrumentation error, and random noise was calculated using the methods outlined in Bentley [171]. The resulting uncertainty is represented by error bars provided in Figures 6.8, 6.9 and 6.13.

6.2.3 Potential flow calculations

To complement the experimental results for the flow between a cyclist's legs, flow analysis was undertaken through the use of potential flow theory. Potential flow theory provides a mathematical description of inviscid, irrotational fluid flow through the combination of several fundamental flow features to create a more complex flow field. However this is a greatly simplified model due to the absence of viscosity, and hence no boundary layers, flow separation or wakes are simulated. In addition, this is a two-dimensional model that only simulates the flow in a series of horizontal planes, when in reality the flow between the legs is highly three-dimensional due to the cyclist's body, angled thighs and calves, sloped down tube and rotating front and rear wheels all contributing to vertical flow. A more accurate method would be to create either a complete or partial CFD model of the pedalling legs, but this would be very computationally expensive to complete for all angles of the crank cycle. To the best of the authors' knowledge, there has only been one previously-published CFD study of cyclist with moving legs [50]. A notable difference between the published CFD study and this potential flow model is the considerable difference in solution time with the work of

Griffith et al. [50] limited by a high computational cost. With consideration of these limitations, the potential flow model produces a remarkably similar flow pattern to the experimental data, as will be discussed further in this paper.

The first step of the calculations is to create a three-dimensional model of the mannequin legs and the bicycle frame by approximating the legs as truncated cones and the cranks and bicycle tubes as cylinders, as shown in Figure 6.4. All dimensions were measured from the mannequin and bicycle and are provided in Table 6.1. The primary differences between the analytical model and the physical mannequin are the legs' cross-sectional shapes, their straightness, and the form of the joints. Representing the bicycle's tubes as cylinders is reasonable as the bicycle frame is constructed from approximately circular cross-section aluminium tubing. Each leg's dynamic motion is modelled by a 4-bar linkage based on link AB for the crank, BFEC for the shank (lower leg), and CD for the thigh. Points A and D are grounded revolute joints while points B and C are free revolute joints. The effect of cadence is modelled by rotating link AB at a constant rotational velocity $\dot{\zeta}$. This model is fully determinate and the position, velocity, and acceleration of any point on the leg can be obtained for all crank angles.

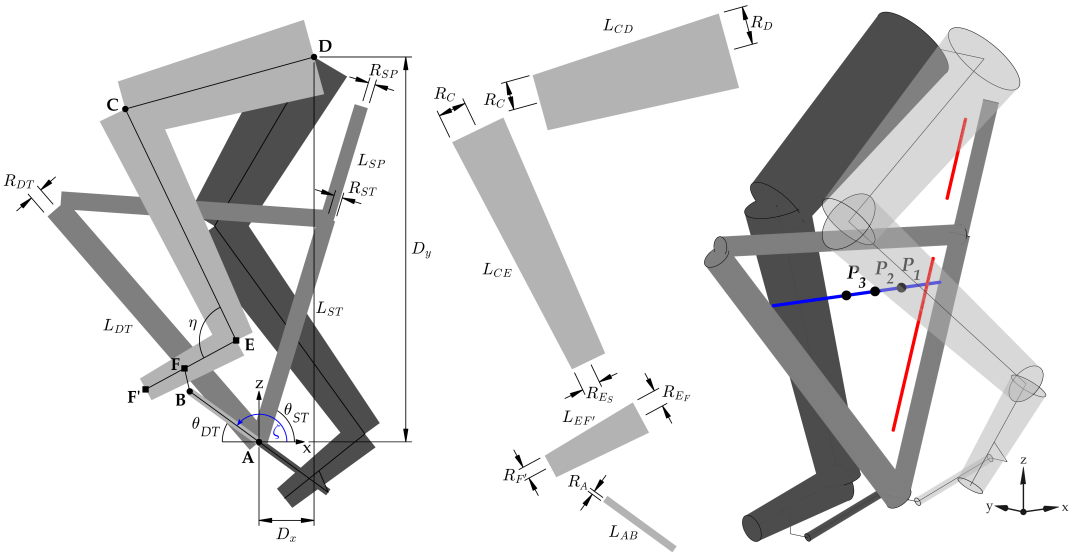


Figure 6.4 The mannequin leg and bicycle model. The foot and shank are one solid body, point F is on the imaginary line BC, and F' is the extension of EF. The three dots labelled P_1, P_2, and P_3 are the locations where experimental measurements were taken and the horizontal (blue) and vertical (red) lines are the locations analysed for Figures 6.11 and 6.12 respectively.

Once the analytical 3D mannequin model was created, a two-dimensional

Table 6.1 Mannequin and bicycle dimensions. The origin is defined at the centre of the bottom bracket.

Name	Symbol	Location [mm] Length [mm] Angle [°]
Crank axis position (x,y,z)	A	(0, ±100, 0)
Hip axis position (x,y,z)	D	(113, ±100, 784)
Probe position 1 (x,y,z)	P_1	(6, 0, 374)
Probe position 2 (x,y,z)	P_2	(-54, 0, 374)
Probe position 3 (x,y,z)	P_3	(-119, 0, 374)
Crank length	L_{AB}	175
Pedal spindle to knee	L_{BC}	590
Knee to hip	L_{CD}	400
Knee to ankle	L_{CE}	523
Ankle to ball of foot	L_{EF}	120
Ball of foot to toes	$L_{FF'}$	90
Crank radius	R_A	10
Knee radius	R_C	58
Hip radius	R_D	79
Ankle radius (shank)	R_E	38
Ankle radius (foot)	R_E	38
Toe radius	$R_{F'}$	38
Seat tube length	L_{ST}	475
Down tube length	L_{DT}	630
Seat post length	L_{SP}	240
Seat tube radius	R_{ST}	18
Down tube radius	R_{DT}	25
Seat post radius	R_{SP}	14
Seat tube/Seat post angle	θ_{ST}	73°
Down tube angle	θ_{DT}	49°
Ankle angle	η	93°

sectional plane of the mannequin and bicycle at the probe tip height was determined by solving for the ellipse that is created when a cone is cut by an angled plane, shown in Figure 6.5 and detailed by Equation (6.2).

$$\begin{aligned}
1 &= \frac{(x-h)^2}{a^2} + \frac{(y-q)^2}{b^2} \\
a &= L\frac{h_e(R_2-R_1) + LR_1\sin\xi}{L^2\sin^2\xi - (R_2-R_1)^2\cos^2\xi} \\
b &= \frac{h_e(R_2-R_1) + LR_1\sin\xi}{\sqrt{L^2\sin^2\xi - (R_2-R_1)^2\cos^2\xi}} \\
h &= \left((R_2-R_1)\frac{h_e(R_2-R_1) + LR_1\sin\xi}{L^2\sin^2\xi - (R_2-R_1)^2\cos^2\xi} + h_e\right)\cot\xi + x_0 \\
q &= y_0
\end{aligned} \tag{6.2}$$

This ellipse has a focus at:

$$c = \sqrt{a^2 - b^2} \tag{6.3}$$

Four ellipses were created from the inclined bicycle seat tube, down tube, left leg, and right leg for all crank angles. The ellipse for each leg was constructed according to Equation (6.2) using the leg component that intersected the horizontal plane. The greatest discrepancy between the model and the physical mannequin occurs during the transition phase when points B, C, or E traverse through the horizontal plane of interest. At these points the ellipse profile differs greatly from the true shape of the joint profile. However, the position of the probe in this investigation was below the knee joint for all crank angles and so this discontinuity is not observed at the primary plane of interest.

Once the physical dimensions of the 2D plane had been constructed, the airflow between the legs could be modelled. Potential flow theory is detailed in the work of Vallentine [172] and others, and hence only a brief outline of the salient points and their use in this case will be presented here. A potential flow is defined by the stream function ϕ which is everywhere tangential to the flow velocity, and the velocity potential ψ which is everywhere normal to ϕ. The equation for a potential flow of uniform velocity (U_∞) on a cartesian grid is given by the complex potential W, where:

$$W = \phi + \psi i = \underbrace{U_\infty x}_{\phi} + \underbrace{U_\infty y}_{\psi}\, i \tag{6.4}$$

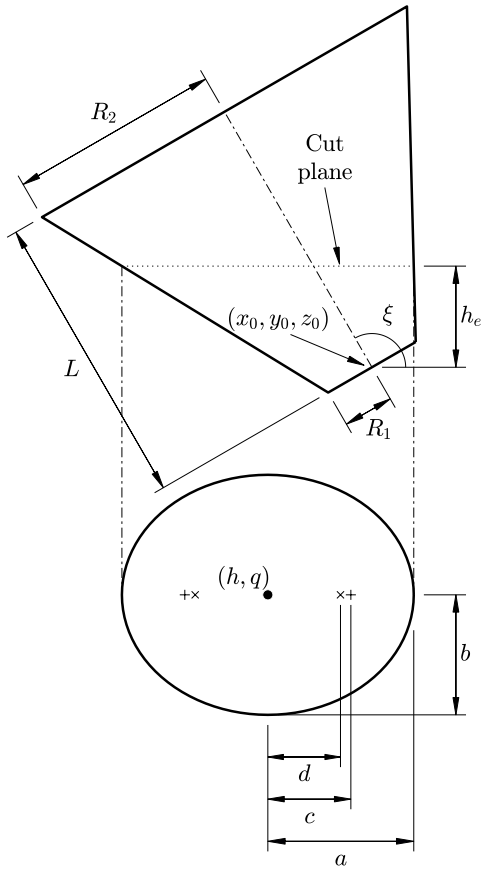


Figure 6.5 The input and output dimensions required to create an ellipse from a cone.

For a point source/sink of strength m, located at (x_j, y_j):

$$W = \pm \left(\underbrace{\frac{m}{2\pi} \log \sqrt{(x-x_j)^2 + (y-y_j)^2}}_{\phi} + \underbrace{\frac{m}{2\pi} \arctan\left(\frac{y-y_j}{x-x_j}\right) i}_{\psi} \right). \tag{6.5}$$

Composite potential flows are created by the summation of multiple features; in this case a Rankine oval is constructed by the addition of a uniform flow and a source/sink pair of identical strength and opposite direction separated by a distance of $2d$ and parallel to the x-axis.

The shape of an ellipse can be approximated by a Rankine oval where the boundary is defined by the curve $\psi = 0$ and represents a solid surface. The centre of the oval is at (h, q) and the source/sink are located at $(h \pm d, q)$. The

maximum half-width of the Rankine oval is found with $\psi(x = h, y = q \pm b) = 0$ and the maximum half-length (stagnation point distance) of the Rankine oval is found when $u = v = 0$ and is given by:

$$s = d\sqrt{\frac{m}{\pi U_\infty d} + 1}. \tag{6.6}$$

The size and shape of the Rankine oval are dictated by the freestream velocity, source/sink strength, and source/sink separation distance. Setting the freestream velocity to match a desired cycling speed, values for the strength (m) and distance (d) can be chosen so that the obtained Rankine oval matches the shape of the cyclist's legs or the bicycle tubes at the desired two-dimensional plane. These values are found by matching the stagnation distance s to the ellipse major-axis a, and the half width to the ellipse minor-axis b by iterating between Equations (6.7) and (6.8) until the results converge. The iteration is started by setting d equal to the ellipse focal distance c (Equation (6.3)).

$$m = \frac{2\pi U_\infty b}{\arctan\left(\frac{2bd}{b^2 - d^2}\right)} \tag{6.7}$$

$$d = \frac{1}{2\pi U_\infty}\left(\sqrt{m^2 + (2\pi U_\infty a)^2} - m\right) \tag{6.8}$$

The potential flow equation for the horizontal plane at the probe tip elevation is then created by the combination of uniform flow and four Rankine ovals representing the elliptical 2D shapes of the down tube, seat tube, and left and right legs. Once the complex potential has been determined the velocity u and v components can be calculated by the partial derivatives of ϕ with respect to x and with respect to y respectively [172]. The results for a single crank angle are shown in Figure 6.6.

The potential flow calculations are constructed on a uniform mesh with 2 mm spacing (113 000 cells) for visual results in contour plots. However, the equations are a continuous, holomorphic function with each mesh point independent of all others, and so the exact values at any particular (x, y) location can be found by directly solving the equation for that exact point, independent of the discretisation of the domain. As such, unlike CFD calculations, the only numerical errors that arise are from double-precision floating point calculations which are rounding errors of the order of 2^{-52} ($\approx 1 \times 10^{-16}$). This provides an extremely efficient method of calculation where a complete flow-field is only constructed for visual purposes; otherwise only the particular points of interest are calculated. In total, to construct the mannequin model and calculate a complete flow-field for all 360° crank

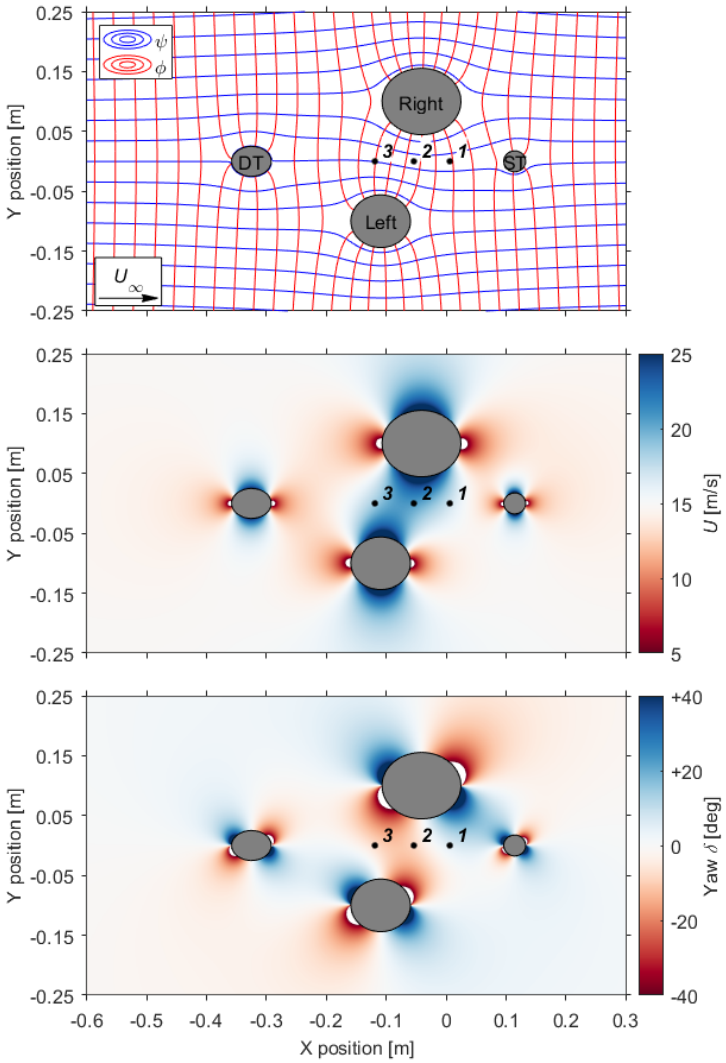


Figure 6.6 The stream function ϕ, velocity potential ψ, total velocity U, and yaw angle δ at a crank angle of 135°. Labels 1, 2, and 3 indicate positions where experimental measurements were taken.

angles in a single plane takes <9 s on a laptop computer (Intel i7-6700HQ at 2.6 GHz)

To summarise the calculation process, the mannequin leg dimensions and position at a single crank angle are calculated using the data in Table 6.1 and the geometry of Figure 6.4. Then Equation (6.2) is used to calculate the four separate ellipses created by the horizontal plane through the down tube, seat tube, left, and right leg. A source/sink pair is then defined for each ellipse with Equations (6.5) to (6.8). The complex potential is then calculated by the summation of each source/sink pair and a freestream flow with Equation (6.4). The u, v and U, δ flow vector components at a given location can then be calculated by derivation of the complex potential.

6.3 Results and discussion

6.3.1 Effect of yawing the bicycle (front probe)

Eight different conditions were tested in the wind tunnel by yawing the bicycle through a sweep of $-15°$ to $+15°$ whilst maintaining a constant tunnel velocity of 15 m/s. The tests involved four different front wheel configurations as shown in Figure 6.7: a disk wheel, a wire-spoked wheel with a deep rim, a wire-spoked wheel with a shallow rim, and no wheel, all with both no rider and the pedalling mannequin. The test with no wheel was conducted by replacing the wheel with a thin metal rod that supported the front end of the frame on the supporting uprights. For all tests with a front wheel fitted, the front wheel was rotated to match the wind tunnel speed and the mannequin pedalled at a reduced frequency of 0.098 (80 rpm). For these tests, where wheel effects are more dominant than cadence effects, it was considered more valuable to match the wind tunnel flow speed and wheel speed with velodrome tests than to match the reduced frequency.



Figure 6.7 The different front wheels tested in the wind tunnel.

The aerodynamic effect at the front Cobra probe due to geometric yawing

the bicycle through a sweep of −15° to +15° is shown in Figure 6.8, with and without the pedalling mannequin for each of the wheel conditions. The total speed measured by the Cobra probe has been normalised by the wind tunnel speed (U/U_∞) and shows an increase in magnitude at higher bicycle-yaw angles for all wheel conditions. Whereas we might expect the aerodynamic yaw angle (relative to the bicycle) would match the bicycle's geometric yaw angle, the measured aerodynamic yaw angle is found to be much greater in magnitude than the geometric yaw angle of the bicycle. The additional (induced) yaw is likely due to the front wheel acting as a lifting body and creating an induced lateral flow at the probe tip. According to Prandtl's lifting line theory [173], the magnitude of this induced flow is proportional to the side force produced by the wheel, with a large induced yaw angle produced by the disc wheel and a much smaller induced yaw angle produced by the two spoked wheels which have only the rim area to create lift. An analysis of the figures in a CFD study on a series of wheels with rim shapes similar to this work by Godo et al. [169] also shows this increase in induced flow near the top of the wheel. The magnitude of the induced flow increases with increasing rim depth, with the maximum induced flow produced by a disc wheel. There is also an induced flow present during the no-wheel condition which is likely due to the whole body of the mannequin, rear wheel and bicycle frame acting as a secondary lifting body, thereby producing a small induced flow at the front of the bicycle. This additional induced velocity effect of the mannequin/rear wheel/frame is present for all wheel configurations across the range of bicycle geometric yaw angles.

There is a noticeable constant offset in the pitch angle between the mannequin and frame-only tests for all bicycle-yaw angles and wheel types. This is due to the upstream influence of the mannequin arms and their supports, inducing a negative pitch angle on the flow. There is also a noticeable offset in the pitch angles between the different wheels which is likely due to three factors. Firstly, for bicycle yaw angles less than 5°, the presence of the wheel immediately below the probe (see Figure 6.7) would induce a positive pitch angle (up-flow) on the flow compared to the no-wheel condition. Secondly, whilst the wheels were replaced and aligned with particular care, there may have been slight differences in wheel diameter and/or tyre width so that the front wheel was fixed at slightly different heights, creating a pitch angle offset at the probe tip. Thirdly, there is a rapid increase in pitch angle when the yaw angle exceeds 5° which is most likely due to the induced velocity of the bicycle, mannequin and front wheel. For the case of the disc wheel, which generates large side forces, the induced upwash from the wheel is shown to be large. This is also shown in the measured U/U_∞ values for the

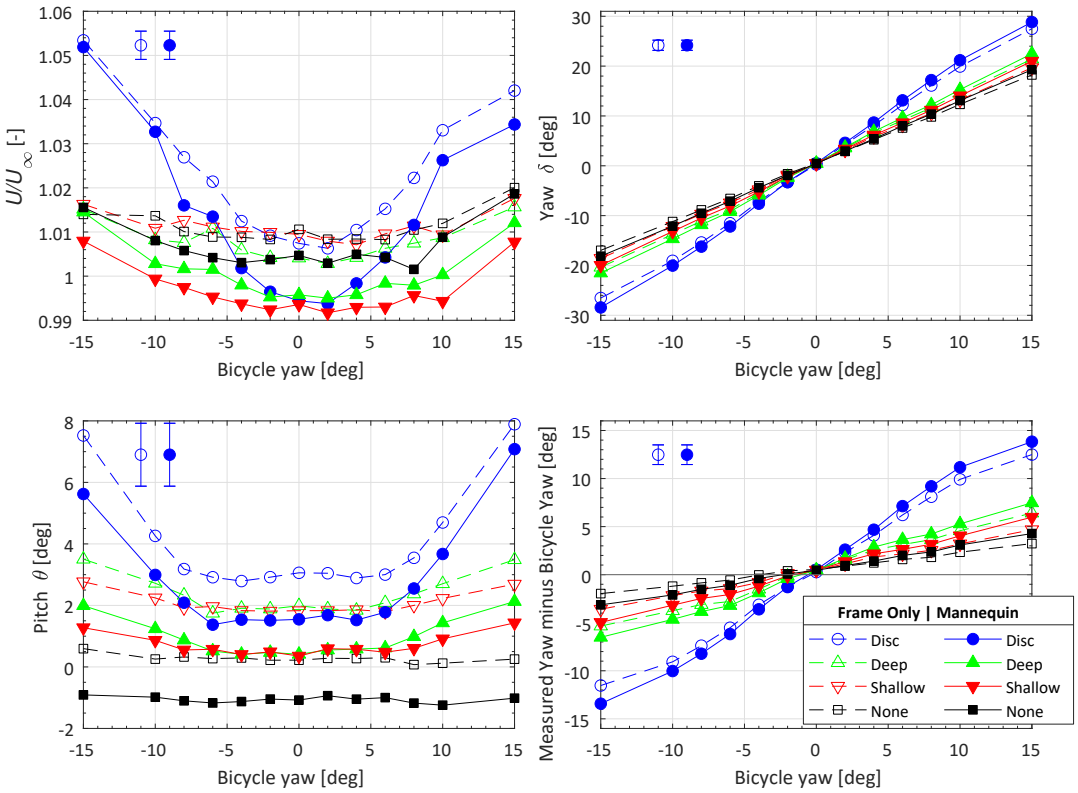


Figure 6.8 The effect of yawing the bicycle on the front probe. Here U_∞ is 15 m/s, the front wheel was rotated to match the tunnel speed and $k = 0.098$ (80 rpm). Typical errorbars for all points are shown in the top left corners.

disk wheel case.

6.3.2 Effect of yawing the bicycle (middle probe)

The effect between the rider's legs of yawing the bicycle is shown in Figure 6.9 where the influence of the pedalling legs is clearly seen when compared to the front probe. For all tests with a front wheel fitted, the front wheel was rotated to match the wind tunnel speed. When the mannequin was present, the rear wheel was rotated to produce a reduced frequency of 0.098 (80 rpm pedalling cadence). As the middle probe is on the centreline of the bicycle, it lies in the wake of the down tube and front wheel, a feature that is clearly evident when observing the total velocity component around 0° of bicycle yaw. At this position, there is a dip in the airspeed until ±4° bicycle yaw where the probe leaves the wake of the down tube and enters the free-stream flow. For the frame-only tests, the airspeed at bicycle yaw angles greater than 6°

plateaus out to equal the tunnel speed. In contrast, the mannequin tests have a notable increase in the airspeed above the tunnel speed until 15° where it drops back down to equal the tunnel speed. This increase in velocity is due to the acceleration of the flow around and between the mannequin's legs, a feature more evident at yaw angles of 4–10° where the probe lies outside of the down tube wake and inside the region of local acceleration around the legs. Beyond this, when the bicycle is at 15° of yaw, the probe is behind the influence of the legs and in the freestream, lowering the magnitude of the airflow to the tunnel speed.

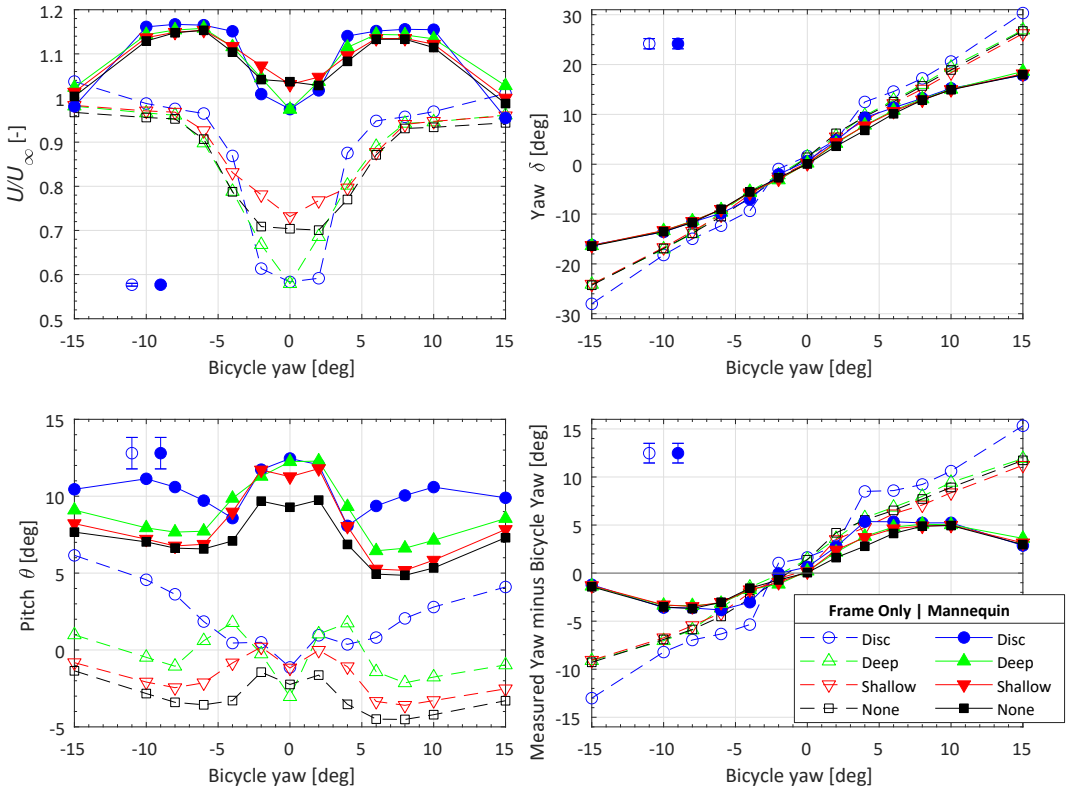


Figure 6.9 The effect of yawing the bicycle on the middle probe (P_1). Here U_∞ is 15 m/s, the front wheel was rotated to match the tunnel speed and $k = 0.098$ (80 rpm). Typical errorbars for all points are shown in the top left corners.

The aerodynamic yaw follows the same trend for all wheel conditions, indicating that the front wheel may not have as large an influence further rearwards along the bicycle as it did ahead of the bicycle. A noticeable exception is the frame-only disc wheel case which shows a greater effect than the other cases for all bicycle yaw angles higher than 4°. The measured

yaw is greater than the bicycle yaw due to the strong induced velocity of the disc wheel. The yaw angles for the frame-only and mannequin tests follow a similar pattern up to 6°, beyond which they deviate with the mannequin results being most affected by the presence of the legs which serve to minimise the aerodynamic yaw and increase the pitch angle.

There is a distinctive pitch angle present for all the mannequin tests which is likely due to an induced upwards flow from the mannequin thighs. This up-flow initially decreases with bicycle yaw until 4–6°, beyond which it starts to increase at a rate dependent on the choice of front wheel. The frame-only tests show the effects of the induced velocity from the front wheel with greater pitch angle at higher bicycle yaw angles for the disc wheel and progressively less for the two spoked wheels.

Further testing was completed with the middle Cobra probe in three different positions (see P_1, P_2, P_3 on Figures 6.4 and 6.6) and for a bicycle yaw angle of zero degrees. Figure 6.10 compares the outputs of the different investigative methods, namely the live-rider velodrome data, mannequin wind tunnel data, and the potential flow model. The wind tunnel data was obtained at a reduced frequency of 0.098 (80 rpm), the potential flow data is quasi-steady ($k = 0$), and the velodrome data was obtained at an average reduced frequency of 0.16 (110 rpm). The wind tunnel and potential flow data were both obtained at a flow speed of 15 m/s while the velodrome data was obtained with an average wheel velocity of 13.2 m/s. For the purposes of this discussion, all references to location in the crank cycle will be limited to the periodic range of $0° < \zeta < 180°$ however, due to body symmetry, results are reflected by 180° in the second half of the crank cycle.

The geometry and conditions of each data set are different and would have a substantial impact when comparing the results. The leg motion in the velodrome data set is obtained from two different live riders with differing leg geometry, whereas the leg shape of the mannequin is based on a 3D scan of a different rider with modifications at the joints to enable articulation, and the potential flow model geometry is a series of simple truncated-cones. The potential flow model has limitations in that it is two-dimensional, inviscid, and irrotational, with only a partial model of the bicycle. As such it may not capture all the effects of geometry, boundary layers, and wakes. However, the results are applicable in the primary measurement points which are outside the wakes and near-wall regions and where the flow can be considered largely irrotational and inviscid [174]. The wind tunnel flow conditions are highly controlled with low turbulence, consistent airflow, and a fixed bicycle/mannequin (albeit with a pedalling motion). This contrasts with the velodrome data which has extra influences such as the lean/rock of the bicycle,

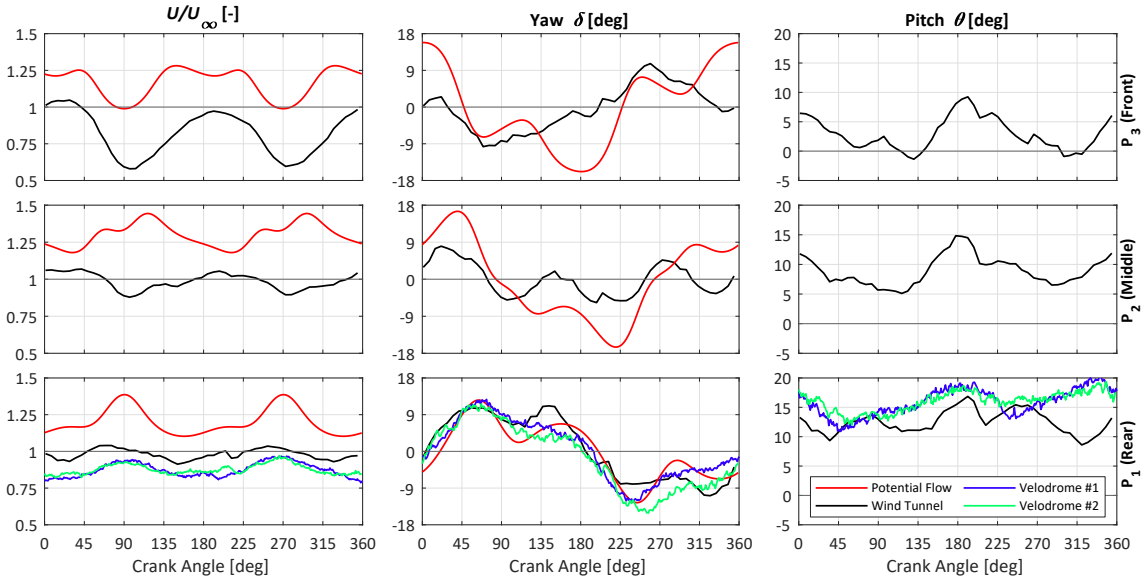


Figure 6.10 Normalised flow speed, pitch and yaw at the three measured positions (P_1, P_2, and P_3) for three different data sets and a bicycle yaw angle of 0°. The black lines are from the mannequin in the wind tunnel, red lines are the potential flow model, and the blue and green lines are velodrome data. See Figure 6.4 for a representation of the location of this data in relation to the bicycle.

a relatively inconsistent cadence, and yawed and turbulent airflow [142]. In addition, the velodrome data is an average of all cycles across several laps, combining the airflow in the bends and straights. However, as the middle probe at position P_1 is in the middle of the bicycle, it is approximately in-line with the turn radius at the centre of gravity of the bicycle/rider, so the aerodynamic effects of bends are minor. As such, there were no observable differences between the data obtained in the straights and the bends for position P_1 and the data was averaged across the entire lap.

Figure 6.10 shows that the total velocity predicted by the potential flow model is consistently greater than that of the experimental data but generally follows a similar pattern. In the potential flow model, the effects of viscosity, and hence wakes, are ignored, eliminating the velocity deficit observed in the wind tunnel experiments, causing the constant difference between the calculated and measured total speed. Additionally, the probe position is in the wake of the front wheel (not included in the model), which has an impact on the experimental results as shown earlier but would not affect any results from the model. Finally, due to the lean angle of the bicycle, the airspeed differs from the wheel speed in the bends, resulting in a lower U/U_∞ for the

velodrome data.

For the probe position P1 there is a minimum normalised speed at a crank angle of 130–150° and a maximum at 90°. This normalised speed cycle is then inverted for position P_3 with the minima corresponding to the maxima at P_1 and vice versa. The maxima in P_1 are due to the left and right legs constricting the airflow between themselves and occurs when either leg is roughly vertical. At this point, both legs are at their furthest from P_3, reducing the upstream flow acceleration from the leg position, reducing the speed at P_3 to the freestream value.

There can be seen a large variation in the yaw and pitch angles at each of the three middle probe positions across a single cadence cycle. Overall the potential flow model follows the broad trends of the experimental data, with exceptions for the yaw data for probe position P_3 at $\zeta = 0°$ and normalised velocity for position P_2 at $\zeta = 110°$, the cause of which is unknown. There is a distinctive double-peak in the yaw data for position P_1 at 60° and 150° that is seen in both the potential flow and wind tunnel data. The velodrome data does not exhibit the distinctive second peak, but does appear to flatten out at the same crank angle.

There is a large positive pitch angle present, particularly at positions P_1 and P_2, indicating that the airflow is moving upwards as it moves rearwards inside the bicycle frame triangle. This could be induced by a vortex roll-up in the near wake of each shank, with the local maxima in the pitch angle occurring when either shank is inclined furthest from vertical. When one knee is forwards, the shank is angled down and towards the rear, producing an angled bluff body that the airflow then separates over, creating a large up-flow laterally offset from its wake. In contrast, the local minima occur at the point when the shanks are most vertical. As the measurement position moves further forwards, the influence of the shank lessens and so the pitch angle becomes more neutral. There is a discrepancy between the velodrome and wind tunnel data at around 140° with a much higher pitch angle in the velodrome data. This could be due to the higher reduced frequency in the velodrome as discussed later, the different body position of the rider compared to the mannequin, or the influence of lean and curved airflow on the bends [142].

An extension of the potential flow results is presented in Figure 6.11 which shows the speed and yaw angle of the flow along a horizontal line parallel to the bicycle centreline between the down tube and seat tube. As expected, there is a slow-down of the flow anterior to the seat tube and posterior to the down tube, with the fastest flow and greatest yaw angle variation midway between the two tubes. This region of high-speed flow occurs at approximately 90° in

the crank cycle, when the two shanks are closest to each other, providing the greatest constriction and acceleration of the flow. At this position in the crank cycle, the flow experiences minimal yaw. Conversely, the greatest yaw angle occurs at approximately 0°, when the legs are furthest apart in the x-direction and the flow is turned laterally between them.

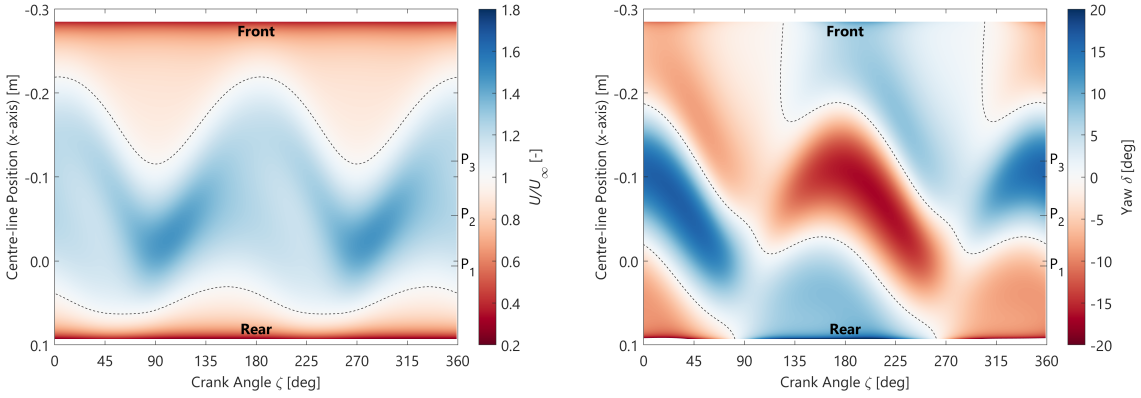


Figure 6.11 Potential flow results along a horizontal line parallel to the centreline of the bicycle at a height of 374 mm above the bottom bracket for **(a)** total velocity, **(b)** yaw angle. The probe positions are marked on the right border. The dashed lines show when $U = U_\infty$ and Yaw = 0°. See Figure 6.4 for a representation of the location of this data in the model.

The flow analysis can also be extended vertically as shown in Figure 6.12 which presents the flow calculated at a distance of 50 mm anterior to the seat tube/post for its entire height in the sagittal plane. There is a gap in the middle where the sloping top tube obstructs the flow and so the flow has not been calculated in this range. There is likely to be a point closer to the hip where the wakes from the thighs merge, making the potential flow analysis at this location inaccurate. The exact position of this is likely to vary with the crank cycle and is currently unknown. The inconsistencies marked by arrows indicate when are where the model transitions from one leg segment to the other, i.e. when the knee or ankle passes through the plane of interest. This produces a step change in the modelled flow and is an area where the model is most inaccurate due to the geometrical differences in the mannequin at the joints, which are not replicated in the model.

The data in Figure 6.12 shows that there is a variation in the yaw angle compared to the freestream across the crank cycle for the length of the seat tube/post, with a relatively small change in flow speed. The yaw angle behaviour is qualitatively confirmed by velodrome observations illustrated in Figure 6.1. The wide range of yaw angles present shows the varying direction

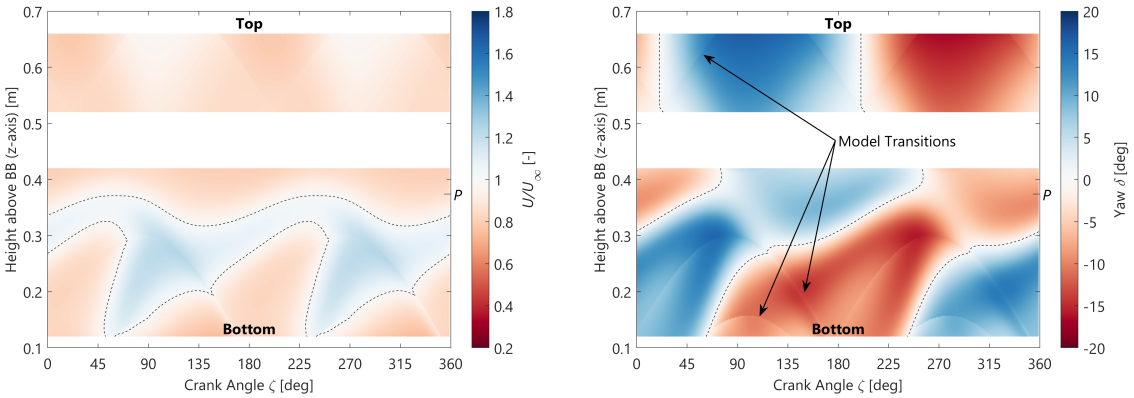


Figure 6.12 Potential flow results 50 mm anterior to the seat tube over a range of heights above the bottom bracket for **(a)** total velocity, **(b)** yaw angle. The position of the measurement plane is marked on the right border. The dashed lines show when $U = U_\infty$ and Yaw = 0°. See Figure 6.4 for a representation of the location of this data in the model.

of the airflow incident on the seat tube/post and must be considered in the design for localised aerodynamic development of bicycle frames.

6.3.3 Effect of the reduced frequency

An investigation into the quasi-steady nature of the airflow around the legs was conducted through static and dynamic mannequin testing in the wind tunnel. Testing was completed with the bicycle at zero degrees of yaw, a wind tunnel speed of 15 m/s, and the probe at position P_1 whilst using the pedalling mannequin. Static testing was completed by manually moving the mannequin through crank angles from 0° to 360° in 15° increments. The influence of dynamically increasing the reduced frequency of pedalling was measured through two separate tests where the mannequin cadence and freestream velocity were independently varied. Firstly, cadence testing was conducted by pedalling the mannequin at fixed cadence frequencies of 10–100 rpm in 10 rpm increments with a constant wind speed of 15 m/s Secondly, freestream velocity testing was completed by decreasing the wind tunnel speed in 2 m/s increments whilst maintaining a constant cadence of 80 rpm.

At each step, data was recorded for 45 s, binned according to the crank angle, and averaged over all complete cycles. Similar studies by Crouch et al. [49], Chan [170] and others who measured the wake during dynamic leg motion were required to infer the crank angle for each phase-averaged velocity field based on an estimated convection velocity of the wake pattern. This was

not done in the present case due to the probe position between the legs and so the flow velocity was directly measured at each crank angle, eliminating one uncertainty associated with dynamic testing.

The results shown in Figure 6.13 establish that the dynamic data for the yaw angle largely follows the static data through all measured reduced frequencies. However, there is a clear step change between the static case and all dynamic changes, particularly in the normalised velocity where the static data is much greater in magnitude than the dynamic data for ≈135–225°. This also corresponds to the introduction of a phase-shift of approximately 45–60°. This largely occurs instantly between the static case the case with the lowest reduced frequency, with only a minor increase in the phase shift and magnitude at higher cadences. Similarly, the effect of increasing the reduced frequency is to increase the pitch-angle magnitude and phase-shift the pattern to later in the crank cycle, evident in both the cadence and wind speed testing. The results collectively demonstrate a reduced frequency dependence for the flow influenced by the mannequin's shins. It is noted that the motion of the shanks during each pedalling cycle comprises both a fore-aft oscillation and a pitching rotation, and parts of this motion resemble that of a missile-like cylinder undergoing a pitching motion. A reduced frequency dependence for one such flow has been observed before in Smith and Nunn [175] where a cylinder of 15:1 aspect ratio, operating at a similar Reynolds number, was rotated at the same reduced frequencies as the angular rotation of the shanks in the present experiments, leading to an approximately 25 % increase in normal force when compared to the static case.

6.4 General discussion

The analysis of the flow at the front probe with a varied bicycle yaw angle is useful to help explain the extensive yaw observed in Fitzgerald et al. [142] when a cyclist is riding on a velodrome bend. The effect of the front wheels and rider/bicycle is to amplify the yaw present from cornering as recorded by the aerodynamic probe. For the case of the disc front wheel, the yaw angle at the front of the bicycle was found to double at the location of the probe. This may have implications on the aerodynamic efficiency of current bicycle designs.

For the dynamic (moving legs) data, there were four different experimental and analytical methods used. Firstly, a basic flow visualisation technique was used to qualitatively observe the flow between a rider's legs. This led to on-track experimental data being obtained with an instrumented bicycle and a live rider inside a velodrome. Thirdly, controlled experiments

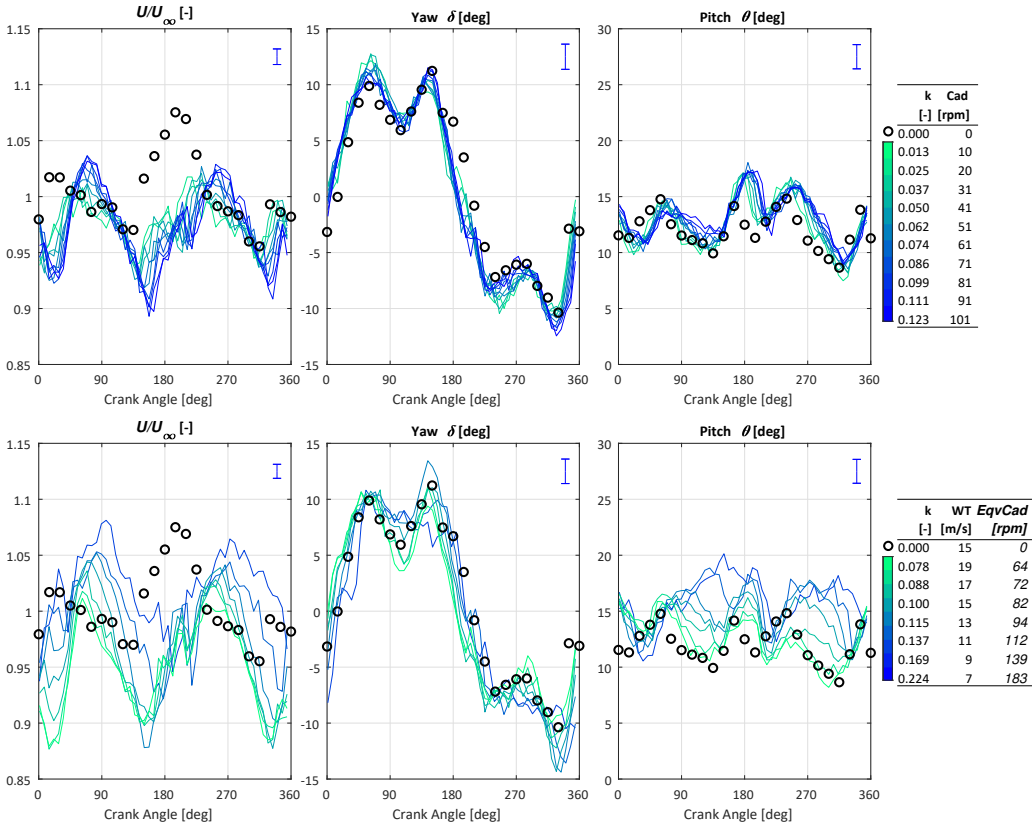


Figure 6.13 Measuring the effects of reduced frequency at probe position P_1 between the mannequin legs. The circular dots indicate the static case and the green-blue shaded lines indicates increasing unsteadiness. The top row shows the effect of varying the pedal cadence whilst maintaining a constant tunnel speed of 15 m/s and the bottom row shows the effect of decreasing tunnel speed whilst maintaining a constant cadence of 80 rpm. The reduced frequency k, and a corresponding equivalent cadence at 15 m/s are shown in the legend. Typical error bars are shown in the top righthand corners.

were undertaken using the same bicycle in a wind tunnel with a pedalling mannequin. Finally, an analytical method using potential flow theory and simplified leg and bicycle geometry was developed and analysed. Each has different geometries, flow conditions and errors, but all agree qualitatively and quantitatively regarding the effects of pedalling on the flow around the bicycle and rider.

The potential flow model was designed as a quick method of validating the experimental data and as a way to experiment with different leg geometries. Caution must be taken when interpreting the results due to their inherent limitations, namely that the leg/bicycle model is a substantial simplification, and the flow is two-dimensional, inviscid and irrotational. As such the leg

shape is an approximation, there are no wakes, and the flow is faster than in reality. Whilst there is a reasonable agreement with the experimental results, this has only been validated at three specific points on a single plane and it can differ at different locations as well as different periods in the crank cycle. However, the inviscid model is useful in that it highlights the probable yaw angle variation versus height along the seat tube and post and demonstrates the variation in phase versus height. Data reported in Figure 6.10 confirms that at location P_1, closest to the seat tube, the correspondence between the velodrome, wind tunnel and potential flow model is strongest, especially for the yaw data. This provides a partial validation of the data presented in Figures 6.11 and 6.12, particularly in relation to the flow beneath the bicycle's top tube. Also note that pitch angles of 10–15° are present at position P_1. Given the 17° rearward lean of the seat tube, this implies that the flow impinges on the seat tube near probe position P_1 at an angle of 25–30° to the normal. Combined with the broad yaw angles (±15°) that are measured at position P_1, the flow field is very complex.

The wide variation in flow conditions inside the primary bicycle frame triangle, as indicated by the above results, demonstrates the need to consider the specific flow conditions around the middle of the bicycle, which can differ significantly from that at the front or rear. This is useful for bicycle design where a segmented approach can be taken, with differing components designed for the differing flow conditions observed. The range of yaw angles could also be used to create a yaw-weighted coefficient of drag [141] for detailed development of the seat tube.

6.5 Conclusion

The airflow anterior to a track bicycle is measured using an instrumented bicycle in a wind tunnel and on a velodrome track and the results are compared to earlier study. The results show that the front wheel has a significant effect on the flow measured anterior to a yawed bicycle with disc wheels creating a considerable induced flow and amplifying the measured aerodynamic yaw.

In addition, the airflow between a rider's legs is modelled with potential flow and compared to experimental data obtained using a mannequin in a wind tunnel and a live rider in a velodrome. The results show a reasonable agreement between the potential flow model and both the wind tunnel and velodrome data, which is particularly remarkable considering the substantial differences between each method of data collection and the inherent assumptions in the potential flow model. The results show a large

variation in the airflow compared to the freestream due to the motion of the rider/mannequin legs. The influence of cadence on the yaw behaviour within the frame triangle appears to be minimal, but the mannequin-based tests indicate a strong effect of reduced frequency on both the pitch and speed variations which have not been identified in previous research.

6.6 Supplementary material

Supplementary videos for this chapter can be found online at 10.1016/j.jweia.2020.104374. The first video shows experimental testing with the wool tuft between a riders legs around the velodrome. The second video shows all the experimental and potential flow data collated as a single video for all 360° of a pedal cycle.

— Chapter 7 —

Conclusions

Essentially, most of this thesis has been driven by a need to understand the data observed by the front velocity probe on the instrumented bicycle when in a corner (Figure 3.7). A first look at this data was produced in the early stages of the research and this ultimately guided the later research direction. The mathematical theory for yaw and pitch angles on a bend developed in Chapter 3 under-predicted the measured data (by a particularly large margin for yaw) and so further research was required to understand the discrepancy. Part of this research involved the development of a more complete understanding of the motion of a cyclist throughout a lap. Calculations of roll angle, steering angle, wheel speed and relative airflow all require an accurate value of turn curvature at all points on the track. This led to the development of the velodrome geometry model in Chapter 4 to facilitate calculations and understand the differences between track geometries. A desire to better understand the flow with other riders present, a need to measure steering angles, and to validate roll angle calculations, led to the experimental work described in Chapter 5. Finally, to better explain the flow around the front wheel as measured by the Cobra probe, wind tunnel testing was completed with a pedalling mannequin, as discussed in Chapter 6. To extend this work from just the one probe position, the flow midway through the bicycle was analysed and the influence of a cyclist's pedalling legs was documented in Chapter 6.

Both the yaw/pitch aerodynamic theory developed in Chapter 3 and the steering angle calculations used in Chapter 5 require an accurate measure of the bicycle roll angle. As detailed in Chapters 2 and 4, the quasi-steady-state equation for roll angle was well known, but it has been of limited realistic use for track cycling due to the requirement of knowing the turn radius at all points around the track. The development of an accurate velodrome geometry model based on simple measurements, outlined in Chapter 4, provides a

method of calculating a continuous roll angle around a complete lap. The validity of using the quasi-steady-state roll angle calculation with the track model was confirmed in Chapter 5 where the measured and calculated lean angles closely aligned. The track model developed here can be used in general track cycling analytic models to improve their accuracy via more accurate estimation of a cyclist's roll angle and velocity of the centre of gravity.

A steering angle sensor was developed and theoretical steering angle calculations used to help understand the aerodynamic influence of the front wheel in the bends. A model of the bend transitions from Chapter 4 enabled the steering angle calculations and extended the cornering yaw/pitch theory developed in Chapter 3. Results in Chapter 5 showed a steering angle of approximately 2° in the bends, matching theoretical calculations from the literature.

The wind tunnel wheel testing, detailed in Chapter 6, show that the front disc wheel creates a considerable induced flow, increasing the relative speed and aerodynamic yaw angle as measured by the probe. The speed of this induced flow is proportional to the yaw angle of the flow incident on the front wheel. In a velodrome, away from other riders, the angle of this incident flow is dependent upon the bicycle roll angle, heading angle, steering angle, and cornering airflow. These observations qualitatively explain the large aerodynamic yaw angles measured on a velodrome bend in Chapter 3. A quantitative explanation of the yaw angle observations would require further investigations of the aerodynamic effects of steering angle at a range of bicycle yaw (heading) angles.

To summarise the steady-state flow on a 21.5 m turn-radius bend at a speed of 14 m/s; a cyclist will lean at 42°, which creates a theoretical aerodynamic yaw angle of 1.8°, an aerodynamic pitch angle of −1.6° and a steering input angle of 2.0° to the left. The combination of steady-state curved airflow and steering angle creates a wheel yaw angle of ≈0° relative to the incoming wind. However, in addition to the steering angle, the bicycle will be at a heading angle of 1.0° to the right of the velocity of the centre of gravity. This is due to the steering and slip angles of a single-track vehicle and is determined in the steering calculations performed with the instrumented bicycle in Chapter 5. The combination of heading angle and steering angle will influence the relative airflow at the front end of the bicycle in a corner. Further work could involve a more complete bicycle dynamics model to provide more accuracy in the heading and steering calculations. In addition, further testing could be completed with the instrumented bicycle and mannequin in a wind tunnel. This would involve setting the bicycle at an aerodynamic yaw angle, but with the front wheel parallel to the flow, enabling observations of the

simultaneous influence of the cyclist's body at yaw angle and the front wheel at zero-yaw.

On top of the lap-based cornering data, there are cadence effects. A cyclist will rock the bicycle left/right each pedal cycle which creates a back-and-forth yawed airflow. Additionally, the cyclist will steer the bicycle approximately ±1.5° within a pedal cycle which changes the incident flow on the front wheel, inducing a fluctuating flow angle. The combination of these two rock/weave factors creates a substantial change in the flow across each pedal cycle, creating the cadence-frequency oscillation in airflow observed in Chapter 3. It would also increase the cyclist's rolling resistance by increasing wheel scrubbing.

In addition to the lap position and cadence effects, there is a third effect due to the random turbulence of the flow inside a velodrome. This is of a much smaller timescale and magnitude than the previous two factors. The scale and intensity of this turbulence is dependant on the number and location of any other riders on the track. The rider experiences the minimum incident turbulence when riding alone in a velodrome and the maximum when closest to other riders, as seen for a team pursuit in Chapter 3. Chapter 5 shows that there is an increase in the freestream turbulence when the other riders are half a lap ahead of the instrumented bicycle. As discussed in Chapters 2 and 5, this freestream turbulence has the potential to influence the effectiveness of drag reduction systems currently in use.

Along with the velocity measurements using the front probe, an investigation into the flow around the middle of the frame was conducted to further study flow in the bends and to observe the influence of pedalling cadence. The results showed that the bends had a negligible influence when the probe was positioned close to bicycle/rider centre of gravity. This is as expected as the distance L_P from Equations (3.2) and (3.3) is close to zero, indicating that the relative airflow is close to a direct headwind. However, the influence of the movement and position of the legs had a large impact on the flow through the middle of the frame.

To corroborate and expand the results, a potential flow model of the pedalling legs was completed. This provides a quick and simple method of understanding the flow through the middle of the frame and onto the bicycle's seat tube. The data at P_1 (Chapter 6), located 50 mm in front of the seat tube, demonstrates reasonable agreement with the potential flow model and shows that the model can be extended further up the seat tube and seat post. However, care must be taken with the model and an understanding of the limitations is required if extension into experimentally-unvalidated areas is desired.

The consistent results shown by the live rider in a velodrome, a pedalling mannequin in a wind tunnel, and potential flow calculations, show that the local flow at the middle position is dominated by the movement and position of the legs, rather than the overall flow around the bicycle. It also helps to improve the reliability of each individual testing method.

7.1 Recommendations for future work

A primary area for future research would be to further analyse the effects of turbulence as measured inside a velodrome and then replicate those measurements in either a wind tunnel or through CFD. This would enable a researcher to have an experimental setup that better matches the real-world conditions experienced by a track cyclist. As discussed in Chapters 2 and 5, freestream turbulence can influence the flow around a cyclist, particularly the laminar-to-turbulent boundary layer transition. As manipulation of the drag crisis is a primary method of drag reduction for cycling, any feature which could have a significant influence on this drag crisis needs a detailed investigation. There is the potential for further drag reduction gains through an understanding of how particular skinsuits or bicycles function in a turbulent environment.

Whilst the primary focus of this project is on indoor track cycling, the research into turbulence would also be of relevance to outdoor road cycling. An instrumented bicycle, similar to that used in this project, could be developed to investigate the airflow on the road. The aerodynamic environment in road cycling has much greater variance than it does in indoor track cycling. Influences such as natural wind, temperature, hot road surfaces, artificial and natural built environments, and auxiliary race vehicles, would all alter the freestream turbulence experienced by a race cyclist. It is likely that the turbulence intensity would be greater and the length scales shorter due to increased turbulence generation and greater mixing. However, the primary difference may be that outdoor cycling racing would produce a far greater range of aerodynamic environments than seen for indoor track cycling.

The velodrome model developed in Chapter 4 that includes transition curves could be used to help improve the accuracy of track cycling analytic models that have been developed by others. One of the possible reasons that the analysis by Fitton and Symons [12] is more accurate than previous track cycling models could be due to the increased accuracy of their track modelling compared to previous work which had no transition curves. However, the geometry they used was not made freely available for other researchers. In contrast, the model in Chapter 4 is able to be adapted for any velodrome and

could be included in existing models, potentially increasing their accuracy. It could also be used to take performance data from one velodrome and model how well an athlete would perform at another velodrome.

Further research into the variation in power around a bend could also be an area of interest. From the work of Chapters 4 and 5, it is unclear exactly what the influence of roll and roll-rate have on the change in power, particularly regarding changes in potential energy. A more detailed look into the effect of the bend transition on the roll-rate could provide further details on the corresponding decrease in power observed in the bends. This could then be used to increase the accuracy of track cycling models and better replicate the velodrome environment in the lab.

The work outlined in Chapter 6 shows that there can be extensive differences in the aerodynamic environment around different components of the bicycle frame. An understanding of the highly fluctuating flow measured anterior to the seat tube can be used to develop low-drag bicycle frame components that are specifically designed for that flow environment. Typical bicycle frame components are often based on a thick, symmetrical NACA aerofoil profile that will stall at an angle of attack less than 15° [176], below the maximum yaw angle observed in Chapter 6. This stall would cause an increase in the aerodynamic drag as well as a fluctuating drag force. Future work could involve different tube profiles that are specifically designed for the fluctuating airflow behind the legs.

Whilst there has been considerable research and development into bicycle aerodynamics to date, it is clear that there are still areas where future work is required. However, to provide any more than a marginal gain in drag reduction a step change in our understanding and appreciation of the flow environment is required.

— Appendix A —

An additional turn curvature equation

This appendix develops an extra curvature function that can be used in the velodrome geometry model outlined in Chapter 4. This function can have any chosen level of geometric continuity $\geq G^2$, only limited by the increasing transition length with increasing continuity. The advantage of this equation is that it can provide high levels of continuity for when considerations of higher derivatives of motion are desired. However, higher levels of continuity can have higher jerk and provide diminishing returns after G^4.

A.1 Derivation

A transition curve profile with G^k curvature can be provided by a polynomial of the form

$$K(\tau) = \frac{1}{RL_T^{k-1}}\left(\frac{C_1}{L_T^{k-2}}\tau^p + \frac{C_2}{L_T^{k-3}}\tau^{p-1} + \frac{C_3}{L_T^{k-4}}\tau^{p-2} + \cdots + C_{k-1}\tau^{k-1}\right) \tag{A.1}$$

where k is the desired level of geometric continuity, $p = 2k-3$ is the polynomial order, and C_i are numerical coefficients. Connecting the curvature at either end of the transition requires that $K(0) = 0$ and $K(\tau_1) = 1/R$, which gives

$$\sum_{i=1}^{k-1} C_i = 1. \tag{A.2}$$

Secondly, G^k continuity requires that the first $k-2$ derivatives of curvature have endpoints $\frac{\mathrm{d}^j K}{\mathrm{d}s^j}(0) = 0$ and $\frac{\mathrm{d}^j K}{\mathrm{d}s^j}(\tau_1) = 0$. Then, for all $\{j \in \mathbb{Z} \mid 1 \leq j \leq k-2\}$,

$$\sum_{i=1}^{k-1} C_i D_{i,j} = 0, \tag{A.3}$$

where $D_{i,j}$ is the coefficient from taking the j^{th} derivative of the i^{th} polynomial term. Using Equations (A.2) and (A.3), the values of the coefficients C_i can be obtained by solving the set of simultaneous equations given by

$$\mathbf{AC} = \mathbf{B} \tag{A.4}$$

where

$$\mathbf{A} = (p\mathbf{J}_{k-1,k-1} - \mathbf{J}_{k-1,1}\mathbf{N})! \oslash \left(p\mathbf{J}_{k-1,k-1} - \mathbf{J}_{k-1,1}\mathbf{N} - \mathbf{N}^T\mathbf{J}_{1,k-1}\right)!. \tag{A.5}$$

Here, $\mathbf{N} = [0,1,\ldots,k-2]$, $\mathbf{J}_{m,n}$ is an $m \times n$ matrix of ones, $\oslash$ represents element-wise division and the factorial is also taken element-wise. The two additional vectors are $\mathbf{B} = [1,0,\ldots,0]^T$ and $\mathbf{C} = [C_1, C_2, \ldots, C_{k-1}]^T$. To better show Equation (A.4), it can be expanded to its complete form with

$$\begin{bmatrix} 1 & 1 & 1 & \cdots & 1 \\ p & p-1 & p-2 & \cdots & p-k+2 \\ \frac{p!}{(p-2)!} & \frac{(p-1)!}{(p-3)!} & \frac{(p-2)!}{(p-4)!} & \cdots & \frac{(p-k+2)!}{(p-k)!} \\ \vdots & \vdots & \vdots & \ddots & \vdots \\ \frac{p!}{(p-k+2)!} & \frac{(p-1)!}{(p-k+1)!} & \frac{(p-2)!}{(p-k)!} & \cdots & \frac{(p-k+2)!}{(p-2k+4)!} \end{bmatrix} \begin{bmatrix} C_1 \\ C_2 \\ C_3 \\ \vdots \\ C_{k-1} \end{bmatrix} = \begin{bmatrix} 1 \\ 0 \\ 0 \\ \vdots \\ 0 \end{bmatrix}. \tag{A.6}$$

Equation (A.4) can be solved for the polynomial coefficients C_i and then Equation (A.1) can be used to calculate the transition curvature equation, in place of either Equation (4.17) or (4.18).

A.2 Results

From Equation (A.1), the first six curvature functions are

$$K(\tau) = \frac{\tau}{RL_T}, \tag{A.7}$$

$$K(\tau) = \frac{1}{RL_T^2}\left(-\frac{2}{L_T}\tau^3 + 3\tau^2\right), \tag{A.8}$$

$$K(\tau) = \frac{1}{RL_T^3}\left(\frac{6}{L_T^2}\tau^5 - \frac{15}{L_T}\tau^4 + 10\tau^3\right), \tag{A.9}$$

$$K(\tau) = \frac{1}{RL_T^4}\left(-\frac{20}{L_T^3}\tau^7 + \frac{70}{L_T^2}\tau^6 - \frac{84}{L_T}\tau^5 + 35\tau^4\right), \tag{A.10}$$

$$K(\tau) = \frac{1}{RL_T^5}\left(\frac{70}{L_T^4}\tau^9 - \frac{315}{L_T^3}\tau^8 + \frac{540}{L_T^2}\tau^7 - \frac{420}{L_T}\tau^6 + 126\tau^5\right), \tag{A.11}$$

$$K(\tau) = \frac{1}{RL_T^6}\left(-\frac{252}{L_T^5}\tau^{11} + \frac{1386}{L_T^4}\tau^{10} - \frac{3080}{L_T^3}\tau^9 + \frac{3465}{L_T^2}\tau^8 - \frac{1980}{L_T}\tau^7 + 462\tau^6\right), \tag{A.12}$$

which have G^2, G^3, G^4, G^5, G^6 and G^7 continuity respectively. These equations have been previously developed separately in the literature, where Equation (A.7) is the standard clothoid curve, Equation (A.8) is known as a Bloss curve [177], and Equation (A.9) has been previously shown by Watorek [178]. Equations (A.10) and (A.11) are shown by Schuhr [179], but their method of derivation are not outlined. It is believed that Equation (A.12) and any higher polynomial orders are not shown elsewhere. The method outlined here demonstrates how the separate transition curves developed by other researchers come from the same origin and expands and generalises the existing work. It is a relatively simple extension to add Equation (A.1) to the Matlab function included in Section 4.6, providing a series of transition curve options with greater continuity.

The curvature of Equation (A.1) and its first three derivatives is shown in Figure A.1 for continuity levels from G^2 to G^9. This demonstrates the discontinuities which begin to appear at curves with lower continuity. Of note is that higher levels of continuity have a higher peak in the first derivative, leading to higher jerk in the middle of the transition, which is the trade-off for increased continuity.

The limiting factor of Equation (A.1) is the increasing transition length required for higher geometric continuity, shown in Table A.1. This greatly limits the range of Y and R inputs that can produce valid results, shown in Figure A.2.

A summary of all the proposed transition curve functions and their first two normalised derivatives is provided in Figure A.3. The maximum and minimum values of the two derivatives have been annotated as they can dictate the jerk experienced in a transition.

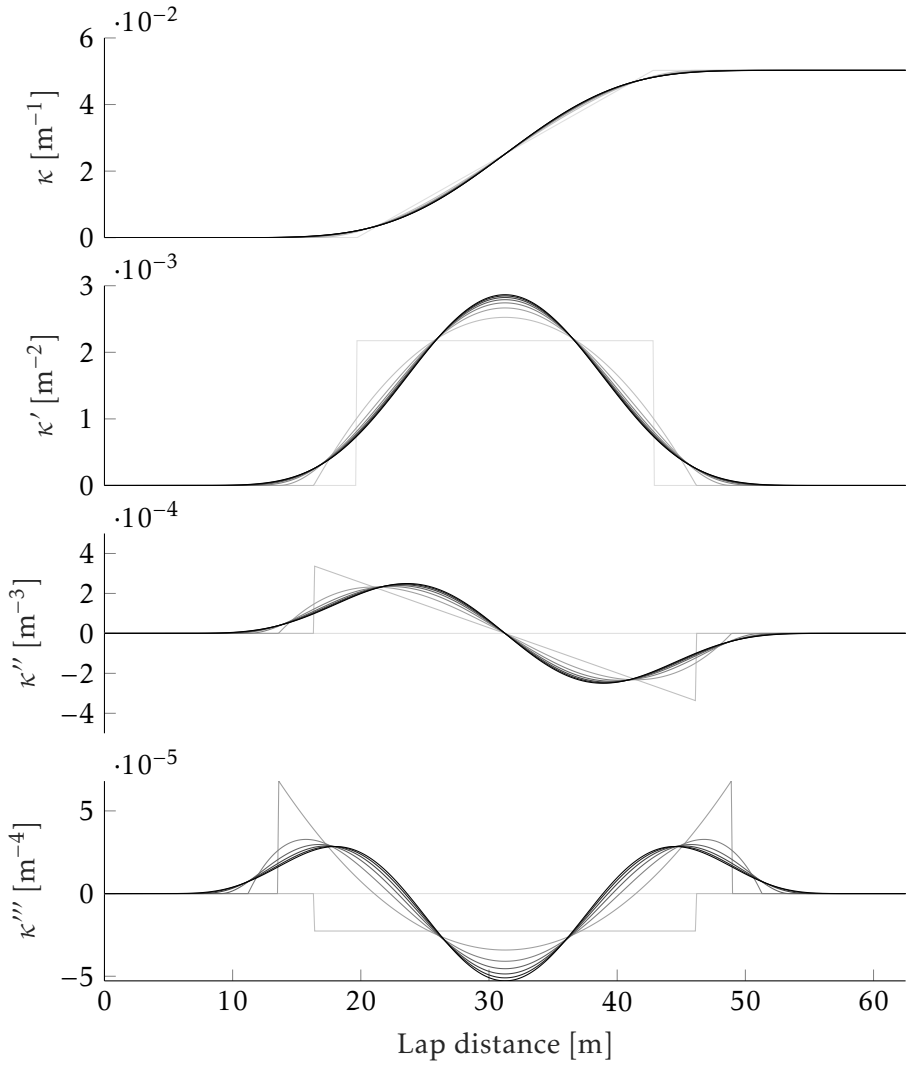


Figure A.1 The effect of Equation (A.1) on the curvature and its first three derivatives along one quarter of the track with $Y = 23\,\text{m}$, $R = 22\,\text{m}$ and $L_L = 250\,\text{m}$. Darker shades indicate increasing levels of geometric continuity from G^2 to G^9.

Table A.1 The straight (L_S), bend (L_B), and transition lengths (L_T) for Equation (A.1) with increasing levels of continuity. Inputs are $Y = 23\,\text{m}$, $R = 22\,\text{m}$, and $L_L = 250\,\text{m}$.

Continuity	L_S [m]	L_B [m]	L_T [m]
G^2	16.40	23.01	23.09
G^3	13.03	19.64	29.83
G^4	10.29	16.91	35.30
G^5	7.92	14.54	40.04
G^6	5.81	12.42	44.27
G^7	3.88	10.49	48.13
G^8	2.09	8.70	51.71
G^9	0.42	7.03	55.05

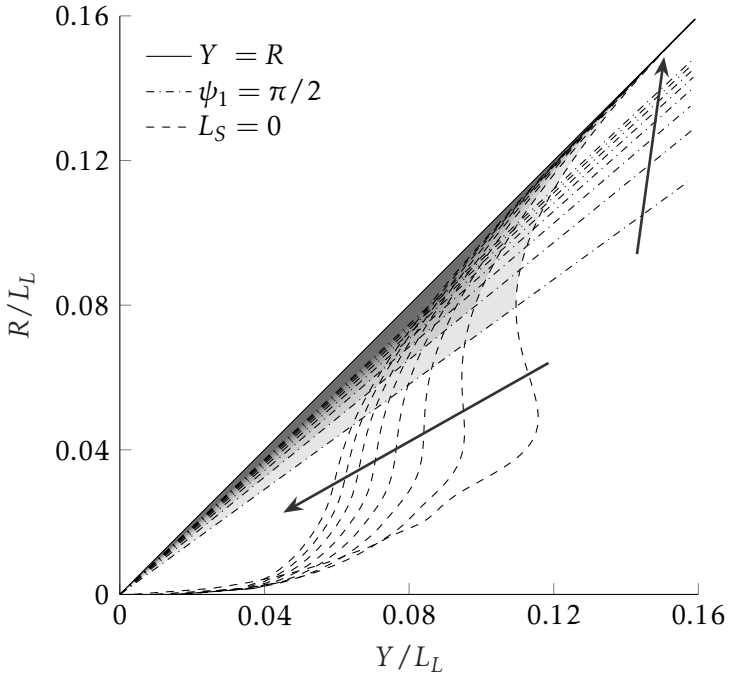


Figure A.2 Parameter space of Equation (A.1) where the shaded area indicates the limits of normalised inputs Y and R. The arrows indicates increasing levels of geometric continuity from G^2 to G^9. The dashed-dotted lines indicate limits due to Equation (4.15), whilst the dashed lines indicate limits due to Equation (4.16).

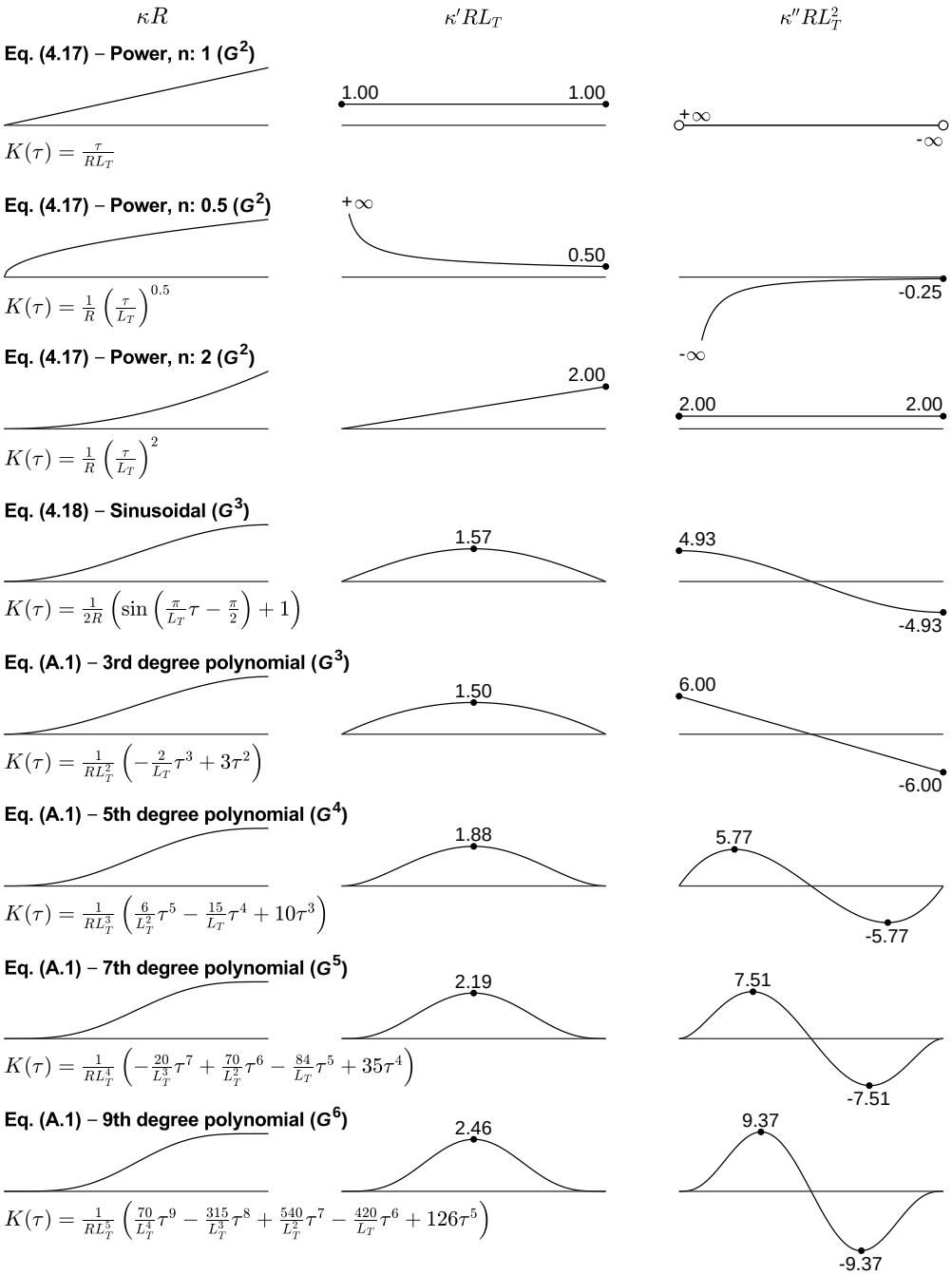


Figure A.3 A summary of all used transition curve equations and their first two derivatives. The x-axis is the normalised transition length and the y-axis has been normalised by the end radius and transition length.

References

[1] Kyle, C. R. and Burke, E. R. (1984) 'Improving the racing bicycle' *Mechanical Engineering*, 106(9), 34–45 (see pp. 1, 25, 34, 97).

[2] Gibson, C. B. (2021) *CBG Photo*. URL: https://www.cbgphoto.com/ accessed: 04/11/2021 (see p. 2).

[3] Union Cycliste Internationale (2021) *Clarification guide of the UCI Technical Regulation. Version 17.01.2021*. URL: https://www.uci.org/inside-uci/constitutions-regulations/regulations (see p. 2).

[4] Union Cycliste Internationale (2020) *UCI Cycling Regulations: Part III: Track Races. Version 12.06.2020*. URL: https://www.uci.org/inside-uci/constitutions-regulations/regulations (see pp. 2, 28, 58, 74, 80).

[5] Olds, T. S., Norton, K. I. and Craig, N. P. (1993) 'Mathematical model of cycling performance' *Journal of Applied Physiology*, 75(2), 730–7. DOI: 10.1152/jappl.1993.75.2.730 (see p. 5).

[6] Lukes, R., Carre, M. and Haake, S. (2006) 'Track Cycling: An Analytical Model' *The Engineering of Sport 6*, 115–120. DOI: 10.1007/978-0-387-46050-5_21 (see pp. 5, 11, 58, 67, 70, 72, 78).

[7] Martin, J., Gardner, A. S., Barras, M. and Martin, D. (2006) 'Modeling Sprint Cycling Using Field-Derived Parameters and Forward Integration' *Medicine and Science in Sports and Exercise*, 38(3), 592–7. DOI: 10.1249/01.mss.0000193560.34022.04 (see pp. 5, 11, 12, 25, 27, 58, 72, 89).

[8] Underwood, L. and Jermy, M. (2010) 'Mathematical model of track cycling: the individual pursuit' *Procedia Engineering*, 2(2), 3217–3222.

DOI: 10.1016/j.proeng.2010.04.135 (see pp. 5, 11, 27, 58, 67, 72, 78).

[9] Lukes, R., Hart, J. and Haake, S. (2012) 'An analytical model for track cycling' *Proceedings of the Institution of Mechanical Engineers, Part P: Journal of Sports Engineering and Technology*, 226(2), 143–151. DOI: 10.1177/1754337111433242 (see pp. 5, 9–12, 17, 27, 35, 58, 66, 72, 78, 79, 89, 90).

[10] Underwood, L. and Jermy, M. (2014) 'Determining optimal pacing strategy for the track cycling individual pursuit event with a fixed energy mathematical model' *Sports Engineering*, 17(4), 183–196. DOI: 10.1007/s12283-014-0153-3 (see pp. 5, 7, 8, 10–12, 17, 25–27, 57, 58, 64, 67, 70, 72, 79, 81, 89, 90).

[11] Caddy, O., Fitton, W., Symons, D., Purnell, A. and Gordon, D. (2017) 'The effects of forward rotation of posture on computer-simulated 4-km track cycling: Implications of Union Cycliste Internationale rule 1.3.013' *Proceedings of the Institution of Mechanical Engineers, Part P: Journal of Sports Engineering and Technology*, 231(1), 3–13. DOI: 10.1177/1754337115619306 (see pp. 5, 8, 10–12, 17, 25–27, 35, 57, 58, 64, 67, 70, 72, 78, 79, 81, 89, 90, 102).

[12] Fitton, B. and Symons, D. (2018) 'A mathematical model for simulating cycling: applied to track cycling' *Sports Engineering*, 21(4), 409–418. DOI: 10.1007/s12283-018-0283-0 (see pp. 5, 8, 10–13, 17, 27–29, 39, 57, 58, 64, 66, 72, 78–81, 85, 89, 90, 94, 127).

[13] Martin, J., Milliken, D., Cobb, J., McFadden, K. and Coggan, A. (1998) 'Validation of a Mathematical Model for Road Cycling Power' *Journal of Applied Biomechanics*, 14(3), 276–291. DOI: 10.1123/jab.14.3.276 (see pp. 5–7, 11, 23, 66).

[14] Olds, T. (2001) 'Modelling Human Locomotion' *Sports Medicine*, 31(7), 497–509. DOI: 10.2165/00007256-200131070-00005 (see p. 5).

[15] Kyle, C. R. (1979) 'Reduction of Wind Resistance and Power Output of Racing Cyclists and Runners Travelling in Groups' *Ergonomics*, 22(4), 387–397. DOI: 10.1080/00140137908924623 (see p. 6).

[16] Jeukendrup, A. E. and Martin, J. (2001) 'Improving Cycling Performance: How Should We Spend Our Time and Money' *Sports Medicine*, 31(7), 559–569. DOI: 10.2165/00007256-200131070-00009 (see pp. 6, 23).

[17] Atkinson, G., Peacock, O. and Passfield, L. (2007) 'Variable versus constant power strategies during cycling time-trials: Prediction of time savings using an up-to-date mathematical model' *Journal of Sports Sciences*, 25(9), 1001–1009. DOI: 10.1080/02640410600944709 (see p. 6).

[18] Dahmen, T., Byshko, R., Saupe, D., Roder, M. and Mantler, S. (2011) 'Validation of a model and a simulator for road cycling on real tracks' *Sports Engineering*, 14(2), 95–110. DOI: 10.1007/s12283-011-0076-1 (see p. 6).

[19] Roa, S. D. and Muñoz, L. E. (2017) 'Bicycle change strategy for uphill time-trial races' *Proceedings of the Institution of Mechanical Engineers, Part P: Journal of Sports Engineering and Technology*, 231(3), 207–219. DOI: 10.1177/1754337117724310 (see p. 6).

[20] Sundström, D. and Bäckström, M. (2017) 'Optimization of pacing strategies for variable wind conditions in road cycling' *Proceedings of the Institution of Mechanical Engineers, Part P: Journal of Sports Engineering and Technology*, 231(3), 184–199. DOI: 10.1177/1754337117700550 (see p. 6).

[21] Wolf, S., Biral, F. and Saupe, D. (2019) 'Adaptive feedback system for optimal pacing strategies in road cycling' *Sports Engineering*, 22, 6. DOI: 10.1007/s12283-019-0294-5 (see p. 6).

[22] Blocken, B., Malizia, F., van Druenen, T. and Gillmeier, S. (2020) 'Aerodynamic benefits for a cyclist by drafting behind a motorcycle' *Sports Engineering*, 23, 19. DOI: 10.1007/s12283-020-00332-z (see pp. 6, 20, 21, 80).

[23] Malizia, F. and Blocken, B. (2020) 'Bicycle aerodynamics: History, state-of-the-art and future perspectives' *Journal of Wind Engineering and Industrial Aerodynamics*, 200, 104134. DOI: 10.1016/j.jweia.2020.104134 (see pp. 6, 91, 97).

[24] Polanco, A., Roa, S., Suárez, D. R., López, O. and Muñoz, L. (2021) 'Influence of wind speed and road grade on the estimation of drag area in cycling' *Sports Biomechanics*, 1–19. DOI: 10.1080/14763141.2020.1837925 (see p. 6).

[25] Spoelstra, A., Hirsch, M., Sciacchitano, A. and Scarano, F. (2021) 'Uncertainty assessment of the Ring of Fire concept for on-site

aerodynamic drag evaluation' *Measurement Science and Technology*, 32(4), 044004. DOI: 10.1088/1361-6501/abb50d (see pp. 6, 26, 90).

[26] Danh, K., Mai, L., Poland, J. and Jenkins, C. (1991) 'Frictional resistance in bicycle wheel bearings' *Cycling Science*, 3(3), 28–32 (see pp. 6, 7).

[27] Wilson, D. G. (2004) *Bicycling Science*. 3rd ed. USA: MIT Press (see pp. 7, 11).

[28] Timoshenko, S. and Young, D. H. (1948) *Advanced dynamics*. USA: McGraw-Hill Book Company (see p. 9).

[29] Limebeer, D. J. N. and Sharp, R. S. (2006) 'Bicycles, motorcycles, and models' *IEEE Control Systems Magazine*, 26(5), 34–61. DOI: 10.1109/MCS.2006.1700044 (see pp. 9, 27).

[30] Fintelman, D. M., Hemida, H., Sterling, M. and Li, F. X. (2015) 'CFD simulations of the flow around a cyclist subjected to crosswinds' *Journal of Wind Engineering and Industrial Aerodynamics*, 144, 31–41. DOI: 10.1016/j.jweia.2015.05.009 (see pp. 10, 17, 36).

[31] Barry, N., Burton, D., Crouch, T., Sheridan, J. and Luescher, R. (2012) 'Effect of crosswinds and wheel selection on the aerodynamic behavior of a cyclist' *Procedia Engineering*, 34, 20–25. DOI: 10.1016/j.proeng.2012.04.005 (see pp. 10, 17, 36, 97).

[32] Blocken, B., van Druenen, T., Toparlar, Y., Malizia, F., Mannion, P., Andrianne, T., Marchal, T., Maas, G.-J. and Diepens, J. (2018) 'Aerodynamic drag in cycling pelotons: New insights by CFD simulation and wind tunnel testing' *Journal of Wind Engineering and Industrial Aerodynamics*, 179, 319–337. DOI: 10.1016/j.jweia.2018.06.011 (see pp. 10, 20, 24, 25, 36, 37, 46, 48, 80, 84, 88).

[33] Terra, W., Sciacchitano, A. and Scarano, F. (2020) 'Cyclist Reynolds number effects and drag crisis distribution' *Journal of Wind Engineering and Industrial Aerodynamics*, 200, 104143. DOI: 10.1016/j.jweia.2020.104143 (see pp. 10, 13, 16, 23, 91, 97).

[34] Debraux, P., Bertucci, W., Manolova, A. V., Rogier, S. and Lodini, A. (2009) 'New method to estimate the cycling frontal area' *International Journal of Sports Medicine*, 30(4), 266–72. DOI: 10.1055/s-0028-1105940 (see p. 10).

[35] Drory, A., Li, H. and Hartley, R. (2017) 'Estimating the projected frontal surface area of cyclists from images using a variational framework and statistical shape and appearance models' *Proceedings of the Institution of Mechanical Engineers, Part P: Journal of Sports Engineering and Technology*, 231(3), 169–183. DOI: 10.1177/1754337117705489 (see p. 10).

[36] Malizia, F., van Druenen, T. and Blocken, B. (2021) 'Impact of wheel rotation on the aerodynamic drag of a time trial cyclist' *Sports Engineering*, 24, 3. DOI: 10.1007/s12283-021-00341-6 (see pp. 10, 23).

[37] Kyle, C. R. (2003) 'Selecting Cycling Equipment' in: *High-tech cycling*. Ed. by E. Burke. 2nd ed. USA: Human Kinetics (see pp. 11, 12, 17, 27, 28, 35, 79, 86, 90).

[38] Crouch, T. N., Burton, D., LaBry, Z. A. and Blair, K. B. (2017) 'Riding against the wind: a review of competition cycling aerodynamics' *Sports Engineering*, 20(2), 81–110. DOI: 10.1007/s12283-017-0234-1 (see pp. 11, 14–16, 20, 34, 36, 37, 80, 90, 91, 97).

[39] Picard, A., Davis, R., Gläser, M. and Fujii, K. (2008) 'Revised formula for the density of moist air (CIPM-2007)' *Metrologia*, 45(2), 149. DOI: 10.1088/0026-1394/45/2/004 (see pp. 11, 103).

[40] Wikipedia (2021) *List of world records in track cycling*. URL: https://en.wikipedia.org/wiki/List_of_world_records_in_track_cycling accessed: 28/10/2021 (see p. 11).

[41] Rusko, H., Tikkanen, H. and Peltonen, J. (2004) 'Altitude and endurance training' *Journal of Sports Sciences*, 22(10), 928–945. DOI: 10.1080/02640410400005933 (see p. 11).

[42] Bassett, D. R., Kyle, C. R., Passfield, L., Broker, J. P. and Burke, E. R. (1999) 'Comparing cycling world hour records, 1967–1996: modeling with empirical data' *Medicine and Science in Sports and Exercise*, 31(11), 1665–1676. DOI: 10.1097/00005768-199911000-00025 (see pp. 11, 12, 17).

[43] Underwood, L. (2012) 'Aerodynamics of Track Cycling' PhD Thesis. New Zealand: The University of Canterbury. DOI: 10.26021/3548 (see pp. 12, 35).

[44] Benham, G., Cohen, C., Brunet, E. and Clanet, C. (2020) 'Brachistochrone on a velodrome' *Proceedings of the Royal Society A: Mathematical, Physical and Engineering Sciences*, 476(2238), 20200153. DOI: 10.1098/rspa.2020.0153 (see pp. 12, 58, 68, 72).

[45] Bos, L., Slawinski, M. A., Slawinski, R. A. and Stanoev, T. (2021) *On modelling bicycle power for velodromes: Part II. Formulation for individual pursuits*. [Preprint] 08/01/2021. arXiv: 2009.01162v4 [physics.pop-ph] (see pp. 12, 13, 58, 59, 72).

[46] Craig, N. P. and Norton, K. I. (2001) 'Characteristics of Track Cycling' *Sports Medicine*, 31(7), 457–468. DOI: 10.2165/00007256-200131070-00001 (see pp. 13, 89).

[47] Olds, T. S., Norton, K. I., Lowe, E. L., Olive, S., Reay, F. and Ly, S. (1995) 'Modeling road-cycling performance' *Journal of Applied Physiology*, 78(4), 1596–1611. DOI: 10.1152/jappl.1995.78.4.1596 (see p. 13).

[48] Crouch, T. N., Burton, D., Brown, N. A. T., Thompson, M. C. and Sheridan, J. (2014) 'Flow topology in the wake of a cyclist and its effect on aerodynamic drag' *Journal of Fluid Mechanics*, 748, 5–35. DOI: 10.1017/jfm.2013.678 (see pp. 13, 18–20, 23, 35, 36, 98).

[49] Crouch, T. N., Burton, D., Thompson, M. C., Brown, N. A. T. and Sheridan, J. (2016) 'Dynamic leg-motion and its effect on the aerodynamic performance of cyclists' *Journal of Fluids and Structures*, 65, 121–137. DOI: 10.1016/j.jfluidstructs.2016.05.007 (see pp. 14, 19, 23, 35, 98, 99, 119).

[50] Griffith, M. D., Crouch, T. N., Burton, D., Sheridan, J., Brown, N. A. and Thompson, M. C. (2019) 'A numerical model for the time-dependent wake of a pedalling cyclist' *Proceedings of the Institution of Mechanical Engineers, Part P: Journal of Sports Engineering and Technology*, 233(4), 514–525. DOI: 10.1177/1754337119858434 (see pp. 14, 19, 25, 98, 104, 105).

[51] Fage, A. and Warsap, J. H. (1929) 'The effects of turbulence and surface roughness on the drag of a circular cylinder' *Aeronautical Research Committee Reports and Memoranda*, 1(1283). URL: https://reports.aerade.cranfield.ac.uk/handle/1826.2/1414 (see pp. 14, 15).

[52] Achenbach, E. (1971) 'Influence of surface roughness on the cross-flow around a circular cylinder' *Journal of Fluid Mechanics*, 46(2), 321–335. DOI: 10.1017/S0022112071000569 (see p. 14).

[53] Brownlie, L., Kyle, C., Carbo, J., Demarest, N., Harber, E., MacDonald, R. and Nordstrom, M. (2009) 'Streamlining the time trial apparel of cyclists: the Nike swift spin project' *Sports Technology*, 2(1-2), 53–60. DOI: 10.1002/jst.12 (see p. 14).

[54] Underwood, L. and Jermy, M. C. (2011) 'Fabric testing for cycling skinsuits' *Procedia Engineering*, 13, 350–356. DOI: 10.1016/j.proeng.2011.05.097 (see p. 14).

[55] Oggiano, L., Brownlie, L., Troynikov, O., Bardal, L. M., Sæter, C. and Sætran, L. (2013) 'A Review on Skin Suits and Sport Garment Aerodynamics: Guidelines and State of the Art' *Procedia Engineering*, 60, 91–98. DOI: 10.1016/j.proeng.2013.07.018 (see p. 14).

[56] Brownlie, L., Aihara, Y., Carbo, J., Harber, E., Henry, R., Ilcheva, I. and Ostafichuk, P. (2016) 'The Use of Vortex Generators to Reduce the Aerodynamic Drag of Athletic Apparel' *Procedia Engineering*, 147, 20–25. DOI: 10.1016/j.proeng.2016.06.183 (see p. 14).

[57] Zdravkovich, M. (1990) 'Conceptual overview of laminar and turbulent flows past smooth and rough circular cylinders' *Journal of Wind Engineering and Industrial Aerodynamics*, 33(1), 53–62. DOI: 10.1016/0167-6105(90)90020-D (see p. 14).

[58] Harries, A., Brunelli, G. and Rizos, I. (2013) 'London 2012 Velodrome - integrating advanced simulation into the design process' *Journal of Building Performance Simulation*, 6(6), 401–419. DOI: 10.1080/19401493.2012.718796 (see p. 14).

[59] Watkins, S. and Alam, F. (2014) 'The Turbulent Flow Field Relevant to Outdoor Sports' *Procedia Engineering*, 72, 792–797. DOI: 10.1016/j.proeng.2014.06.134 (see pp. 15, 36).

[60] Bearman, P. W. and Morel, T. (1983) 'Effect of free stream turbulence on the flow around bluff bodies' *Progress in Aerospace Sciences*, 20(2), 97–123. DOI: 10.1016/0376-0421(83)90002-7 (see pp. 15, 91).

[61] Barlow, J. B., Rae, W. H. and Pope, A. (1999) *Low-Speed Wind Tunnel Testing*. 3rd ed. USA: John Wiley and Sons (see pp. 16, 24, 102).

[62] Dryden, H. L., Schubauer, G., Mock, W. and Skramstad, H. (1937) 'Measurements of intensity and scale of wind-tunnel turbulence and their relation to the critical Reynolds number of spheres' *NACA*

Technical Report, (581). URL: https://ntrs.nasa.gov/citations/19930091656 (see p. 16).

[63] Gerhart, P. M., Gross, R. J. and Hochstein, J. I. (1992) *Fundamentals of Fluid Mechanics*. 2nd ed. USA: Addison-Wesley Publishing Company (see p. 16).

[64] Malizia, F. and Blocken, B. (2020) 'CFD simulations of an isolated cycling spoked wheel: Impact of the ground and wheel/ground contact modeling' *European Journal of Mechanics - B/Fluids*, 82, 21–38. DOI: 10.1016/j.euromechflu.2020.02.002 (see pp. 16, 98).

[65] Cooper, K. R. and Watkins, S. (2007) 'The Unsteady Wind Environment of Road Vehicles, Part One: A Review of the On-road Turbulent Wind Environment' *SAE Transactions*, 1259–1276. DOI: 10.4271/2007-01-1236 (see pp. 16, 36, 91).

[66] Watkins, S. and Cooper, K. R. (2007) 'The Unsteady Wind Environment of Road Vehicles, Part Two: Effects on Vehicle Development and Simulation of Turbulence' *SAE Transactions*, 1277–1291. DOI: 10.4271/2007-01-1237 (see pp. 16, 91).

[67] McAuliffe, B. R., Belluz, L. and Belzile, M. (2014) 'Measurement of the On-Road Turbulence Environment Experienced by Heavy Duty Vehicles' *SAE International Journal of Commercial Vehicles*, 7(2), 685–702. DOI: 10.4271/2014-01-2451 (see p. 16).

[68] Garratt, J. R. (1994) 'Review: the atmospheric boundary layer' *Earth-Science Reviews*, 37(1), 89–134. DOI: 10.1016/0012-8252(94)90026-4 (see p. 16).

[69] D'Auteuil, A. (2010) 'Manipulation of the Boundary Layer Transition to Enhance the Aerodynamic Performance of Athletes' PhD Thesis. Canada: Ottawa-Carleton Institute for Mechanical and Aerospace Engineering. DOI: 10.22215/etd/2010-12529 (see pp. 16, 17, 36).

[70] D'Auteuil, A., Larose, G. L. and Zan, S. J. (2012) 'Wind turbulence in speed skating: Measurement, simulation and its effect on aerodynamic drag' *Journal of Wind Engineering and Industrial Aerodynamics*, 104, 585–593. DOI: 10.1016/j.jweia.2012.02.002 (see pp. 16, 36, 80, 90, 91).

[71] Kyle, C. R. (2010) *Chet Kyle on bicycles, solar cars, and human powered aircraft*. URL: https://archive.org/details/ChetKyleOn accessed: 09/07/2021 (see pp. 17, 27).

[72] Okada, Y., Nouzawa, T., Okamoto, S., Fujita, T., Kamioka, T. and Tsubokura, M. (2012) 'Unsteady Vehicle Aerodynamics during a Dynamic Steering Action: 1st Report, On-Road Analysis' *SAE Technical Paper*. DOI: 10.4271/2012-01-0446 (see p. 17).

[73] Nara, K., Tsubokura, M. and Ikeda, J. (n.d.) 'A Numerical Analysis of Unsteady Aerodynamics of Formula Car During Dynamic Cornering Motion' *32nd AIAA Applied Aerodynamics Conference*. DOI: 10.2514/6.2014-3138 (see p. 17).

[74] Keogh, J., Barber, T., Diasinos, S. and Doig, G. (2015) 'Techniques for Aerodynamic Analysis of Cornering Vehicles' *18th Asia Pacific Automotive Engineering Conference*. SAE International. DOI: 10.4271/2015-01-0022 (see p. 17).

[75] Keogh, J., Barber, T., Diasinos, S. and Doig, G. (2016) 'The aerodynamic effects on a cornering Ahmed body' *Journal of Wind Engineering and Industrial Aerodynamics*, 154, 34–46. DOI: 10.1016/j.jweia.2016.04.002 (see pp. 17, 35, 39).

[76] Ahmed, S. R., Ramm, G. and Faltin, G. (1984) 'Some Salient Features of the Time-Averaged Ground Vehicle Wake' *SAE Transactions*, 93, 473–503. DOI: 10.4271/840300 (see pp. 17, 22).

[77] Íñiguez-de-la-Torre, I. and Íñiguez, J. (2005) 'Cycling and wind: does sidewind brake?' *European Journal of Physics*, 27(1), 71–74. DOI: 10.1088/0143-0807/27/1/007 (see pp. 17, 36).

[78] Brownlie, L., Ostafichuk, P., Tews, E., Muller, H., Briggs, E. and Franks, K. (2010) 'The wind-averaged aerodynamic drag of competitive time trial cycling helmets' *Procedia Engineering*, 2(2), 2419–2424. DOI: 10.1016/j.proeng.2010.04.009 (see pp. 17, 53).

[79] Fintelman, D., Sterling, M., Hemida, H. and Li, F.-X. (2014) 'The effect of crosswinds on cyclists: an experimental study' *Procedia Engineering*, 72, 720–725. DOI: 10.1016/j.proeng.2014.06.122 (see p. 17).

[80] Mannion, P., Toparlar, Y., Clifford, E., Hajdukiewicz, M., Andrianne, T. and Blocken, B. (2019) 'On the effects of crosswinds in tandem aerodynamics: An experimental and computational study' *European*

Journal of Mechanics - B/Fluids, 74, 68–80. DOI: 10.1016/j.euromechflu.2018.11.001 (see p. 17).

[81] Baidya, R., Monty, J. P. and Hutchins, N. (2010) 'Aerodynamics of High Cadence Cycling' *17th Australasian Fluid Mechanics Conference*. Ed. by G. D. Mallinson. URL: https://www.afms.org.au/proceedings/17.html (see pp. 19, 23, 98).

[82] Crouch, T., Thompson, M., Burton, D., Sheridan, J. and Brown, N. (2012) 'Dominant Flow Structures In The Wake of A Cyclist' *30th AIAA Applied Aerodynamics Conference*. DOI: 10.2514/6.2012-3212 (see p. 19).

[83] Crouch, T., Sheridan, J., Burton, D., Thompson, M. and Brown, N. A. T. (2012) 'A quasi-static investigation of the effect of leg position on cyclist aerodynamic drag' *Procedia Engineering*, 34, 3–8. DOI: 10.1016/j.proeng.2012.04.002 (see p. 19).

[84] Griffith, M. D., Crouch, T., Thompson, M. C., Burton, D., Sheridan, J. and Brown, N. A. T. (2014) 'Computational Fluid Dynamics Study of the Effect of Leg Position on Cyclist Aerodynamic Drag' *Journal of Fluids Engineering*, 136(10), 101105. DOI: 10.1115/1.4027428 (see p. 19).

[85] Spoelstra, A., de Martino Norante, L., Terra, W., Sciacchitano, A. and Scarano, F. (2019) 'On-site cycling drag analysis with the Ring of Fire' *Experiments in Fluids*, 60(6), 90. DOI: 10.1007/s00348-019-2737-y (see pp. 20, 23, 26, 98).

[86] Broker, J. P., Kyle, C. R. and Burke, E. R. (1999) 'Racing cyclist power requirements in the 4000-m individual and team pursuits' *Medicine and Science in Sports and Exercise*, 31(11), 1677–1685. DOI: 10.1097/00005768-199911000-00026 (see p. 20).

[87] Edwards, A. G. and Byrnes, W. C. (2007) 'Aerodynamic Characteristics as Determinants of the Drafting Effect in Cycling' *Medicine and Science in Sports and Exercise*, 39(1), 170–176. DOI: 10.1249/01.mss.0000239400.85955.12 (see p. 20).

[88] Íñiguez-de-la Torre, A. and Íñiguez, J. (2009) 'Aerodynamics of a cycling team in a time trial: does the cyclist at the front benefit?' *European Journal of Physics*, 30(6), 1365–1369. DOI: 10.1088/0143-0807/30/6/014 (see pp. 20, 21).

[89] Blocken, B., Defraeye, T., Koninckx, E., Carmeliet, J. and Hespel, P. (2013) 'CFD simulations of the aerodynamic drag of two drafting cyclists' *Computers and Fluids*, 71, 435–445. DOI: 10.1016/j.compfluid.2012.11.012 (see pp. 20, 37).

[90] Defraeye, T., Blocken, B., Koninckx, E., Hespel, P., Verboven, P., Nicolai, B. and Carmeliet, J. (2014) 'Cyclist Drag in Team Pursuit: Influence of Cyclist Sequence, Stature, and Arm Spacing' *Journal of Biomechanical Engineering*, 136(1), 011005. DOI: 10.1115/1.4025792 (see pp. 20, 37).

[91] Barry, N., Sheridan, J., Burton, D. and Brown, N. A. T. (2014) 'The Effect of Spatial Position on the Aerodynamic Interactions between Cyclists' *Procedia Engineering*, 72, 774–779. DOI: 10.1016/j.proeng.2014.06.131 (see pp. 20–22, 79).

[92] Barry, N., Burton, D., Sheridan, J., Thompson, M. and Brown, N. A. T. (2015) 'Aerodynamic drag interactions between cyclists in a team pursuit' *Sports Engineering*, 18(2), 93–103. DOI: 10.1007/s12283-015-0172-8 (see pp. 20, 23, 37, 48).

[93] Barry, N., Burton, D., Sheridan, J., Thompson, M. and Brown, N. A. T. (2016) 'Flow field interactions between two tandem cyclists' *Experiments in Fluids*, 57(12), 181. DOI: 10.1007/s00348-016-2273-y (see pp. 20, 37).

[94] Blocken, B., Toparlar, Y. and Andrianne, T. (2016) 'Aerodynamic benefit for a cyclist by a following motorcycle' *Journal of Wind Engineering and Industrial Aerodynamics*, 155, 1–10. DOI: 10.1016/j.jweia.2016.04.008 (see pp. 20, 23).

[95] Fitton, B., Caddy, O. and Symons, D. (2017) 'The impact of relative athlete characteristics on the drag reductions caused by drafting when cycling in a velodrome' *Proceedings of the Institution of Mechanical Engineers, Part P: Journal of Sports Engineering and Technology*, 232(1), 39–49. DOI: 10.1177/1754337117692280 (see pp. 20, 21, 23, 25, 26, 37, 48, 90).

[96] Shirasaki, K., Yamanobe, K., Akashi, K. and Takashima, W. (2017) 'Variation of the drafting effect on the trailing rider for different numbers of riders in a cycling group' *Proceedings of the Institution of Mechanical Engineers, Part P: Journal of Sports Engineering and Technology*, 1754337117736617. DOI: 10.1177/1754337117736617 (see pp. 20, 21).

[97] Blocken, B., Toparlar, Y., van Druenen, T. and Andrianne, T. (2018) 'Aerodynamic drag in cycling team time trials' *Journal of Wind Engineering and Industrial Aerodynamics*, 182, 128–145. DOI: 10.1016/j.jweia.2018.09.015 (see pp. 20, 21, 36, 37, 48).

[98] Spoelstra, A., Mahalingesh, N. and Sciacchitano, A. (2020) 'Drafting Effect in Cycling: On-Site Aerodynamic Investigation by the 'Ring of Fire'' *Proceedings*, 49(1), 113. DOI: 10.3390/proceedings2020049113 (see pp. 20, 21).

[99] Blocken, B., Gillmeier, S., Malizia, F. and van Druenen, T. (2021) 'Impact of a motorcycle on cyclist aerodynamic drag in parallel and staggered arrangements' *Sports Engineering*, 24, 7. DOI: 10.1007/s12283-021-00344-3 (see pp. 20–22).

[100] Van Druenen, T. and Blocken, B. (2021) 'Aerodynamic analysis of uphill drafting in cycling' *Sports Engineering*, 24, 10. DOI: 10.1007/s12283-021-00345-2 (see pp. 20, 21).

[101] Jacobs, E. N., Ward, K. E. and Pinkerton, R. M. (1933) 'The Characteristics of 78 related airfoil section from tests in the Variable-Density Wind Tunnel' *NACA Technical Report*, (460). URL: https://ntrs.nasa.gov/citations/19930091108 (see p. 22).

[102] Kyle, C. R. (1991) 'The effect of crosswinds upon time trials' *Cycling Science*, 51–56 (see p. 23).

[103] Zdravkovich, M., Ashcroft, M., Chishohn, S. and Hicks, N. (1996) 'Effect of cyclist's posture and vicinity of another cyclist on aerodynamic drag' in: *The Engineering of Sport*. Ed. by S. Haake. 1st ed. Great Britain: CRC Press, 21–28. URL: https://www.taylorfrancis.com/chapters/edit/10.1201/9781003078098-4 (see p. 23).

[104] Padilla, S., Mujika, I., Angulo, F. and Goiriena, J. J. (2000) 'Scientific approach to the 1-h cycling world record: a case study' *Journal of Applied Physiology*, 89(4), 1522–1527. DOI: 10.1152/jappl.2000.89.4.1522 (see p. 23).

[105] Gibertini, G. and Grassi, D. (2008) 'Cycling Aerodynamics' in: *Sport Aerodynamics*. Ed. by N. Helge. Austria: Springer, Vienna, 23–47. DOI: 10.1007/978-3-211-89297-8_3 (see p. 23).

[106] García-López, J., Rodríguez-Marroyo, J. A., Juneau, C.-E., Peleteiro, J., Martínez, A. C. and Villa, J. G. (2008) 'Reference values and

improvement of aerodynamic drag in professional cyclists' *Journal of Sports Sciences*, 26(3), 277–286. DOI: 10.1080/02640410701501697 (see p. 23).

[107] Defraeye, T., Blocken, B., Koninckx, E., Hespel, P. and Carmeliet, J. (2010) 'Aerodynamic study of different cyclist positions: CFD analysis and full-scale wind-tunnel tests' *Journal of Biomechanics*, 43(7), 1262–1268. DOI: 10.1016/j.jbiomech.2010.01.025 (see p. 23).

[108] Underwood, L., Schumacher, J., Burette-Pommay, J. and Jermy, M. (2011) 'Aerodynamic drag and biomechanical power of a track cyclist as a function of shoulder and torso angles' *Sports Engineering*, 14(2), 147–154. DOI: 10.1007/s12283-011-0078-z (see p. 23).

[109] Chi, S., Pitman, J., Crouch, T., Burton, D. and Thompson, M. (2021) 'The application of body scanning, numerical simulations and wind tunnel testing for the aerodynamic development of cyclists' *Proceedings of the Institution of Mechanical Engineers, Part P: Journal of Sports Engineering and Technology*, 235(4), 339–353. DOI: 10.1177/1754337120904258 (see p. 23).

[110] Javadi, A., Buckrell, A. J. M. and Peterson, S. D. (2020) 'Improving Numerical Estimation of Cyclist Drag Area in Static Conditions Using Unsteady RANS' *Proceedings*, 49(1), 139. DOI: 10.3390/proceedings2020049139 (see p. 23).

[111] Grappe, F., Candau, R., Belli, A. and Rouillon, J. D. (1997) 'Aerodynamic drag in field cycling with special reference to the Obree's position' *Ergonomics*, 40(12), 1299–1311. DOI: 10.1080/001401397187388 (see p. 23).

[112] Candau, R. B., Grappe, F., Menard, M., Barbier, B., Millet, G. Y., Hoffman, M. D., Belli, A. R. and Rouillon, J. D. (1999) 'Simplified deceleration method for assessment of resistive forces in cycling' *Medicine and science in sports and exercise*, 31(10), 1441–1447. DOI: 10.1097/00005768-199910000-00013 (see p. 23).

[113] Valenzuela, P. L., Alcalde, Y., Gil-Cabrera, J., Talavera, E., Lucia, A. and Barranco-Gil, D. (2020) 'Validity of a novel device for real-time analysis of cyclists' drag area' *Journal of Science and Medicine in Sport*, 23(4), 421–425. DOI: 10.1016/j.jsams.2019.10.023 (see pp. 23, 25).

[114] Williams, M. (2020). [LinkedIn Post]. URL: https://www.linkedin.com/posts/matthew-williams-58290413_cfd-is-an-important-

tool-in-helping-to-decipher-activity-6666256162310230016-uEZA accessed: 21/07/2021 (see pp. 22, 25).

[115] LSWT (2021) *San Diego Low Speed Wind Tunnel*. URL: http://www.sandiegowindtunnel.com/high-performance-cycling.html accessed: 21/06/2021 (see p. 22).

[116] Monash University (2021) *Wind Tunnel*. URL: https://www.monash.edu/engineering/our-research/facilities/wind-tunnel-facility accessed: 21/06/2021 (see p. 22).

[117] A2 (2021) *A2 Wind Tunnel*. URL: https://a2wt.com/cycling accessed: 21/06/2021 (see pp. 22, 23).

[118] Celis, B. and Ubbens, H. H. (2016) 'Design and Construction of an Open-circuit Wind Tunnel with Specific Measurement Equipment for Cycling' *Procedia Engineering*, 147, 98–103. DOI: 10.1016/j.proeng.2016.06.196 (see p. 23).

[119] Bäckström, M., Carlsson, P., Danvind, J., Koptyug, A., Sundström, D. and Tinnsten, M. (2016) 'A New Wind Tunnel Facility Dedicated to Sports Technology Research and Development' *Procedia Engineering*, 147, 62–67. DOI: 10.1016/j.proeng.2016.06.190 (see p. 23).

[120] Specialized (2021) *Aero is Everything*. URL: https://www.specialized.com/au/en/stories/aero-is-everything accessed: 21/06/2021 (see p. 23).

[121] Eindhoven University of Technology (2021) *Research Lab: Wind Tunnel*. URL: https://www.tue.nl/en/research/research-labs/wind-tunnel accessed: 21/06/2021 (see p. 23).

[122] Drag2Zero (2021) *Drag2Zero Bike Wind Tunnel*. URL: https://drag2zero.co.uk accessed: 21/06/2021 (see p. 23).

[123] Brownlie, L. W. (2019) 'Wind Tunnels: Design Considerations in Wind Tunnel Testing of Cyclists' in: *Biomechanical Principles and Applications in Sports*. Ed. by J. M. Pallis, J. L. McNitt-Gray and G. K. Hung. Switzerland: Springer Nature, 57–86. DOI: 10.1007/978-3-030-13467-9_4 (see pp. 23, 24).

[124] Terra, W., Sciacchitano, A. and Shah, Y. H. (2019) 'Aerodynamic drag determination of a full-scale cyclist mannequin from large-scale PTV measurements' *Experiments in Fluids*, 60(2), 29. DOI: 10.1007/s00348-019-2677-6 (see pp. 24, 35, 36).

[125] Tengattini, S. and Bigazzi, A. (2018) 'Validation of an Outdoor Coast-Down Test to Measure Bicycle Resistance Parameters' *Journal of Transportation Engineering, Part A: Systems*, 144(7), 04018031. DOI: 10.1061/JTEPBS.0000152 (see p. 25).

[126] Notio Technologies (2021) *Notio Aerometer*. URL: https://notio.ai/products/notio-ride-tracker accessed: 06/05/2021 (see p. 25).

[127] Morton, C. (2020) *Aeropro sensor system v1.0.0*. URL: https://aerolab.tech/news/tech-paper accessed: 18/02/2021 (see p. 25).

[128] Kordi, M., Galis, G., van Erp, T. and Terra, W. (2021) 'Reliability and sensitivity of the Notio Konect to quantify coefficient of drag area in elite track cyclists' *European Journal of Sport Science*, 1–6. DOI: 10.1080/17461391.2021.1891296 (see p. 25).

[129] Chung, R. (2012) *Estimating CdA with a power meter*. URL: http://anonymous.coward.free.fr/wattage/cda/indirect-cda.pdf accessed: 12/03/2020 (see p. 26).

[130] Sciacchitano, A., Caridi, G. C. A. and Scarano, F. (2015) 'A Quantitative Flow Visualization Technique for On-site Sport Aerodynamics Optimization' *Procedia Engineering*, 112, 412–417. DOI: 10.1016/j.proeng.2015.07.217 (see p. 26).

[131] Whipple, F. J. W. (1899) 'The stability of the motion of a bicycle' *Quarterly Journal of Pure and Applied Mathematics*, 30(120), 312–348 (see p. 26).

[132] Carvallo, E. (1899) *Théorie Du Mouvement Du Monocycle Et De La Bicyclette [Theory of the movement of the unicycle and the bicycle]*. France: Gauthier-Villars (see p. 26).

[133] Meijaard, J., Papadopoulos, J. M., Ruina, A. and Schwab, A. (2007) 'Linearized dynamics equations for the balance and steer of a bicycle: a benchmark and review' *Proceedings of the Royal Society A: Mathematical, Physical and Engineering Sciences*, 463(2084), 1955–1982. DOI: 10.1098/rspa.2007.1857 (see pp. 26, 27).

[134] Wang, E. X., Zou, J., Xue, G., Liu, Y., Li, Y. and Fan, Q. (2015) 'Development of Efficient Nonlinear Benchmark Bicycle Dynamics for Control Applications' *IEEE Transactions on Intelligent Transportation Systems*, 16(4), 2236–2246. DOI: 10.1109/TITS.2015.2404339 (see p. 26).

[135] Moore, J. K., Hubbard, M., Kooijman, J. D. G. and Schwab, A. L. (2009) 'A Method for Estimating Physical Properties of a Combined Bicycle and Rider' *ASME 2009 International Design Engineering Technical Conferences and Computers and Information in Engineering Conference*. Vol. 4, 2011–2020. DOI: 10.1115/detc2009-86947 (see p. 27).

[136] Pacejka, H. (2005) *Tire and vehicle dynamics*. 3rd ed. Great Britain: Elsevier. URL: https://www.sciencedirect.com/book/9780080970165 (see p. 27).

[137] Gladstone, H. (2011) *Making Tracks: building the Olympic velodrome*. URL: https://www.cyclingweekly.com/news/making-tracks-building-the-olympic-velodrome-53916 accessed: 12/11/2020 (see pp. 29, 63).

[138] Belloli, M., Giappino, S., Robustelli, F. and Somaschini, C. (2016) 'Drafting Effect in Cycling: Investigation by Wind Tunnel Tests' *Procedia Engineering*, 147, 38–43. DOI: 10.1016/j.proeng.2016.06.186 (see p. 37).

[139] Hussain, A. K. M. F. and Reynolds, W. C. (1970) 'The mechanics of an organized wave in turbulent shear flow' *Journal of Fluid Mechanics*, 41(2), 241–258. DOI: 10.1017/S0022112070000605 (see pp. 43, 88).

[140] Savitzky, A. and Golay, M. J. (1964) 'Smoothing and Differentiation of Data by Simplified Least Squares Procedures' *Analytical Chemistry*, 36(8), 1627–1639. DOI: 10.1021/ac60214a047 (see p. 43).

[141] Barry, N. (2018) 'A New Method for Analysing the Effect of Environmental Wind on Real World Aerodynamic Performance in Cycling' *Proceedings*, 2(6), 211. DOI: 10.3390/proceedings2060211 (see pp. 53, 122).

[142] Fitzgerald, S., Kelso, R., Grimshaw, P. and Warr, A. (2019) 'Measurement of the air velocity and turbulence in a simulated track cycling team pursuit race' *Journal of Wind Engineering and Industrial Aerodynamics*, 190, 322–330. DOI: 10.1016/j.jweia.2019.05.014 (see pp. 57, 64, 80, 84, 88, 90, 98–101, 116, 117, 120).

[143] Bartels, R. H., Beatty, J. C. and Barsky, B. A. (1987) *An Introduction to Splines for use in Computer Graphics and Geometric Modeling*. USA: Morgan Kaufmann. URL: https://www.elsevier.com/books/an-introduction-to-splines-for-use-in-computer-graphics-and-geometric-modeling/bartels/978-0-08-050921-1 (see p. 59).

[144] Brustad, T. F. and Dalmo, R. (2020) 'Railway Transition Curves: A Review of the State-of-the-Art and Future Research' *Infrastructures*, 5(5), 43. DOI: 10.3390/infrastructures5050043 (see p. 59).

[145] Pendrill, A.-M. and Eager, D. (2020) 'Velocity, acceleration, jerk, snap and vibration: forces in our bodies during a roller coaster ride' *Physics Education*, 55(6), 065012. DOI: 10.1088/1361-6552/aba732 (see p. 59).

[146] Meek, D. S. and Walton, D. J. (1989) 'The use of Cornu spirals in drawing planar curves of controlled curvature' *Journal of Computational and Applied Mathematics*, 25(1), 69–78. DOI: 10.1016/0377-0427(89)90076-9 (see p. 59).

[147] Nutbourne, A. W., McLellan, P. M. and Kensit, R. M. L. (1972) 'Curvature profiles for plane curves' *Computer-Aided Design*, 4(4), 176–184. DOI: 10.1016/0010-4485(72)90072-3 (see p. 60).

[148] Elhassan, I. M. and Ali, A. S. (2011) 'Comparative study of accuracy in distance measurement using: Optical and digital levels' *Journal of King Saud University - Engineering Sciences*, 23(1), 15–19. DOI: 10.1016/j.jksues.2010.10.001 (see p. 67).

[149] Gander, W., Golub, G. H. and Strebel, R. (1994) 'Least-squares fitting of circles and ellipses' *BIT Numerical Mathematics*, 34(4), 558–578. DOI: 10.1007/BF01934268 (see p. 67).

[150] Hossain, M. I., Eager, D. and Walker, P. D. (2020) 'Greyhound racing ideal trajectory path generation for straight to bend based on jerk rate minimization' *Scientific Reports*, 10(1), 7088. DOI: 10.1038/s41598-020-63678-1 (see p. 73).

[151] Mahdavi, F., Hossain, M. I., Hayati, H., Eager, D. and Kennedy, P. (2018) 'Track Shape, Resulting Dynamics and Injury Rates of Greyhounds' *ASME 2018 International Mechanical Engineering Congress and Exposition. Volume 13: Design, Reliability, Safety, and Risk*. Vol. 13. DOI: 10.1115/imece2018-87156 (see p. 73).

[152] World Athletics (2019) *Track and Field Facilities Manual 2019 Edition - Chapters 1-3. Version 01.11.2019*. URL: https://www.worldathletics.org/about-iaaf/documents/technical-information (see p. 73).

[153] Sanjurjo, E., Naya, M. A., Cuadrado, J. and Schwab, A. L. (2019) 'Roll angle estimator based on angular rate measurements for bicycles'

Vehicle System Dynamics, 57(11), 1705–1719. DOI: 10.1080/00423114.2018.1551554 (see p. 79).

[154] Sakai, D., Uchida, N., Enomoto, S., Iwata, S., Kawakami, Y. and Wesugi, S. (2020) 'Improving Road Bike Leaning Skills on Downhill Corners (Developing a System for Detecting Curvature Change Points and the Angle of a Road Bike while Riding)' *Proceedings*, 49(1), 153. DOI: 10.3390/proceedings2020049153 (see p. 79).

[155] Fujii, S., Shiozawa, S., Shinagawa, A. and Kishi, T. (2012) 'Steering characteristics of motorcycles' *Vehicle System Dynamics*, 50(8), 1277–1295. DOI: 10.1080/00423114.2011.607900 (see p. 79).

[156] Brown, C., Crouch, T., Burton, D. and Thompson, M. C. (2020) 'Understanding the Aerodynamic Benefits of Drafting in the Wake of Cyclists' *Proceedings*, 49(1), 32. DOI: 10.3390/proceedings2020049032 (see pp. 79, 90).

[157] Union Cycliste Internationale (2021) *UCI Cycling Regulations: Part II: Road Races. Version 10.06.2021*. URL: https://www.uci.org/inside-uci/constitutions-regulations/regulations (see p. 80).

[158] Malizia, F. and Blocken, B. (2021) 'Cyclist aerodynamics through time: Better, faster, stronger' *Journal of Wind Engineering and Industrial Aerodynamics*, 214, 104673. DOI: 10.1016/j.jweia.2021.104673 (see pp. 80, 90).

[159] Fitzgerald, S., Kelso, R., Grimshaw, P. and Warr, A. (2020) 'Observations of the flow experienced by a track cyclist using velodrome, wind tunnel, and potential flow investigations with an instrumented bicycle' *Journal of Wind Engineering and Industrial Aerodynamics*, 206, 104374. DOI: 10.1016/j.jweia.2020.104374 (see pp. 80, 90–92).

[160] Fitzgerald, S., Kelso, R., Grimshaw, P. and Warr, A. (2021) 'Impact of transition design on the accuracy of velodrome models' *Sports Engineering*, 24, 23. DOI: 10.1007/s12283-021-00360-3 (see pp. 81, 89, 93, 94).

[161] Doria, A. and Roa, S. (2018) 'On the influence of tyre and structural properties on the stability of bicycles' *Vehicle System Dynamics*, 56(6), 947–966. DOI: 10.1080/00423114.2017.1403032 (see p. 81).

[162] Soden, P. D. and Adeyefa, B. A. (1979) 'Forces applied to a bicycle during normal cycling' *Journal of Biomechanics*, 12(7), 527–541. DOI: 10.1016/0021-9290(79)90041-1 (see p. 82).

[163] Emes, M. J., Arjomandi, M., Kelso, R. M. and Ghanadi, F. (2019) 'Turbulence length scales in a low-roughness near-neutral atmospheric surface layer' *Journal of Turbulence*, 20(9), 545–562. DOI: 10.1080/14685248.2019.1677908 (see p. 88).

[164] Kestrel (2021) *Kestrel 5000 Environmental Meter*. URL: https://kestrelmeters.com/products/kestrel-5000-environmental-meter accessed: 08/03/2021 (see p. 88).

[165] Hoerner, S. F. (1965) *Fluid-dynamic drag: practical information on aerodynamic drag and hydrodynamic resistance*. 2nd ed. USA: Published by the Author (see p. 91).

[166] Karabelas, S. J. and Markatos, N. C. (2012) 'Aerodynamics of Fixed and Rotating Spoked Cycling Wheels' *Journal of Fluids Engineering*, 134(1), 011102. DOI: 10.1115/1.4005691 (see p. 97).

[167] Malizia, F., Montazeri, H. and Blocken, B. (2019) 'CFD simulations of spoked wheel aerodynamics in cycling: Impact of computational parameters' *Journal of Wind Engineering and Industrial Aerodynamics*, 194, 103988. DOI: 10.1016/j.jweia.2019.103988 (see p. 97).

[168] Crane, R. and Morton, C. (2018) 'Drag and Side Force Analysis on Bicycle Wheel–Tire Combinations' *Journal of Fluids Engineering*, 140(6). DOI: 10.1115/1.4039513 (see p. 97).

[169] Godo, M., Corson, D. and Legensky, S. (2010) 'A Comparative Aerodynamic Study of Commercial Bicycle Wheels Using CFD' *48th AIAA Aerospace Sciences Meeting Including the New Horizons Forum and Aerospace Exposition*. DOI: 10.2514/6.2010-1431 (see pp. 98, 112).

[170] Chan, H. C. (2018) 'High cadence cycling: aerodynamic drag and wake structure' PhD Thesis. Australia: University of Melbourne. URL: http://hdl.handle.net/11343/214463 (see pp. 98, 119).

[171] Bentley, R. (2005) 'Uncertainty in measurement: The ISO guide' *National Measurement Institute, Sydney, Australia*. URL: https://shop.measurement.gov.au/products/monograph-1 (see p. 104).

[172] Vallentine, H. R. (1969) *Applied Hydronamics*. SI ed. Great Britain: Butterworth and Co (see pp. 107, 109).

[173] Prandtl, L. (1921) 'Applications of modern hydrodynamics to aeronautics' *NACA Technical Report*, (116), 157–215. URL: https://ntrs.nasa.gov/citations/19930091180 (see p. 112).

[174] Prandtl, L. (1904) 'Über Flüssigkeitsbewegung bei sehr kleiner Reibung [On the motion of fluids in very little friction]' *Verhandlungen des dritten internationalen Mathematiker-Kongresses*. English trans. In: J. Ackroyd, B. Axcell, A. Ruban, (Eds.), Early Developments of Modern Aerodynamics, 489–491 (see p. 115).

[175] Smith, L. H. and Nunn, R. H. (1976) 'Aerodynamic characteristics of an axisymmetric body undergoing a uniform pitching motion' *Journal of Spacecraft and Rockets*, 13(1), 8–14. DOI: 10.2514/3.57059 (see p. 120).

[176] Althus, D. (1980) *Profilpolaren für den Modellflug: Windkanalmessungen an Profilen im kritischen Reynoldszahlbereich [Profile polar for model flying: Wind tunnel measurements on profiles in the critical Reynolds number range]*. Germany: Neckar-Velag, Villingen-Schwenningen (see p. 128).

[177] Bloss, A. E. (1936) 'Der Übergangsbogen mit geschwungener Überhöhungsrampe [The transition bend with a curved superelevation ramp]' *Organ für die Fortschritte des Eisenbahnwesens*, 91, 319–320. URL: https://www.google.com.au/books/edition/_/UQ_nAAAAMAAJ (see p. 131).

[178] Watorek, K. (1907) 'Übergangsbogen [Transition bend]' *Organ für die Fortschritte des Eisenbahnwesens*, 62, 186–189. URL: https://www.google.com.au/books/edition/_/QnbmAAAAMAAJ (see p. 131).

[179] Schuhr, P. (2007) 'Übergangsbogen für Bahnen mit hohen Fahrgeschwindigkeiten [Transition bend for railways with high travel speeds]' *Deutsche Geodätische Kommission: B (Angewandte Geodäsie)*, Reihe B, Angewandte Geodäsie; 314. URL: https://publikationen.badw.de/de/022412726 (see p. 131).